2020

Attribution of Soil Surface Temperature Sensitivity to Hydro-climatic Drivers

Sarah Khalid

Marco Maneta

ATTRIBUTION OF SOIL SURFACE TEMPERATURE SENSITIVITY TO HYDRO-CLIMATIC DRIVERS

By

SARAH KHALID

B.Sc. Arizona State University, Tempe, AZ, 2018

Thesis

presented in partial fulfillment of the requirements

for the degree of

Master of Science

Geoscience

The University of Montana

Missoula, MT

January 22, 2021

Approved by:

Scott Whittenburg, Dean of The Graduate School

Graduate School

Dr. Marco Maneta (Chair)

Department of Geosciences

Dr. Solomon Dobrowski

Department of Forest Management

Dr. Payton Gardner

Department of Geosciences

Dr. Zachary Holden

U.S. Forest Service

Khalid, Sarah, MS, Fall 2020   Geoscience

Attribution of Soil Surface Temperature Sensitivity to Hydro-climatic Drivers

Chairperson: Dr. Marco Maneta

Greenhouse gas emissions caused by human economic activity are altering the global hydrologic cycle and the energy exchanges at the land surface. In large portions of the western US there is evidence of reduced summertime precipitation and increased air temperatures and longwave irradiation. At local scales, these changes can translate into more frequent and intense extreme land surface temperature events during the summer, with potential impacts on wildfire activity, forest health, soil biochemical cycles, and thermal comfort for human populations. However, because increases in radiation and sensible heat (air temperature) inputs to the land surface are confounded with changes in water availability, which alter the way the surface energy balance is reapportioned, it is difficult to disentangle the specific contributions of these factors to the observed dynamics of land surface temperatures. This thesis contributes insight into this problem using a combination of analytical and numerical model applications in a plot and for the city of Missoula, MT. In the first chapter of this thesis we used analytical method on a surface energy balance equation to identify and assess the attribution of surface temperature sensitivities to key hydro-climatic drivers in a plot of soil with and without vegetation canopy cover. The second chapter uses an ecohydrological model to investigate the effect of perturbations in water input regimes (additions to soil moisture) on surface temperatures for different land covers in a semi-arid urban area (Missoula, MT).

Table of Contents

Summary

Greenhouse gas emissions caused by human economic activity are altering the global hydrologic cycle and the energy exchanges at the land surface. In large portions of the western US there is evidence of reduced summertime precipitation and increased air temperatures and longwave irradiation. At local scales, these changes can translate into more frequent and intense extreme land surface temperature events during the summer, with potential impacts on wildfire activity, forest health, soil biochemical cycles, and thermal comfort for human populations. However, because increases in radiation and sensible heat (air temperature) inputs to the land surface are confounded with changes in water availability, which alter the way the surface energy balance is reapportioned, it is difficult to disentangle the specific contributions of these factors to the observed dynamics of land surface temperatures. This thesis contributes insight into this problem using a combination of analytical and numerical model applications in a plot and for the city of Missoula, MT. In the first chapter of this thesis we used analytical method on a surface energy balance equation to identify and assess the attribution of surface temperature sensitivities to key hydro-climatic drivers in a plot of soil with and without vegetation canopy cover. The second chapter uses an ecohydrological model to investigate the effect of perturbations in water input regimes (additions to soil moisture) on surface temperatures for different land covers in a semi-arid urban area (Missoula, MT).

Research Questions

Main research question: What are the sensitivities of local soil surface temperatures to hydro-climatic drivers: shortwave radiation, longwave radiation, air temperature and soil moisture?

Specific research questions:

1. What is the relative radiative and non-radiative sensitivity of soil surface temperatures to hydro-climatic drivers for a bare soil landcover?

2. What is the effect of vegetation on the radiative and non-radiative sensitivities of soil surface temperatures to hydro-climatic drivers?

3. How do the soil surface temperatures to hydro-climatic drivers for different urban land covers respond to a range of water input regimes in a small semiarid urban microclimate using an ecohydrological model?

Hypotheses

In order to address the research questions posed above and driven by the attribution of soil surface temperature sensitivities not only to hydro-climatic drivers but also ultimately to intrinsic geophysical parameters governing differences between them (e.g., soil resistance, soil capacitance, emissivity, albedo, aerodynamic resistance, amount of shading on the ground, soil field capacity), we propose the following hypotheses:

a) The modulating effect that soil moisture has on surface temperature sensitivities exerts a stronger control than air temperature and radiation variations when soil moisture levels are moderate or high. This is due to intrinsic wet soil properties such as high thermal capacity and thermal inertia.

b) The relative modulating effect of soil moisture on surface temperature increases under vegetated scenarios. This is because in addition to soil moisture increasing the bulk thermal capacity of soils and enhancing evaporative heat dissipation, canopies attenuate the effect of incoming solar radiation reducing the effect of radiation on land surface temperature.

c) Because of high latent heat of vaporization of water, the relative cooling effect generated by losing a given percent of soil moisture (latent heat losses) is stronger than the cooling effect produced by the same percent decline in air temperature or radiation.

CHAPTER 1: Sensitivity of surface temperature to radiation, air temperature and soil moisture for soils with and without canopy cover

Abstract

Increasing surface temperatures have widespread ecological, societal, and economic consequences and have been attributed to surface moisture deficits in some regions and to increased energy inputs in others. The complex interaction between the geophysical factors that drive land surface exchanges of moisture, momentum and energy control the relative sensitivity of surface temperatures to hydro-climatic inputs such as radiation, air temperature and precipitation. Warming induced by the absorption of short and long wave radiation may be enhanced or reduced by non-radiative processes such as conductive and convective heat fluxes of sensible and latent heat. These fluxes are facilitated by soil moisture availability, and by surface properties such as its aerodynamic roughness. In this study we use a linearized form of the surface energy budget to calculate analytical surface temperature elasticities and attribute the relative sensitivities to radiative and non-radiative factors for a vegetated and a bare soil land surface in a semiarid climate. We found that relative surface temperature sensitivity to soil moisture is highest during the day for soils with and without canopy cover and often become the most important modulating factor. However, elasticity to radiation is largest in bare soils while elasticity to air temperature increases in soils under canopies and becomes a dominant factor at night and under conditions when evaporation is limited.

1.1 Introduction

One of the most salient effects of greenhouse gas emissions is the global increase of air temperature and long wave radiation emissions from the atmosphere (Hegerl et al., IPCC 2007), which affect weather patterns and the hydrologic cycle. At regional and local scales, variations in precipitation have been widely studied (e.g. Gehne et al., 2016; Trenberth & Shea, 2005), with documented impacts on soil moisture dynamics (e.g. D'Odorico & Porporato, 2004; Hsu et al., 2017). These climate variations affect the surface energy balance at local scales. Changes in soil surface temperature induced by energetic imbalances can outpace those of air temperature and increase the likelihood of short duration extreme temperature peaks at the soil-atmosphere interface. In urban environments, more sustained, frequent or intense surface temperature events can become a hazard for sensitive groups. Outside urban environments, thermal stress on trees can increase the intensity and extent of wildfires (e.g. Holden et al., 2018; Kitzberger et al., 2017; Westerling, 2016) or forest die-offs (e.g. Allen et al., 2010; Anderegg et al., 2012; Breshears et al., 2005). Extreme surface temperatures can also induce ecosystem collapse and transition by suppressing recovery after disturbance (e.g. Davis et al., 2019; Rother & Veblen, 2016), or by altering the soil biochemical cycles that sustain the ecosystem (Neary et al., 2005).

The mechanisms that determine the response of surface temperature to specific hydro-climatologic drivers are complex and depend on land surface properties. Radiation, air temperature, and precipitation are commonly identified as the key atmospheric variables that drive variations in land surface temperatures from sub-daily to decadal scales (e.g. Good et al., 2017; Lean, 1997; Lean & Rind, 1998; Trenberth & Shea, 2005). However, surface properties of different land use and land covers (LULC) control the sensitivity of surface temperatures to each of these drivers by modulating the exchanges of energy, momentum and moisture between land and the atmosphere (Oleson et al., 2004; Pielke et al., 2002). For instance, while incoming solar shortwave radiation constitutes the largest energy input to the climate system (Budyko, 1969; Schwingshackl et al., 2018) surface albedo determines how much of this shortwave radiation is absorbed by the surface and contributes to increasing its temperature.

Surface properties play an important role on the non-radiative (conductive and convective) controls on surface temperatures and determine the reapportion of available net radiation into latent, sensible and ground heat fluxes. The dynamics of this partitioning is driven by soil moisture (e.g. Hauser et al., 2017; Miralles et al., 2012; Schwingshackl et al., 2017), especially during summer (Fischer et al., 2012; Samset et al., 2019). Changes in the volume, timing and intensity of precipitation events will affect soil moisture dynamics and therefore the surface energy balance.

Assessments of surface temperature dynamics that only look at single atmospheric or land use factors can therefore be inaccurate and end up informing policies that may be counter to the aims of mitigation or adaptation. Using direct ground observations, remote sensing, and/or modeling, long and short term variations in surface temperatures have been attributed to changes in incident shortwave radiation (Donohoe et al., 2014; Wild, 2016) , to changes in the surface parameters that facilitate convective energy exchanges (e.g. Boisier et al., 2012; Bright et al., 2017; Luyssaert et al., 2014; Rigden & Li, 2017), to soil moisture deficits (Berg et al., 2014; Miralles et al., 2014; Whan et al., 2015), or to a combination of all these factors (Dentener et al., 2013; Erfan Haghighi et al., 2018). Most attribution studies, however, are inconclusive (Ingram, 2006; Stone & Allen, 2005) because disentangling the individual contribution of each geophysical feedback to observed variations in surface temperature is difficult when these hydro-climatic drivers covary. This is especially true for empirical studies because the overlapping effects of individual drivers are aggregated in the observed response of surface temperature.

A way to make the problem of attribution more tractable is to decompose the equations of the surface energy balance to separate the effects of individual components (Luyssaert et al., 2014; Rigden & Li, 2017; Zhao et al., 2014). In this approach radiative and non-radiative effects are partitioned using normalized first order partial derivatives with respect to the hydro-climatic drivers of interest. We use this analytical methodology to study the sensitivity of surface temperature to variations in air temperature, radiation and soil moisture. We specifically focus on the modulating effect of soil moisture and its potential role in mitigating the effects of increasing air temperatures and radiative inputs on bare soil surfaces and soils under canopies.

1.2 Methodology

1.2.1 Linearized surface energy budget

The surface energy balance equation (SEB) for a small layer of the topsoil states that net radiation (R_n) must equal the sum of latent heat flux (LE), sensible heat flux (H), ground heat flux (G), and heat flux advected by rain (H_r):

$$R_n = -LE - H - G - H_r \tag{1}$$

Our calculation of turbulent fluxes (LE and H) in Eq. (1) uses a forced convection formulation based on the Monin-Obukhov similarity theory to parameterize aerodynamic resistance. We assume that thermal and momentum roughness lengths are identical (neutral atmosphere). In addition to the aerodynamic resistance term, our formulation accounts for the soil resistance to evaporation following Passerat De Silans et al. (1989). Ground heat diffusion through the topsoil layer is simulated using the force-restore method (Liebethal & Foken, 2007) with soil thermal conductivity and soil thermal capacity being functions of the water content in the soil. The energy balance includes the effects of vegetation canopies and permit to study vegetation feedbacks on surface temperatures. If present, vegetation effects on the soil energy balance include canopy interception of precipitation, attenuation of shortwave radiation (shading), emission of longwave radiation, enhanced aerodynamic resistance, and soil moisture uptake by transpiration. All terms in Eq. (1) are functions of surface temperature. The equations describing all fluxes in Eq. (1) are presented in Appendix A.

The LE and R_n terms are nonlinear in surface temperature because the calculation of saturated vapor pressure of soil ($e_s{*}$) and surface irradiance ($\xi_s \sigma_s (T_s + 273.2)^4$) are nonlinear. To allow a direct non-iterative solution of surface temperature, we produce a linear version of Eq. (1) by linearizing these two components using a Taylor Series Expansion:

$$R_n{}^* = -LE^* - H - G - H_r \tag{2}$$

Where $R_n{}^*$ is linearized net radiation and LE^* is linearized latent heat flux based on saturated vapor pressure of soil evaluated at temperature of air (T_a), $\frac{de_s^*}{dT}|_{Ta}$ (Appendix B).

The linearized version of Eq. (1) permits to obtain a direct solution of soil surface temperatures (T_s):

$$T_s^t$$
$$= \frac{\left(H_r + Rn^* + \left(\lambda_o + \Gamma_a * \Delta_{Ta} + \frac{r_o}{r_a + r_{exp}}\right) * T_a + \Gamma_a * e_a^* * (R_H - 1) + \left(\frac{d_s * C_s}{dt} - \frac{G_d}{(\omega * dt)}\right) * T_s^{t-1} + \left(G_d - \frac{G_d * d_s * \omega * dt}{d_o}\right) * T_d^{t-1}\right)}{\lambda_o + \Gamma_a * \Delta_{Ta} + \frac{r_o}{r_a + r_{exp}} + \frac{d_s * C_s}{dt} - \frac{G_d}{(\omega * dt)} + G_d - \frac{G_d * d_s * \omega * dt}{d_o}} \quad (3)$$

Where $\lambda_o = 4\xi_s\sigma_s(T_a + 273.2)^3$ is the linearized portion of irradiance evaluated at T_a, $\Gamma_a = \frac{r_o\beta}{\gamma(r_a+r_s)}$ is effective conductance that incorporates aerodynamic resistance effects in a neutral atmosphere, $r_o = \rho_{air}c_{air}$, $e_s^* \sim e_a^* - \frac{de_s^*}{dT}|_{Ta} * (T_s - T_a)$ is the linearized saturated soil vapor pressure term evaluated at T_a, and $\Delta_{Ta} = \frac{de_s^*}{dT}|_{Ta}$. A full list of symbols and descriptions are provided in Table 1.

Soil surface temperatures calculated from the linear energy balance are a good approximation of the temperatures obtained from the original non-linear energy balance (Appendix D). This linearized solution permits a mathematical analysis of the surface energy balance equations that reveals the contribution of individual hydro-climatic factors to the observed instantaneous variations of soil surface temperatures.

Table 1. List of symbols		
Symbol	Description	Units
α_s	Albedo of surface	0-1
β	Function of soil moisture to calculate pore relative humidity	-
c_a	Heat capacity of air	J kg^{-1} ^{o}C^{-1}
c_p	Heat capacity of solid soil particles	J kg^{-1} ^{o}C^{-1}
c_w	Heat capacity of water	J kg^{-1} ^{o}C^{-1}
C_s	Soil volumetric heat capacity	J m^{-3} ^{o}C^{-1}
d_s	Hydrologically active soil depth	m
d_o	Soil temperature damping depth	m
dt	Time step size	s
e_a	Vapor pressure of air at elevation z$_a$	Pa
$e_s{}^*$	Saturated vapor pressure in soil	Pa
ξ_c	Emissivity and absorptivity of canopy	0-1
ξ_s	Emissivity and absorptivity of surface	0-1
γ	Psychrometric constant	Pa ^{o}C^{-1}
G	Ground heat flux at surface	Wm^{-2}
G_d	Ground heat flux at depth d$_o$	Wm^{-2}
H	Sensible heat flux	Wm^{-2}
H_t	Height of canopy cover	m
κ	Von Karman constant	-
K_a	Thermal conductivity of air	Wm^{-1}K^{-1}
χ	Beer's law exponential attenuation coefficient	-
K_s	Thermal conductivity of soil	ms^{-1}
K_p	Thermal conductivity of soil particles	Wm^{-1}K^{-1}
K_w	Thermal conductivity of water	Wm^{-1}K^{-1}
LAI	Leaf area index	-
LE	Latent heat flux	Wm^{-2}
LE^*	Linearized latent heat flux	Wm^{-2}
l_m	Average separation of leaves in canopy	m
λ	Brooks Corey pore size distribution	-
λ_v	Latent heat of vaporization	J kg^{-1}
n	Soil porosity	-
ω	Frequency of sinusoidal wave	s^{-1}
P	Precipitation	ms^{-1}
r_a	Aerodynamic resistance	sm^{-1}
r_s	Soil resistance to latent heat transfer	sm^{-1}
r_r	Random roughness (small scale) of the surface terrain	m
r_{exp}	Aerodynamic resistance within canopies	sm^{-1}
R_H	Relative humidity of the atmosphere at elevation z$_a$	-
R_n	Net radiation of the soil surface	Wm^{-2}
$R_n{}^*$	Linearized net radiation of the soil surface	Wm^{-2}
H_r	Heat advected by rain	Wm^{-2}
ρ_a	Density of air	Kg m^{-3}
ρ_w	Density of water	Kg m^{-3}
ψ_{ae}	Soil air entry pressure	m
S	Effective relative soil saturation	-
σ	Stefan Boltzmann constant	Wm^{-2}K^{-4}
t	time	s
T_a	Temperature of air	^{o}C
T_c	Temperature of canopy	^{o}C

T_d	Soil temperature at damping depth	°C
T_m	Temperature of melting point of water	°C
T_s	Temperature of soil surface	°C
θ	Volumetric soil water content of d_s	$m^3 m^{-3}$
θ_{fc}	Volumetric soil water content at field capacity	$m^3 m^{-3}$
θ_r	Residual volumetric soil water content	$m^3 m^{-3}$
u_a	Wind speed at reference elevation z_a	ms^{-1}
z_a	Reference elevation for atmospheric conditions	m
z_d	Zero-plane displacement height	m
z_o	Roughness height of the overstory	m
zd_o	Zero-plane displacement for overstory	m
zo_o	Roughness height of overstory	m
z_t	Apparent sink of heat/momentum/vapor	m

1.2.2 Surface temperature elasticities

The four key hydro-climatic factors that are expected to vary with climate change are incident shortwave radiation, incident longwave radiation, variations in soil moisture that reflect variations in precipitation inputs, and variations in air temperature. An analysis of the linearized SEB budget permits to attribute relative instantaneous sensitivities of soil surface temperatures to each of these components.

An application of the chain rule provides the instantaneous sensitivities of surface temperature ($\frac{dT_s}{dt}$) to changes in soil moisture (θ), air temperature (T_a) and radiative forcing: incoming shortwave radiation and incoming longwave radiation (S_{down}, L_{down}).

$$\frac{dT_s}{dt} = \frac{\partial T_s}{\partial \theta}\frac{d\theta}{dt} + \frac{\partial T_s}{\partial T_a}\frac{dT_a}{dt} + \frac{\partial T_s}{\partial S_{down}}\frac{dS_{down}}{dt} + \frac{\partial T_s}{\partial L_{down}}\frac{dL_{down}}{dt} \tag{4}$$

The first factor in each term of the right-hand side in Eq. (4) represents the magnitude of contribution of dynamic variations in the corresponding variables to variation of T_s. These factors, however, cannot be directly compared to estimate relative sensitivities because they are not dimensionally consistent. Normalization of the sensitivity factors is accomplished by dividing the differentials by their mean values by to obtain dimensionless elasticities:

$$\varepsilon_{SM} = \frac{\partial T_s}{\partial \theta} * \frac{\bar{\theta}}{\overline{T_s}} \tag{5}$$

$$\varepsilon_{Ta} = \frac{\partial T_s}{\partial T_a} * \frac{\overline{Ta}}{\overline{T_s}} \tag{6}$$

$$\varepsilon_{Ldown} = \frac{\partial T_s}{\partial L_{down}} * \frac{\overline{L_{down}}}{\overline{T_s}} \tag{7}$$

$$\varepsilon_{Sdown} = \frac{\partial T_s}{\partial S_{down}} * \frac{\overline{S_{down}}}{\overline{T_s}} \tag{8}$$

Where ε is surface temperature elasticity of the variable indicated in the subscript. Appendix E shows the analytical form of the partial derivatives which we use to guide our interpretation of the results. Appendix E, Eq. (E1) presents partial derivative of Eq. (5), Eq. (E2) presents partial derivative of Eq. (6), Eq. (E3) presents partial derivative of Eq. (7) and Eq. (E4) presents partial derivative of Eq. (8). These analytical solutions help us partition dominant processes controlling surface temperature elasticities to variables of interest. The overbar denotes the time average of the corresponding variable (arithmetic mean of the time series). Elasticity represents the percent change that surface temperatures incur for a percent change in the attributing variable and are therefore normalized sensitivities that permit direct comparison between variables.

A key question is how the dependencies between these variables are resolved. If we consider an independent assumption, for example T_s as a function of soil moisture (θ) and air temperature (T_a), $T_s(\theta, T_a)$, then the derivative of T_s with respect to θ is simply:

$$\frac{dT_s}{d\theta} = \frac{\partial T_s}{\partial \theta}$$

However, if there is a dependency between the variables for example air temperature is also a function of soil moisture, $T_s(\theta, T_a(\theta))$, then the total derivative of T_s with respect to θ becomes:

$$\frac{dT_s}{d\theta} = \frac{\partial T_s}{\partial \theta} + \frac{\partial T_s}{\partial T_a}\frac{\partial T_a}{\partial \theta}$$

Where the term $\frac{\partial T_s}{\partial T_a}\frac{\partial T_a}{\partial \theta}$ absorbs the indirect dependency of T_s to soil moisture via its effect on T_a. The methodology can, therefore, fully determine the partial attribution to one hydro-climatic variable given constant values in all other parameters and drivers. To investigate the interaction between pairs of covarying hydroclimatic drivers (e.g., soil moisture (θ) and air temperature (T_a), we reconstructed sections of the functional elasticity space that plot the elasticity surfaces for any combination of soil moisture (θ) and air temperature (T_a). An analysis of the partial derivatives functions using standard calculus methods allow mechanistic insight into the dominant radiative

and non-radiative terms of the SEB that control surface temperature variations (sensitivity functions presented in Appendix E).

1.2.3 Model setup, study plot and atmospheric inputs

We conduct a simulation study in a well-watered lawn plot located in the city of Missoula, MT (USA). The study plot is characterized by gravelly and sandy loams with physical parameters as in Table 2. The region has a dry continental climate with hot summers and large diurnal temperature variations. Lawn in the plot was 0.1 m high. A meteorological station was installed in the summer of 2019 and recorded atmospheric input conditions averaged at 3-hour time intervals over the summer from July 24 to September 30 (Figure 1 & Appendix C). The study period is characterized by a mix of clear sky and overcast days, high temperature diurnal variations, low air relative humidity and wind speeds. The model was parameterized and run using the same soil and meteorological conditions for bare soils and for soil with an overstory canopy. To investigate the robustness of the results we reconstructed the soil temperature elasticity spaces for a wide range of temperature and soil moisture, air temperature, radiation and wind speed conditions.

Table 2. Soil, vegetation and surface parameters for the study plot, units are in parenthesis.	
Parameter	Value
Albedo of surface, α_s (-)	0.15
Emissivity of surface, ξ_s (-)	0.96
Emissivity of canopy, ξ_c (-)	0.95
Height of canopy, H_t (m)	0.1
Light attenuation coefficient, χ (-)	0.92
Leaf Area Index, LAI (-)	2
Random roughness of surface, r_r (m)	0.0015
Soil air entry pressure, ψ_{ae} (m)	0.84
Porosity, n (-)	0.4559
Soil residual water content, θ_r (-)	0.05
Soil pore size distribution, λ (-)	8
Damping depth, d_o (m)	0.0776
Solid soil particle heat capacity, c_p (J Kg^{-1}°C^{-1})	2819400
Soil temperature at damping depth, T_d (°C)	20
Thermal conductivity of soil particles, K_p (Wm^{-1}K^{-1})	1.4

Figure 1. Comparison of meteorological inputs during entire study period (July 24 to September 30, 2019) including (a) air temperature, (b) precipitation, (c) relative humidity, (d) radiation, and (e) wind speed shown as 3-hourly averages.

1.3 Results and Discussion

1.3.1 Diurnal dynamics of soil surface temperature elasticities

Elasticity of soil moisture, ε_{SM}, Eq. (5) , had the largest negative values and largest diurnal fluctuations in bare soils (Figure 2a), suggesting that since soil moisture does not change diurnally, it was a control that operated in conjunction with other processes operating with a diurnal cycle. The largest instantaneous absolute elasticity occurred during the mid-day hours and was also associated with elasticity of soil moisture. Unique to ε_{SM} is that it switches sign and becomes positive at night-time when evaporative cooling became weaker and relative importance of soil moisture in providing soil thermal inertia increased. At the end of the summer, ε_{SM} decreased as latent heat losses due to evaporation were reduced and soil heat storage capacity declined with drier soils. Soil moisture is the main source of variation of soil thermal properties at diurnal time scales (Cheruy et al., 2017), controlling thermal inertia and soil response to energy inputs and also controlling evaporative cooling when convection is not a limiting factor for latent heat transfers. The modulation of surface temperatures provided by soil moisture is therefore tied to diurnal energy cycles of energy availability and turbulent mixing.

Surface temperature elasticity of incoming longwave radiation, ε_{Ldown}, Eq. (7), had the highest absolute average value on bare soils (Figure 2a) and also showed less pronounced diurnal cycles, indicating that in the absence of a protective canopy surface temperature was most responsive to variations in incoming longwave radiation both during nighttime and daytime. On the other hand, air temperature elasticity of soil temperature, ε_{Ta}, Eq. (6), in bare soils showed ample diurnal variations. Like ε_{SM}, ε_{Ta} also flipped sign and becomes negative during the early evening hours (Figure 2a). This counter-intuitive behavior was produced by the lag between diurnal air temperature and surface temperature peaks. Heat capacity and thermal inertia of air is lower than that of soils, which will continue increasing its temperature when air temperatures drop at dusk or maintain relatively low soil temperatures when air temperatures increase at dawn. This effect disappeared in the energy balance under canopies (Figure 2b). Under canopies, the shading reduces radiative energy inputs and evaporation. Sensible heat exchanges become more dominant than radiative and latent heat exchanges, increasing the direct feedback between surface and air temperatures.

Given the leaf area index and canopy emissivity/absorptivity (Table 2) prescribed in this experiment ε_{Sdown}, Eq. (8), became a more important factor than ε_{Ldown} (Figure 2b) because the canopy was more effective in absorbing atmospheric longwave radiation than it was in intercepting shortwave radiation (see Eq. (E3) & (E4) in Appendix E). Overall, our results reveal that the impact of canopies reduced the sensitivity of surface temperatures to all factors but increased the relative control of soil moisture on surface temperatures over the rest of the variables.
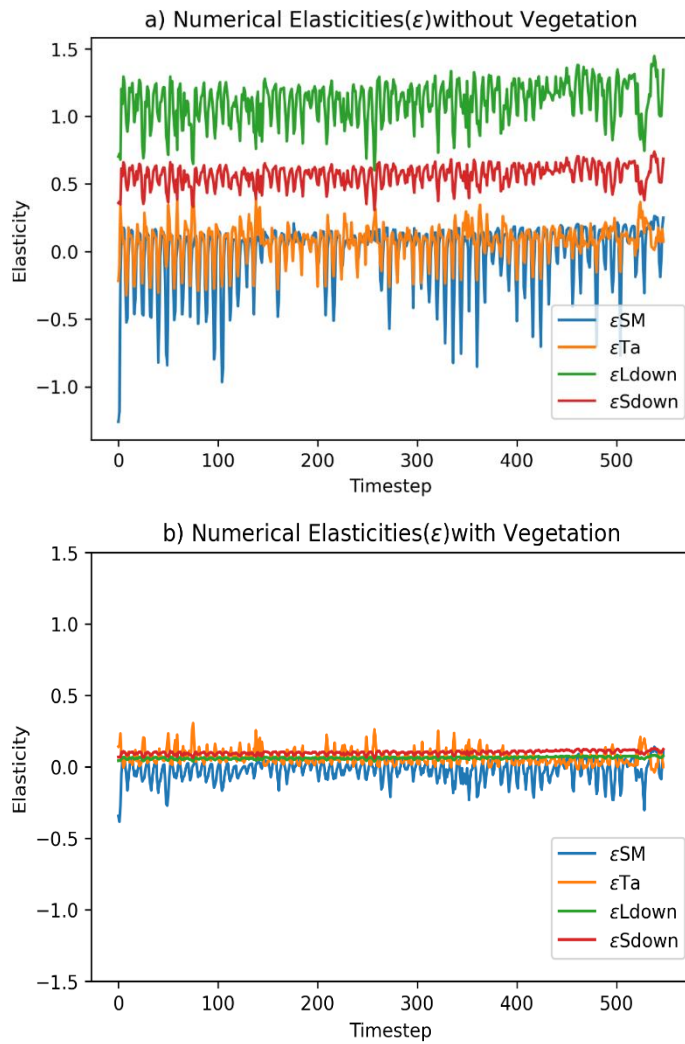
Fig 2. Bare soil (a) and a vegetated landcover (b) T_s elasticity (%) of soil moisture (blue), air temperature (orange), incoming longwave radiation (green) and incoming shortwave radiation (red) from July 24 to September 30, 2019 under meteorological conditions presented in Figure 1.

1.3.2 Functional elasticity spaces for a bare soil surface
- **How do changes in incoming shortwave radiation affect soil moisture modulation for bare soils?**

The functional elasticity spaces in Figures 3-6 provide general insight into the evolution of key changes in surface temperature elasticities, their dependency on hydro-climatic variables of interest and partitioning of available energy at the land surface. It permits to answers questions related to the interaction of factors such as how changes in incoming shortwave radiation or windspeed affect ε_{SM}. Panels in Figure 3a-c show a reconstruction of elasticity surfaces as a function of soil water content, air temperature and three shortwave radiation scenarios.

Under low shortwave radiation loads such as late in the evening or early in the morning, the soil temperature sensitivity to soil moisture (Eq. (5)) becomes positive over most of soil moisture and air temperatures ranges (Figure 3a, 1st row). This happened when inputs of energy declined, less energy was dissipated due to evaporation more was available to keep soils warmer at night due to high heat storage capacity of moist soils. These results are consistent with ones reported by Cheruy et al. (2017) and Kumar et al. (2014) showing the effects of soil thermal inertia from moist to dry conditions and with our previous analysis using the time series of sensitivities in our study plot.

Generally, ε_{SM} becomes more negative as shortwave radiation increases (Figure 3b-c, 1st row). The most sensitive region (purple) centered around soil moisture value of 0.21 and over a wider range of air temperature values. This sensitive region is governed by the empirical wetness function (β) that determines water availability for evaporation. The importance of soil moisture in controlling soil temperatures through evaporative cooling decline past this point because the supply of water to atmosphere becomes less limiting. Such response to soil moisture variations in bare soils is attributed to and associated with pore-scale mechanisms governing vapor diffusion from soil pores into the atmosphere (Haghighi; & Kirchner, 2017; E. Haghighi & Or, 2013). At intermediate and high shortwave radiation levels, the elasticity of soil moisture stays relatively constant over a wide range of air temperatures, which suggest that radiative inputs are more efficient than sensible energy inputs controlled by air temperature to generate conditions that enhance latent heat losses and increase the importance of ε_{SM}. In any case, the level of soil moisture above which evaporative losses became insensitive to changes in soil moisture depends on atmospheric conditions (Gu et al. (2006)).

$\varepsilon_{Ta}, Eq.(6)$ increased non-linearly with air temperature and soil moisture values but decreased with incident shortwave radiation (Figure 3a-c, 2nd row). Values of ε_{Ta} became negative for most combinations of air temperature and soil moisture when insolation reached 900 Wm^{-2}. In the linearized version of energy balance, air temperature is used to approximate radiative surface temperatures and this caused the negative elasticities. At high insolation levels, the soil surface

reaches temperatures that make radiative cooling an increasingly more efficient heat dissipation mechanism than convective exchanges.

The last two rows of Figure 3 illustrated that both ε_{Ldown}, Eq. 7 and ε_{Sdown}, Eq. (8) do not change in response to changing radiation scenarios as expected but exhibited a general pattern of higher elasticities (yellow) at low soil moisture levels meaning that the radiative control on surface temperatures became more dominant then. A decrease in surface temperature sensitivity to radiative controls at higher air temperature and soil moisture levels (purple) on the other hand meant that convective exchanges became more dominant at those levels.

Overall, the surface temperatures were most sensitive to soil moisture under changing radiation scenarios than other drivers. These sensitivities in bare soils were dominated by radiative controls at low soil moisture and air temperature levels and by convective exchanges at higher ones. Higher soil moisture levels greatly restrict the increase in surface temperature as available energy is consumed in evaporation (Nemani et al., 1993).
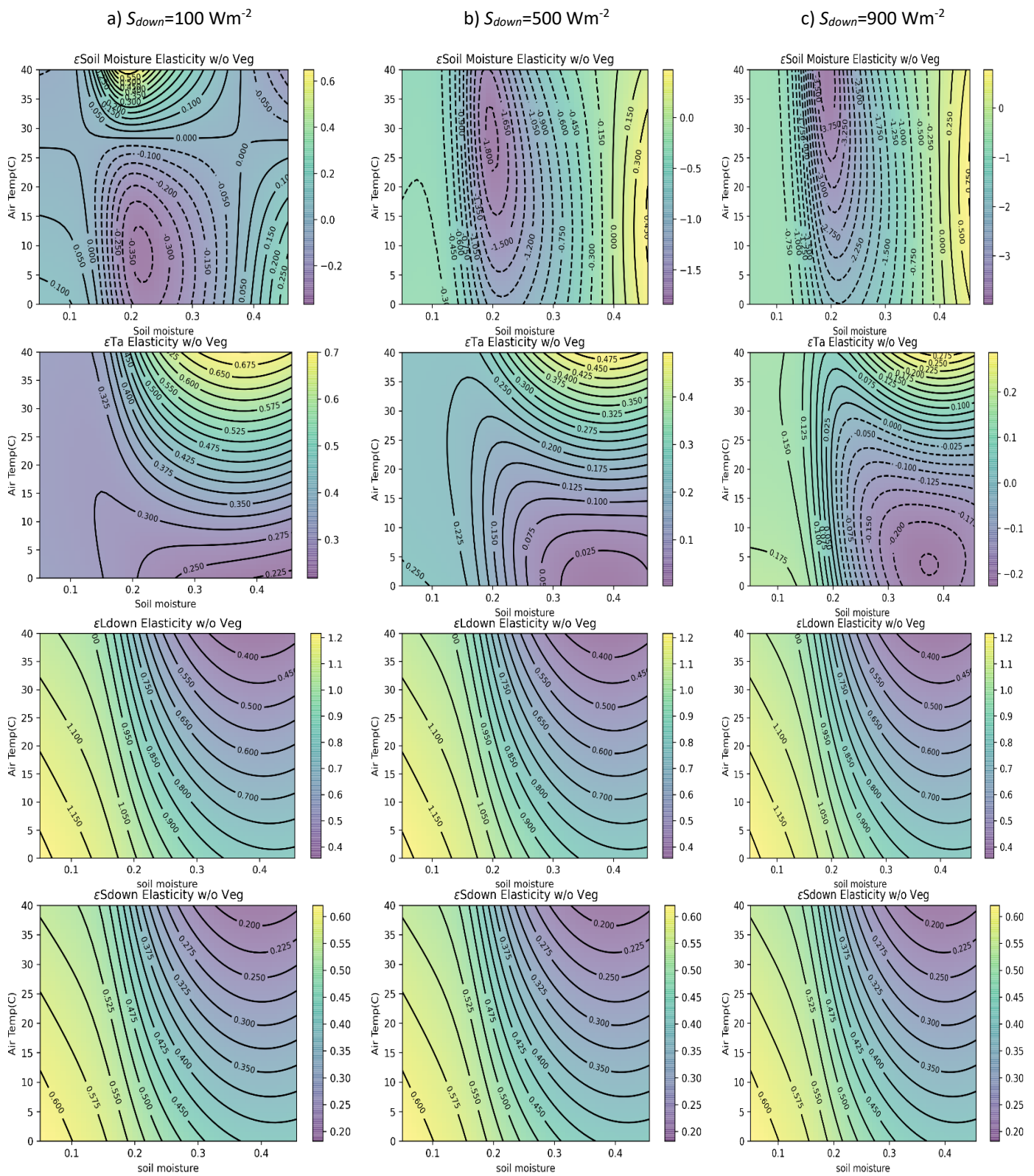
Fig 3. Elasticity spaces of soil moisture (ε_{SM}), of air temperature (ε_{Ta}), of incoming longwave radiation (ε_{Ldown}) and of incoming shortwave radiation (ε_{Sdown}) (first, second, third and fourth row, respectively) as a function of soil water content, air temperature and three varying S_{down} scenarios at 100 Wm^{-2}(a), 500 Wm^{-2}(b) and 900 Wm^{-2}(c) (first, second and third column, respectively) for a bare soil surface. The rest of hydro-climatic drivers remain constant through all three scenarios where L_{down}=300 Wm^{-2}, wind speed=2.0 ms^{-1}, relative humidity of air=0.55 and temperature of the canopy=10°C. High elasticity values are in yellow, medium in green and low in purple. Solid contour lines are positive elasticities and dashed contours are negative elasticities.

- **How do changes in wind speed affect soil moisture modulation for bare soils?**

The efficiency of cooling induced by convective exchanges is strongly influenced by wind conditions, surface water availability and surface roughness lengths (Appendix A, Eq. (A9) & (A12)). Changes in wind speed affect the efficiency of convective exchanges through its effect on aerodynamic resistance (Appendix A, Eq. (A14) & (A16)). Regional scale studies in bare soils reveal that turbulent heat fluxes are primarily dominated by wind speed variability (Bertoldi et al., 2007). The magnitude of ε_{SM} increased nonlinearly with wind speeds, with the biggest impacts occurring when wind speeds increased from low speeds (Figure 3a-c, 1st row). Increasing wind speed also increased the sensitivity of ε_{SM} to variations in soil moisture, producing a steeper elasticity surface as soil moisture converged toward the volumetric water contents level of maximum sensitivity. Maximum ε_{SM} occurred at soil moisture levels of about 0.21 and relatively high air temperatures, when latent heat dominated sensible heat losses at these optimal temperature and soil moisture conditions.

Sensitivity to air temperatures, ε_{Ta} increased and became increasingly positive as wind speed increased (Figure 4a-c, 2nd row). At high wind speeds, the soil surface reaches temperatures that make sensible heat losses an increasingly more efficient heat dissipation mechanism than latent heat or radiative exchanges. This partially explains the narrowing of the soil moisture region that keeps ε_{SM} at maximum levels observed in Figure 3a-c 1st row. The decline of the relative importance of radiative controls with respect to convective processes is apparent in the third and fourth rows of the figure, where both ε_{Ldown} and ε_{Sdown} decreased as wind speed increased.

Fig 4. Elasticity spaces of soil moisture (ε_{SM}), of air temperature (ε_{Ta}), of incoming longwave radiation (ε_{Ldown}) and of incoming shortwave radiation (ε_{Sdown}) (first, second, third and fourth row, respectively) as a function of soil water content, air temperature and three varying wind speed scenarios at 0.5ms[-1](a), 2.0ms[-1](b) and 5.0ms[-1](c) (first, second and third column, respectively) for a bare soil surface. The rest of hydro-climatic drivers remain constant through all three scenarios where $S_{down=}$ 700 Wm[-2], L_{down}=300 Wm[-2], relative humidity of air=0.55 and temperature of the canopy=10°C. High elasticity values are in yellow, medium in green and low in purple. Solid contour lines are positive elasticities and dashed contours are negative elasticities.

1.3.3 Functional elasticity spaces for canopies

- **How do changes in incoming shortwave radiation affect soil moisture modulation for canopies?**

Differences in the sensitivity of surface temperature to the considered hydro-climatic factors between a bare soil and a vegetated landcover are most apparent in the overall magnitude of elasticities, which are significantly reduced in the presence of a canopy cover (Figure 5). Vegetation significantly alters the surface energy balance partitioning between radiative and non-radiative processes (Eq. (1)) and is affected by the presence of specific biophysical parameters associated with canopies such as leaf area index, which determines the extent of the transpiration surface, the amount of water and light interception, and the aerodynamic resistance to turbulent exchanges between the surface and the free atmosphere above the canopy.

The sensitivity of surface temperature to soil moisture, ε_{SM} (Figure 5a-c, 1st row), increases modestly with increasing insolation compared to bare soil conditions due to the effects of reduced energy availability caused by shading and by the additional aerodynamic resistance imposed by the canopy (Appendix A, Eq. (A16)), both of which suppress latent heat transfers. At the same time, the range of air temperature values over which ε_{SM} remains high are reduced when canopy is present compared to bare soil conditions (Figure 4a-c, 1st row). The modulation of surface temperature provided by soil moisture under canopies, mostly through evaporative cooling, is stronger than the effect on soil temperature from variations in radiative inputs. This result is consistent with other studies such as Duveiller et al. (2018), who show that reduction in available energy at the surface does not counter-balance the increase in temperature associated with reduction in transpiration.

The effect of canopies did not change the qualitative features of the ε_{Ta} surface under increasing radiation scenario (Figure 5a-c, 2nd row). Under canopies as discussed earlier, the shading reduces radiative energy inputs and evaporation enhancing the importance of sensible heat exchanges and increasing the direct feedback between surface and air temperatures.

Shortwave radiation had no significant effect on the elasticities of longwave and shortwave radiation, ε_{Ldown} and ε_{Sdown}, (Figure 5a-c, 3rd & 4th row), however, these elasticities were significantly smaller than for bare soil conditions.

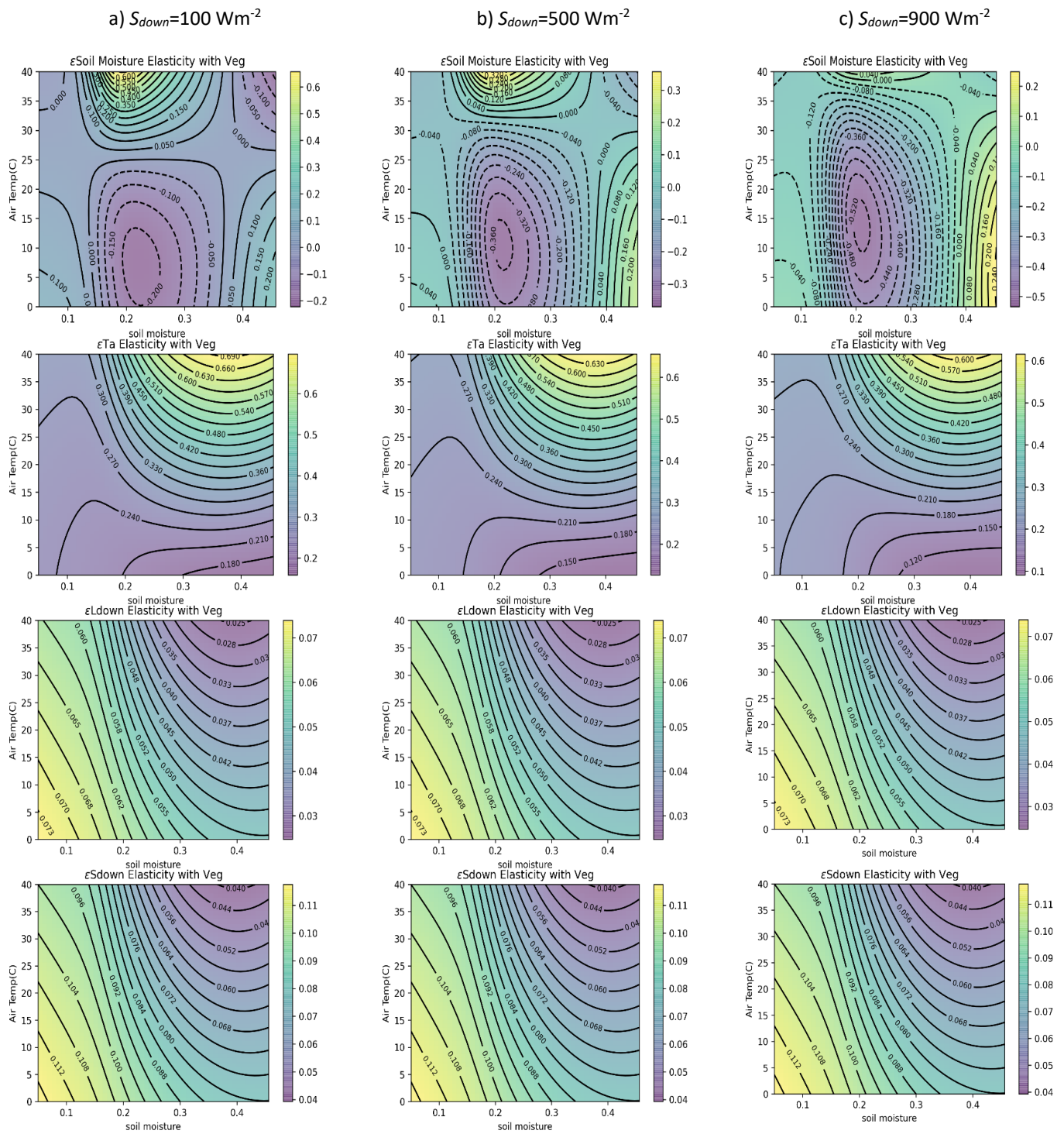Fig 5. Elasticity spaces of soil moisture (ε_{SM}), of air temperature (ε_{Ta}), of incoming longwave radiation (ε_{Ldown}) and of incoming shortwave radiation (ε_{Sdown}) (first, second, third and fourth row, respectively) as a function of soil water content, air temperature and three varying S_{down} scenarios at 100 Wm^{-2}(a), 500 Wm^{-2}(b) and 900 Wm^{-2}(c) (first, second and third column, respectively) for a canopy. The rest of hydro-climatic drivers remain constant through all three scenarios where L_{down}=300 Wm^{-2}, wind speed=2.0ms^{-1}, relative humidity of air=0.55 and temperature of the canopy=10°C. High elasticity values are in yellow, medium in green and low in purple. Solid contour lines are positive elasticities and dashed contours are negative elasticities.

- **How do changes in wind speed affect soil moisture modulation for canopies?**

Similarly, to the case of bare soils, wind speed increased the sensitivity of surface temperature to soil moisture variations (increasing absolute values of ε_{SM} with wind speeds, Figure 6a-c, 1st row) due to enhancements in turbulent latent heat transfer during evaporation. However, the effect is of a smaller degree than bare soils because turbulent energy transfers are partially suppressed by the additional aerodynamic resistance imposed by canopies. The sensitive region became restricted over smaller range of soil moisture levels for same reasons as previously discussed under changing wind speeds in bare soils (Figure 4a-c, 1st row).

On the other hand, the elasticity of air temperature, ε_{Ta} (Figure 6a-c, 2nd row), under canopies increases with wind speed at a faster rate than for bare soils (Figure 4a-c, 2nd row). This increase in sensitivity is also illustrated in the temporal evolution of ε_{Ta} in Figure 2b for a canopy landcover and is attributed to a rebalancing of turbulent exchanges toward sensible heat at the expense of latent heat. ε_{Ldown} and ε_{Sdown} decreased (Figure 6a-c, 3rd & 4th rows) for similar reasons as explained in bare soils (Figure 4a-c, 3rd & 4th rows).

Overall, the modulating effect of soil moisture on surface temperature is greater when wind speeds are high enough to generate sufficient forced convection than when the availability of radiative energy increases. However, the sign of ε_{SM} and the relative importance of factors depend on the presence of a canopy cover (e.g., ε_{Ldown} dominating in bare soils but lower than ε_{Ta} when canopies are included) highlighting potential mechanisms through which canopy cover can decouple soil and atmospheric climates and provide ecosystem resilience.
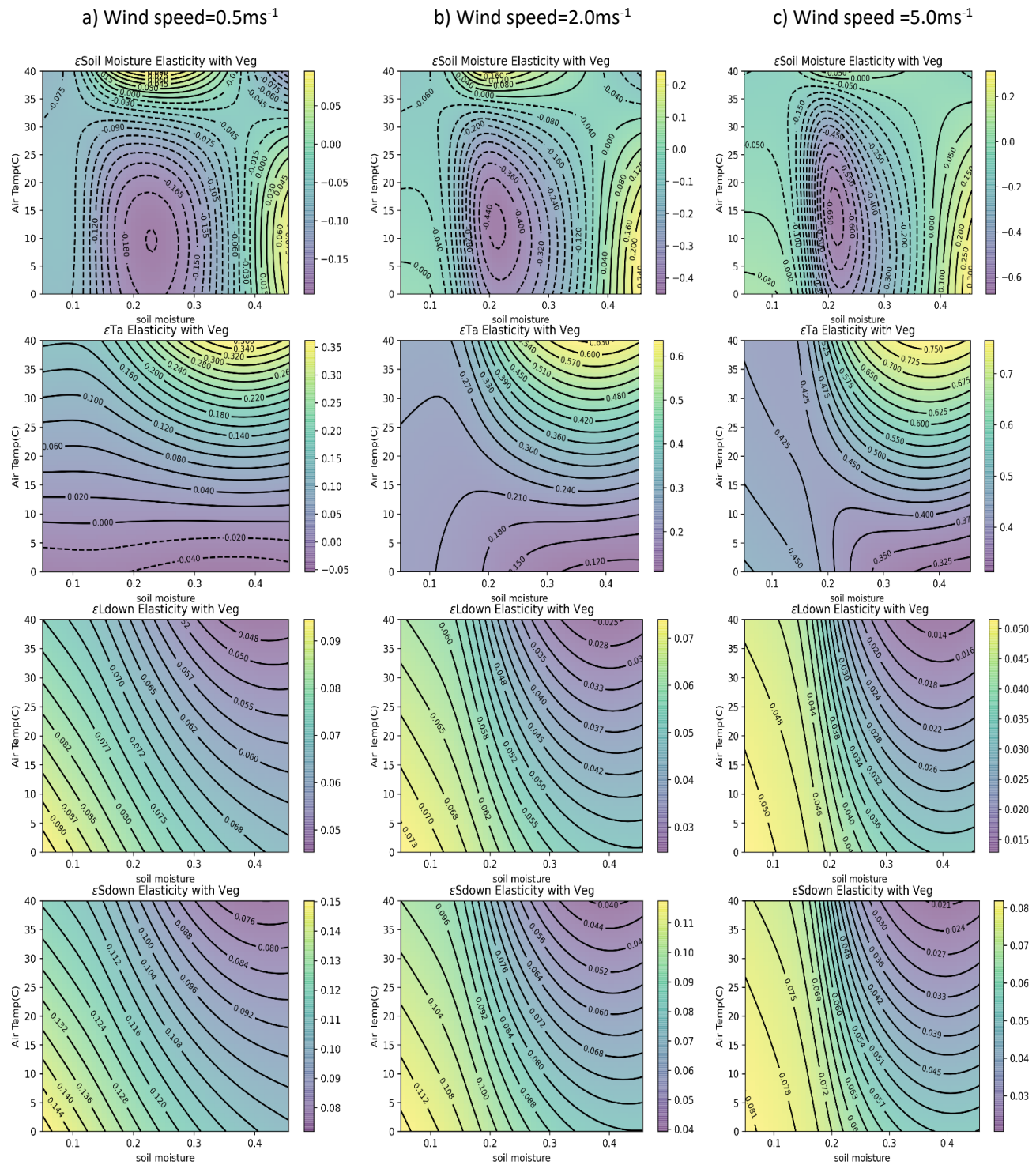
Fig 6. Elasticity spaces of soil moisture (ε_{SM}), of air temperature (ε_{Ta}), of incoming longwave radiation (ε_{Ldown}) and of incoming shortwave radiation (ε_{Sdown}) (first, second, third and fourth row, respectively) as a function of soil water content, air temperature and three varying wind speed scenarios at 0.5ms^{-1}(a), 2.0ms^{-1}(b) and 5.0ms^{-1}(c) (first, second and third column, respectively) for a canopy. The rest of hydro-climatic drivers remain constant through all three scenarios where $S_{down=}$ 700 Wm^{-2}, L_{down}=300 Wm^{-2}, relative humidity of air=0.55 and temperature of the canopy=10°C. High elasticity values are in yellow, medium in green and low in purple. Solid contour lines are positive elasticities and dashed contours are negative elasticities.

1.4 Summary, conclusions and future work

In this study we proposed a method to determine the sensitivity of surface temperature dynamics to key hydroclimatic drivers under the presence and absence of vegetation canopies at local scales. Using this method, we calculated the dynamics of the sensitivity of surface temperature in a study plot and identified the dominant factors controlling soil temperature dynamics. Our results permit us to address the original hypotheses posed on page 5 and confirm hypothesis (a) that soil moisture emerged as a key control, playing a pivotal role in partitioning available energy between radiative, conductive, and convective exchanges and controlling the thermal properties of the soil. While we showed that for a grass canopy cover, the attenuation provided by leaf area and aerodynamic resistance did in fact reduce convective exchanges of latent heat, hypothesis (b), we also showed that it reduced incoming shortwave radiation, evaporative losses of heat and water leading to an overall reduction of the sensitivity of surface temperature to climatic drivers. Lastly, the relative cooling affect of losing a given percent of soil moisture was shown to be stronger than the cooling affect produced by the same percent decline in air temperature or radiation, hypothesis (c), in Figure 2a-b. However, this was not only due to the high latent heat of vaporization but also due to how water vapor is conducted in response to hydro-climatic drivers.

Feedbacks between energy exchange processes result in modification of the importance of the mechanisms that make soil temperature sensitive to specific drivers. This makes it difficult to accurately attribute changes in surface temperature to specific causes outside the range of condition used during the analysis. However, our findings illustrate that in over the wide range of conditions used in our analysis, soil moisture was the dominant control through its role in reapportioning of the surface energy balance between turbulent heat fluxes. Given the complex (nonlinear) interactions among surface energy balance components, further considerations are required for generalizing this study to all possible conditions. This can be accomplished using a similar analysis on the non-dimensionalized form of the linearized energy balance equation, which presents an opportunity for future research.

CHAPTER 2: Urban surface temperature distribution in response to water input regimes for varying land covers using an ecohydrological model: A case study in Missoula, Montana, USA

Abstract

In this study we show that soil surface temperature increases in an urban semiarid environment are strongly modulated by precipitation and by land cover properties that enhance latent heat losses. To evaluate the net impact of precipitation on surface temperatures we used a fully coupled energy and water balance model applied at high temporal resolutions during a wet and a dry summer in the city of Missoula, MT. The model tracks the evolution of soil surface temperatures and the partitioning of available radiative energy between conductive fluxes into the ground and turbulent fluxes of sensible and latent heat. The model performance was assessed against USGS land surface temperature estimations from Landsat satellite data. Results show differences of about 2°C between average surface temperatures between the wet and the dry scenarios. In both scenarios surface temperatures were higher where low latent heat exchanges were not sufficient to dissipate excess energy. These hot locations, however, experienced relatively low additional increases in temperature when precipitation declined during the dry year scenario. The largest relative differences in average surface temperature between the wet and dry were in vegetated land covers with relatively high average soil moisture contents. It is in these land cover where declining precipitation had the largest impact on surface temperatures.

2.1 Introduction

Today, about 55% of the world's population lives in urban areas around the world. The fraction is expected to grow to over 68% by 2050 according to the UN (United Nations, 2018). Alterations to the natural environment as a result of the physical structures of buildings, use of materials such as concrete, asphalt, brick, removal of vegetation and residential neighborhood planning results in the formation of distinct urban microclimates (Carlson & Arthur, 2000) by altering surface physical properties, the surface water balance, and the surface-atmosphere exchanges of energy and momentum (e.g. Cook et al., 2012; Grimm et al., 2008; Templeton et al., 2018; Wu et al., 2011). These alterations can sometimes have undesirable effects on the local community, especially in times of extreme climate variations such as extreme heat, droughts, or floods.

In urban environments, summertime precipitation and urban irrigation regimes can help maintain surface temperatures below hazardous levels by reapportioning energy from heating the air and ground to latent heat associated with evaporation and evapotranspiration losses. Changes in precipitation are one of the most noticeable and significant outcomes of a warming atmosphere (Easterling et al., 2017). Precipitation adds moisture to the surface, which is subsequently either

infiltrated into the soil, intercepted and stored in the canopy, evaporated or transpired by vegetation. If the soil cannot hold excess precipitation, it becomes runoff or recharge to groundwater systems. Precipitation plays an important part in the energy balance because the presence of water promotes latent heat expenditures of the available energy (Ward et al, 2018). Despite its control on how the energy balance is reapportioned, the extent to which summer precipitation events modulate extreme variations in surface temperatures in urban environments has not been fully examined.

The Fourth National Climate Assessment Report shows a decline in historical mean annual precipitation in much of West, Southwest and Southeast portions of the US (USGCRP et al., 2018). At the same time the length of dry periods and the frequency of high-intensity precipitation has increased in most of US (USGCRP et al., 2018). Using multiple gridded datasets and observations, Holden et al. (2018) detected that since 1979 the number of consecutive dry days during the May-September period has been growing by more than 20% per decade with direct correlation with increases in wildfire activity (Holden et al., 2018). Distal causes of precipitation declines in the Western US have been attributed to declining Arctic sea ice extent (Stroeve et al., 2012) and subsequent weakening of zonal winds (Francis & Vavrus, 2012; Luce et al., 2013), while the intensification of storms have been associated with the increased holding capacity of warmer air and with positive latent-heat flux feedbacks (Dai et al., 2020).

Recent studies have used a combination of satellite observations, in situ observations and climate modeling approaches to assess the impacts of vegetation on urban climate and hydrology (Meili et al., 2020), varying irrigation regimes in agricultural areas on hot extremes (e.g. Chen & Dirmeyer, 2019; N. D. Mueller et al., 2016; Puma & Cook, 2010; Thiery et al., 2017) and mega heat wave events in urban areas on continental and global scales (e.g. Barriopedro et al., 2011; Fischer et al., 2007; Fischer & Knutti, 2015; Garcia-Herrera et al., 2010; B. Mueller & Seneviratne, 2012; Perkins et al., 2012; Rahmstorf & Coumou, 2011). Still, the degree to which urban irrigation abates extreme surface temperatures at fine spatial and temporal scales remain unexplored.

Understanding the links between land cover types and energy balance processes is critical for urban planning and design purposes (Georgescu et al., 2014), particularly since urban heat islands are affected by the orientation of buildings and urban structures that affect outgoing longwave radiation due to limiting sky-view factor, albedo and losses in natural vegetation that reduce evapotranspiration and hence latent heat losses (Oke, 1982).

Here, we present a modeling approach to construct the contribution of summer June, July, August (JJA) precipitation storms to changes in the distribution of surface temperatures for different urban land covers. We use a mechanistic ecohydrological model, Ech2o (Maneta &

Silverman, 2013) to simulate 30-m spatial and 3-hourly temporal scale water and energy exchanges at the land surface. We validated the model using Landsat satellite surface temperature data provided by USGS and ran the model in a semiarid urban landscape in western Montana.

The goals of this study are to 1) show that urban land covers play an important role in regulating the surface temperature of an urban microclimate and hence affect the relative comfort level of its inhabitants; 2) quantify the role water plays on ameliorating localized heat islands in different urban land covers; and lastly 3) provide modeling results that local land planners can use to assess the impact of drier weather patterns caused by global climate change and plan strategies to mitigate the frequency and duration of extreme heat events.

2.2 Methods and Data

2.2.1 Modeling Framework: Ecohydrological Model, Ech2o

Ech2o (Maneta & Silverman, 2013; Simeone et al. 2018; Kuppel et al, 2018) is a fully distributed ecohydrological model that has three main components 1) a vertical energy balance scheme that simulates soil-vegetation-atmosphere energy dynamics based on flux-gradient similarity theory; 2) a carbon uptake and vegetation phenology component; and 3) a kinematic wave hydrologic module that provides vertical and lateral water transfer and ensures the hydrologic articulation of the landscape (Figure 1).

The model uses the empirical surface energy balance (SEB) approach to calculate surface temperatures (T_s). The solution of the energy balance (Eq. (1)) allocates the available energy into energy used to evaporate water, reduce the cold content of the snowpack (if snow is present), heat the air, and heat the ground (Maneta & Silverman, 2013).

$$\sum_{p=1}^{P}(R_n[p] + \rho_w\lambda_v E[p] + H[p] + G[p] + S[p] + LM[p] + H_r[p])f_p + H_a = 0 \qquad (1)$$

Where R_n is net radiation at the surface (Wm^{-2}), ρ_w is water density (kg m^{-3}), λ_v is latent heat of vaporization water (J kg^{-1}), E is flux of water vapor due to soil evaporation (ms^{-1}), $\rho_w\lambda_v E$ (Wm^{-2}) is latent heat flux into the atmosphere due to soil evaporation, H is sensible heat flux into the atmosphere (Wm^{-2}), G is ground heat flux (Wm^{-2}), S is heat flux into the snowpack (Wm^{-2}), LM is latent heat of snowmelt (Wm^{-2}), and H_r is sensible heat advected by rainfall/throughfall (Wm^{-2}) and H_a is anthropogenic heat flux (Wm^{-2}) averaged over the most populated downtown areas in the study domain (Appendix H). The variable in square brackets [p] indicates that the flux of energy is for the p soil cover type. See Appendix A for detailed definitions and formulations for each of the fluxes.

The model domain is constructed using a gridded digital elevation model that defines the topography and the drainage network and establishes the grid on which the governing equations

are solved (Maneta & Silverman, 2013). Conservation of mass and energy are enforced at each time step and grid cell. Each grid cell in the model can have multiple vegetation types in addition to unvegetated surface areas. The total energy balance for the pixel is calculated by taking the sum of the fluxes for each of the vegetation types weighted by the proportion of the pixel they occupy. For each cell in the domain, the surface energy balance Eq. (1) is solved P times.
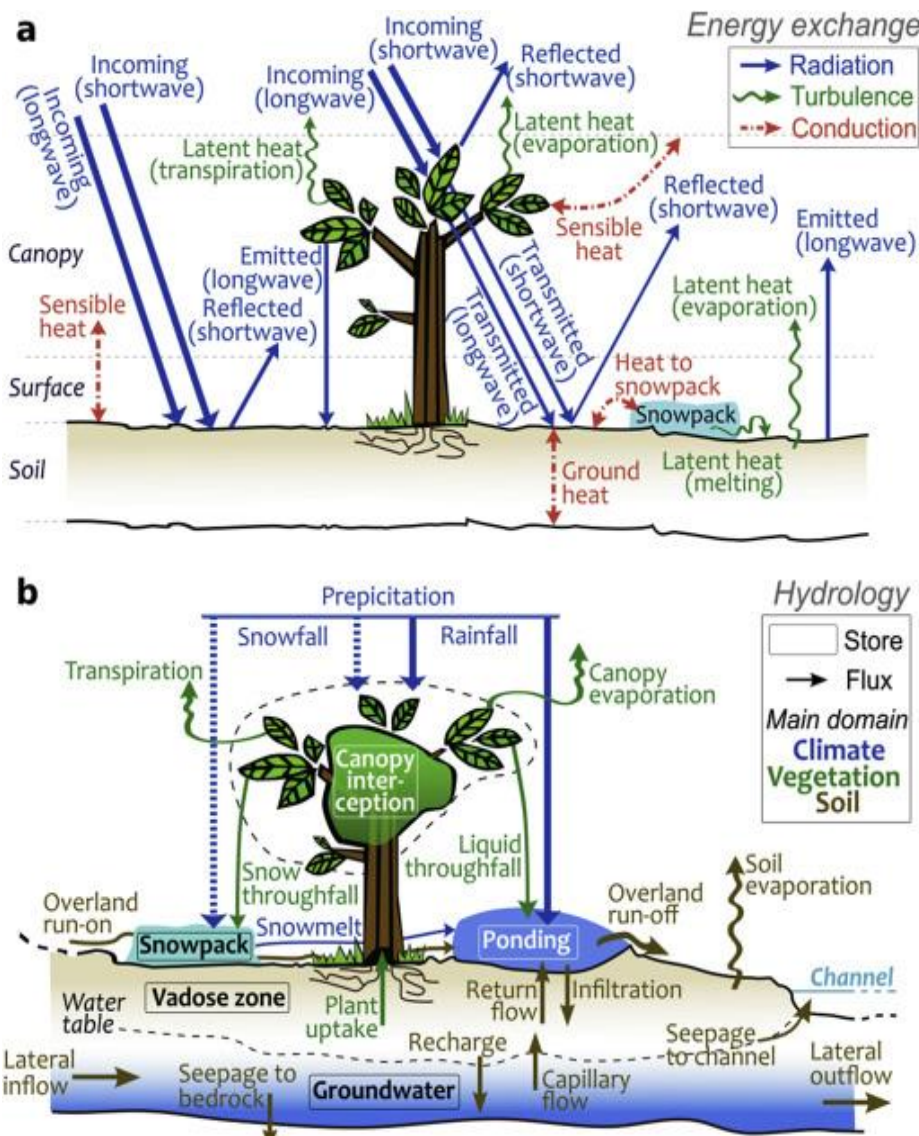

Figure 1. Energy fluxes (a) and hydrologic cycle (b) articulated in Ech2o (Kuppel et al., 2018).

2.2.2 Study Area

We ran the model for Missoula, MT (Figure 2), population of 74,428 residents as of July 1, 2018 (U.S. Census Bureau, 2018) over an area of approximately 90 km^2 (City of Missoula, 2019). The study domain is discretized by 30-m grid cells with surface properties associated with different landcovers (Figure 2). The land use-land change (LULC) classification raster map for Montana was obtained from Montana government's official geodatabase collection developed by Sanborn and NWGAP (University of Idaho). The baseline map was adapted from the Northwest ReGAP project land cover classification, which used 30-m resolution multi-spectral satellite imagery (Landsat ETM+) between 1999 and 2001.Vegetation classes were from the Ecological System Classification developed by NatureServe (Comer et al., 2003) and the land cover classes were developed by Anderson et al. (1976).
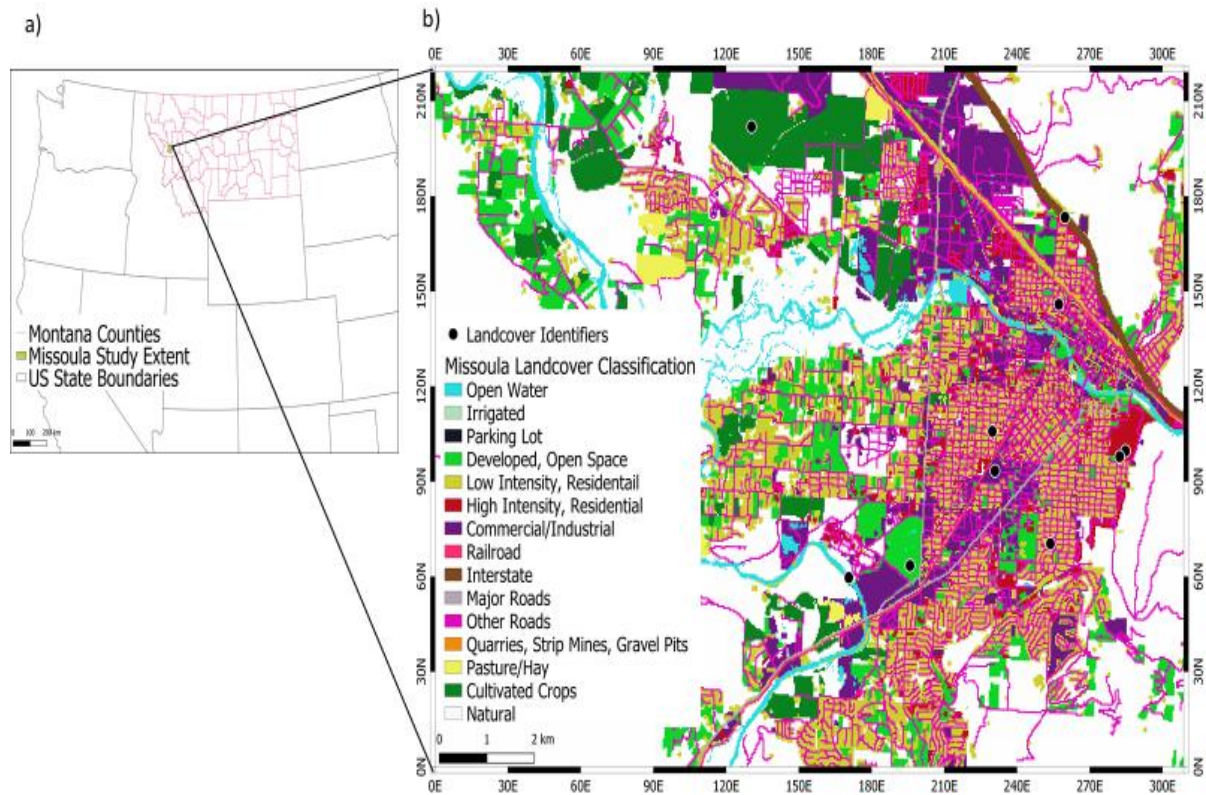
Figure 2. Section map of study area, Missoula, Montana in Western US. a) The green bounding box is the extent of study area within Missoula County; b) different colors represent landcover classifications per Montana Natural Heritage Program, Sanborn, University of Idaho level 2 product, 2016 (https://mslservices.mt.gov). Black circles are single pixels representing selected land cover classes.

2.2.3 Study methods

In order to evaluate the impact of variability of summer precipitation on soil surface temperatures for different landcovers we run the model under the conditions of two distinctive years. We chose 1998 as a wet year and the conditions of 2012 as a dry year based on the number of consecutive dry days. The results we compared to assess differences were the spatial distribution of mean summer (JJA) temperatures. In addition, we run a 'no precipitation' scenario that completely suppresses summer precipitation (Figure 14). This extreme scenario provides a way to evaluate the maximum drought-induced attainable surface temperatures and provides a benchmark to evaluate other alternative scenarios.

2.2.4 Model setup and forcing data

Spatially variable input parameters for the model include remotely sensed data (Landsat), land cover classification data and binary files with climate data.

Geospatial data products and climate data sources used to parameterize and run the model are detailed in Table 1. All geospatial data was projected to the local Universal Transverse Mercator (UTM) coordinate system and resampled to a common raster grid with 30-m spatial resolution.

2.2.5 Meteorological inputs

The spatial distribution of climate data is done according to discrete climate zones with unique identifiers that define areas of the domain with constant values for a given climate input. These climate zones were constructed using a regular grid of 250-m. Input data for each climate zone was obtained from regional climate models as listed in Table 1 at 3-hourly time steps. Climate data used in this study span a period of two years from the end of September through the beginning of October for 2012 and 1998.

Figure 3a-e shows the spatially-averaged time series over the study domain of air temperature, precipitation, air relative humidity, radiative forcing and wind speed during the study period for 2012, which is considered a drier than average year.
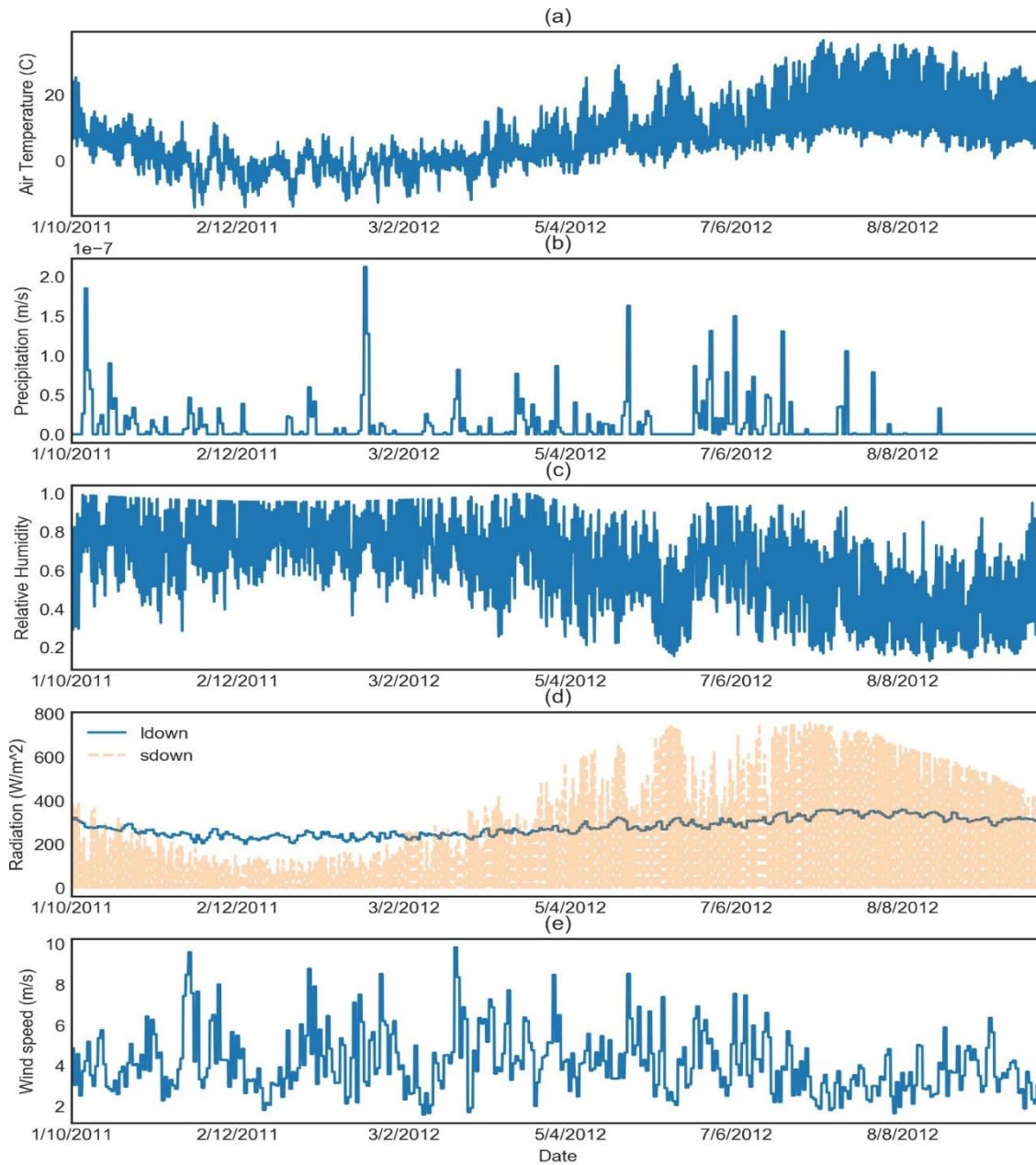
Figure 3. Comparison of spatially-averaged meteorological inputs during entire study period (1 October to 30 September, 2012) including (a) air temperature, (b) precipitation, (c) relative humidity, (d) radiation, and (e) windspeed shown as 3-hourly averages over the entire study domain.

2.2.6 Vegetation parameters

Vegetated landcovers were defined as per the Montana Natural Heritage Program, Sanborn, University of Idaho level 2 product (Figure 2). Here we present only the vegetation parameter data relevant for this study. The area of vegetation occupied in each 30-m pixel was obtained from Multi Resolution Land Characteristics Consortium (MRLC) and developed by U.S. Forest Service for CONUS (Coulston et al., 2012) (Figure 4). This product uses the Random Forests regression algorithm to estimate percent tree canopy cover in each pixel.

Spatially distributed 30-m leaf area index (*LAI*) was calculated following Anderson et al. (2004). Their methodology was adopted using a regression equation to obtain *LAI* from the Normalized Difference Water Index (NDWI). The Landsat satellite bands (Near infrared, NIR and Shortwave infrared, SWIR) were used to calculate NDWI and processed in the Google Earth Engine platform (Figure 5).

Relevant non-spatially distributed parameters (among others) include maximum physiological stomatal conductance of leaf water to the atmosphere (*gs, max*) and optimal environmental efficiency parameters to calculate stomatal conductance. Parameter values were selected on trial-and-error basis during preliminary model runs.
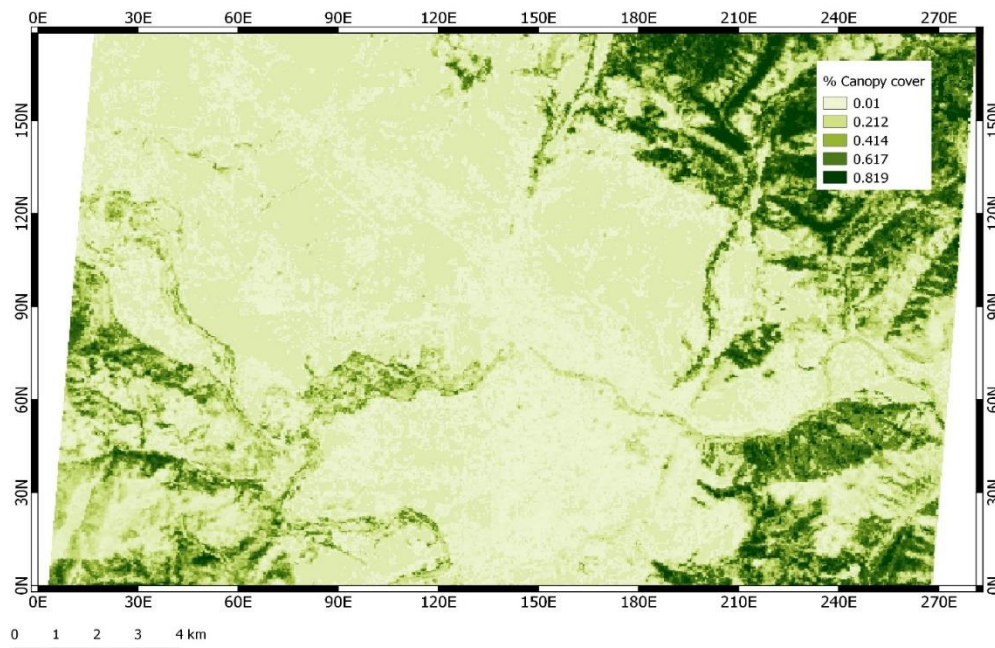
Figure 4. Spatial distribution of the fraction of terrain covered by canopies in study area, NLCD (2011).
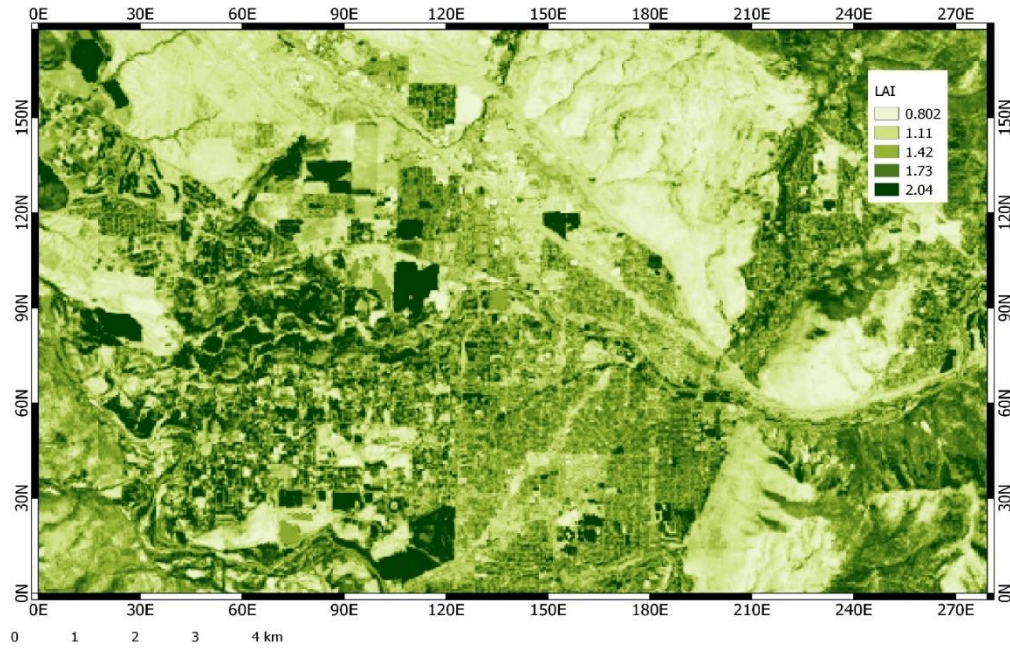
Figure 5. Spatial distribution of leaf area index (LAI) at 30-m resolution following Anderson M.C. et al., 2004 using Landsat 8 (OLI) satellite data and processed with Google Earth Engine platform.

2.2.7 Surface and soil parameters

Soil and surface properties play an important role on the non-radiative (conductive and convective) controls on surface temperatures and determine the reapportion of available net radiation into latent, sensible and ground heat fluxes. A complete list of parameters and their sources is provided in Table 1.

The albedo map at 30-m spatial resolution was calculated following Shuai et al., (2011) using surface reflectance (SR) data from the Analysis Ready Product (ARD), which is atmospherically corrected using LEDAPS and readily available in the Earth Explorer website. SR images were processed in Google Earth Engine platform and masked for clouds. The final summer albedo map used in the model was obtained by averaging SR raster images corresponding to the summer months (JJA) (Figure 6). Surface emissivity (Figure 7) is also available within the same ARD package (Cook et al. 2014) and processed in a way similar to SR.

The map of impervious area, the proportion of surface in each cell that cannot infiltrate water, was estimated from the landcover map assuming that in residential areas only lawns and backyards are impervious.

Spatially distributed soil parameters such as porosity (Figure 8) and others such as hydraulic conductivity, air entry pressure etc are all listed in Table 1. These spatially distributed maps are based on tables by Dingman, 2002 and SSURGO soil classification map for natural areas. They

are then classified accordingly to LCLU maps provided by Sanborn, University of Idaho level 2 product (2016), Figure 1, since SSURGO soil data over urban areas is missing (Appendix G).
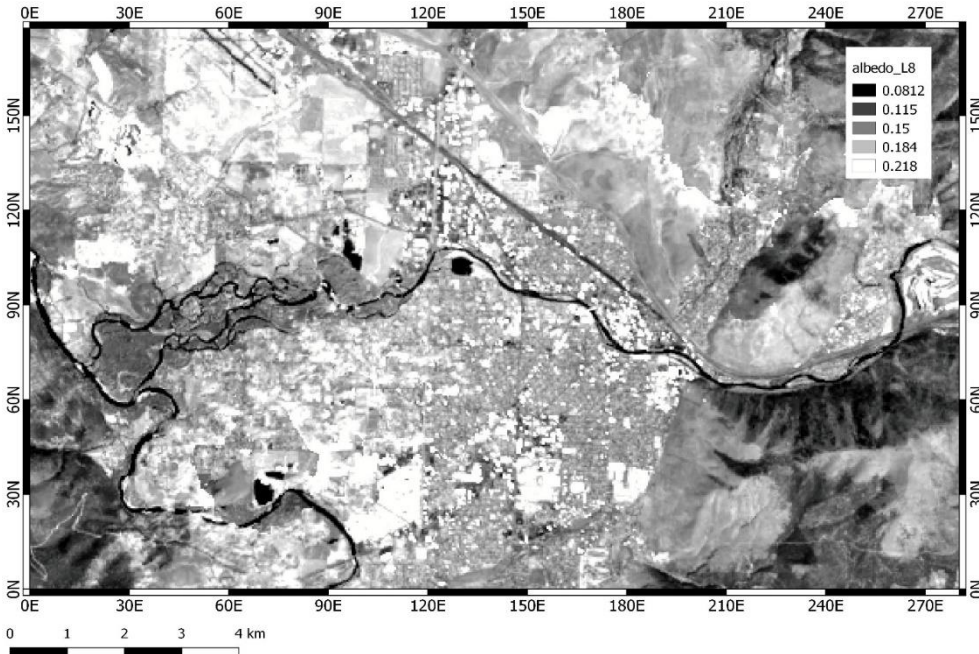

Figure 6. Spatial distribution of albedo at 30-m resolution following Shuai et al., 2011 using Landsat 8 (OLI) satellite data and processed with Google Earth Engine platform.
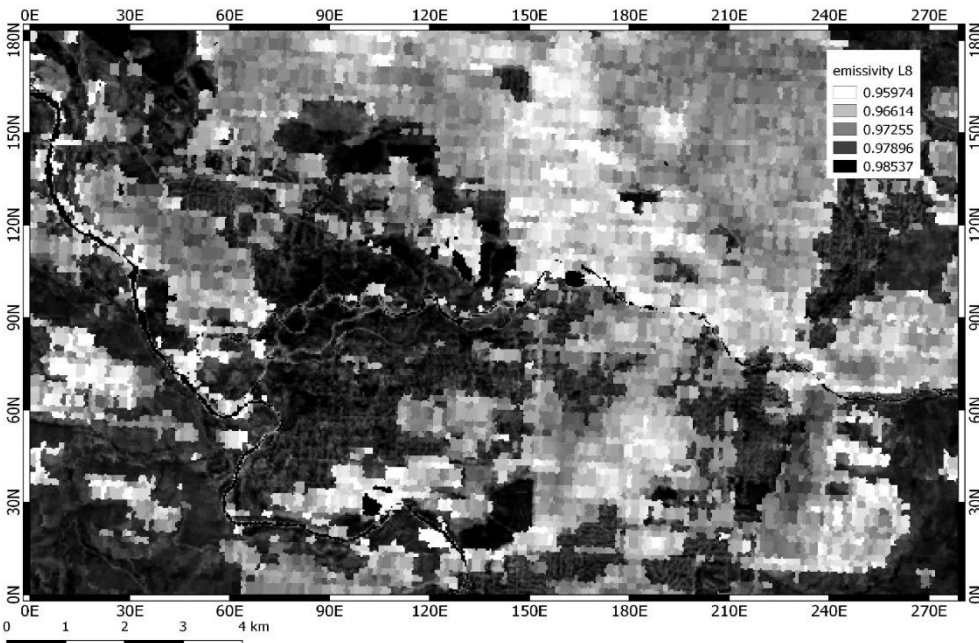

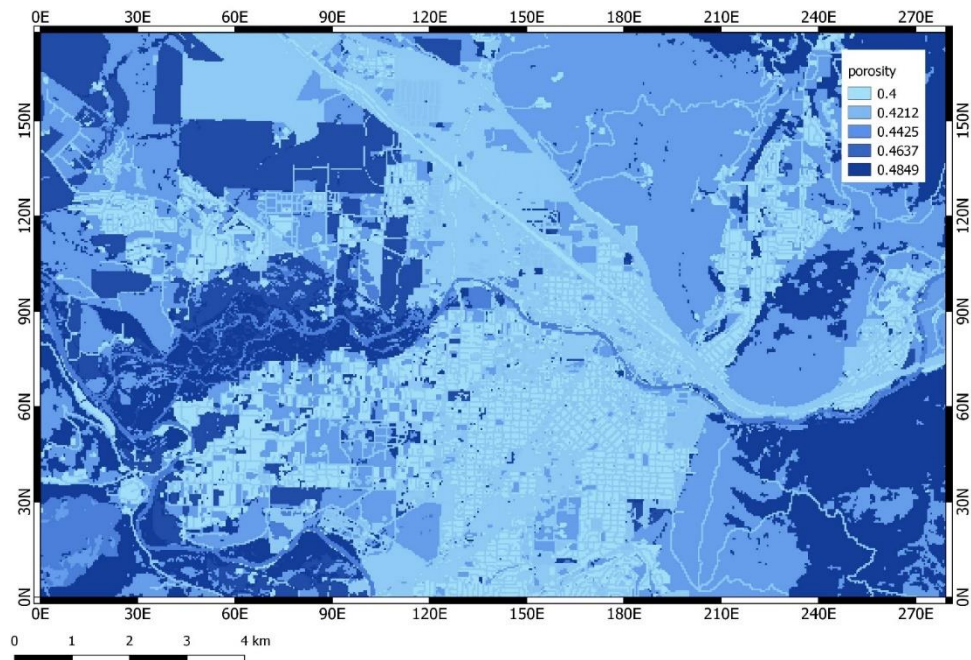Figure 7. 30-m emissivity product provided by USGS ARD using Landsat 7 satellite, based on work by Cook et al., 2014. Image processed in QGIS.

Figure 8. Porosity map created using tables following Dingman, 2002. The values are then allocated to each pixel according to LULC map developed by Sanborn, University of Idaho level 2 product, 2016 (https://mslservices.mt.gov).

Ech2o Inputs-Climate (boundary conditions)	Type	Units	Source
			Table 1. Summary of spatially variable and climate data inputs, units and sources.
Air temperature	Binary	°C	Holden et al., 2019. AMS. A Topographically Resolved Wildfire Danger and Drought Monitoring System for the Conterminous United States.
Incoming longwave and shortwave radiation	Binary	Wm^{-2}	Holden et al., 2019. AMS. A Topographically Resolved Wildfire Danger and Drought Monitoring System for the Conterminous United States.
Precipitation	Binary	ms^{-1}	Daly et al., 1997. AMS. The PRISM Approach to Mapping Precipitation and Temperature
Relative Humidity	Binary	●	Holden et al., 2019. AMS. A Topographically Resolved Wildfire Danger and Drought Monitoring System for the Conterminous United States.
Wind speed	Binary	ms^{-1}	Mesinger et al., 2006. North American Regional Reanalysis
Ech2o Inputs-Spatial			
Digital Elevation Model	Raster	m	USGS, 2000. SRTM (Shuttle Radar Topography Mission 1 Arc-Second Global)
Random roughness	Raster	m	Davenport et al., 2000. AMS. Estimating the Roughness of Cities and Sheltered Country
Saturated hydraulic conductivity	Raster	ms^{-1}	Dingman 2002, p. 235. Values assigned based on Montana Natural Heritage Program's land cover and land use classification product, Sanborn, University of Idaho level 2 product,2016
Porosity	Raster	●	Dingman 2002, p. 235. Values assigned based on Montana Natural Heritage Program's land cover and land use classification product, Sanborn, University of Idaho level 2 product,2016
Pore size distribution	Raster	●	Dingman 2002, p. 235. Values assigned based on Montana Natural Heritage Program's land cover and land use classification product, Sanborn, University of Idaho level 2 product,2016
Air entry pressure	Raster	kPa	Dingman 2002, p. 235. Values assigned based on Montana Natural Heritage Program's land cover and land use classification product, Sanborn, University of Idaho level 2 product,2016
Residual soil moisture	Raster	m^3m^{-3}	Values assigned using Arcmap based on Montana Natural Heritage Program's land cover and land use classification product, Sanborn, University of Idaho level 2 product,2016
Soil layer depth	Raster	m	SSURGO, 2012
Albedo	Raster	●	USGS, 2018. Analysis Ready Product (ARD) processed using Google Earth Engine platform & QGIS
Surface emissivity	Raster	●	USGS, 2018. Analysis Ready Product (ARD) processed using Google Earth Engine platform & QGIS
Specific heat capacity(Soil vol)	Raster	$Jm^{-3}K^{-1}$	Table. Values assigned using Arcmap based on Montana Natural Heritage Program's land cover and land use classification product, Sanborn, University of Idaho level 2 product,2016

Thermal conductivity	Raster	Wm^{-1}K^{-1}	Table. Values assigned using Arcmap based on Montana Natural Heritage Program's land cover and land use classification product, Sanborn, University of Idaho level 2 product,2016
Canopy cover	Raster	•	U.S. Forest Service,2011. National Land Cover Data (NLCD) percent tree canopy cover
Surface Imperviousness	Raster	•	Table. Values assigned using Arcmap based on Montana Natural Heritage Program's land cover and land use classification product, Sanborn, University of Idaho level 2 product,2016
Ech2o- Initial conditions			
Soil water content (soil moisture)	Raster	m^{3}m^{-3}	Values assigned using Arcmap based on Montana Natural Heritage Program's land cover and land use classification product, Sanborn, University of Idaho level 2 product,2016
Soil temperature	Raster	°C	Values assigned using Arcmap based on Montana Natural Heritage Program's land cover and land use classification product, Sanborn, University of Idaho level 2 product,2016
Leaf Area Index	Raster	•	Anderson M.C. et al., 2004. Remote Sensing of Environment. Upscaling ground observations of vegetation water content, canopy height, and leaf area index during SMEX02 using aircraft and Landsat imagery.
Tree height	Table	m	Based on vegetation species (e.g grass height= 0.1m)

2.2.8 Validation

The ability of the model to simulate surface temperatures was validated against Landsat land surface temperature (LST) dataset. Included in the USGS Analysis Ready Product (USGS, 2018), Figure 9. Landsat flyover time is every 16 days at 11 AM local MST time. Six images were available between April and September of 2012 after culling scenes with insufficient quality due to cloud cover.

The model was run directly from the parameters obtained from sources listed above (Table 1) without any type of parameter calibration or adjustment. Our model simulations provide average surface temperatures over the 3-hourly time steps used during model executions. Simulated average temperatures from the time step ending at 12PM were compared with the Landsat LST overpass at 11 AM.

2.3 Results

2.3.1 Comparison of modeled and remotely sensed surface temperatures

Figure 9a shows the 6 images that were available for comparison purposes from April-September 2012 (red dots) between average diurnal daily surface temperatures and Landsat ARD product. A qualitative comparison of modeled (Figure 9b) and Landsat surface temperatures (Figure 9c) show that the temperature range and main elements of the spatial patterns are consistent across main urban and natural landcovers. The model had a consistent surface temperatures bias of about 7°C with respect to the Landsat LST product. A regression between observed and simulated surface temperatures for a random sample of pixels showed a regression coefficient (r^2) of 0.2 (Figure 10c). High surface temperature values are higher than those of the Landsat LST product.
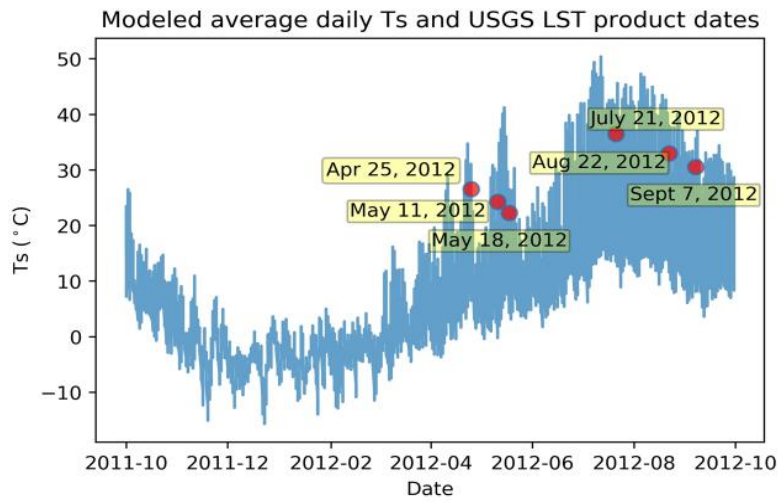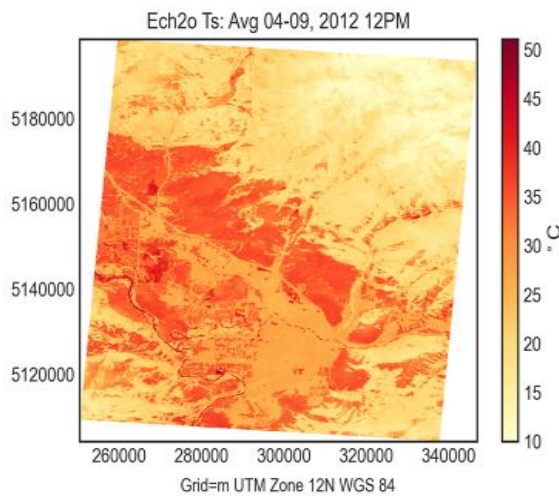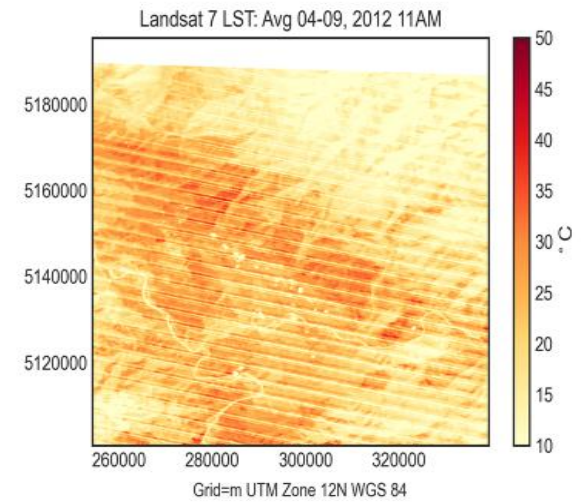
Figure 9. Spatial distribution of mean surface temperatures for selected dates between Apr-Sept of 2012: (a) Average daily simulated *Ts* and USGS LST product availability dates in red dots; (b) Landsat 7 estimation for 6 images and (c) simulated mean for the same days.
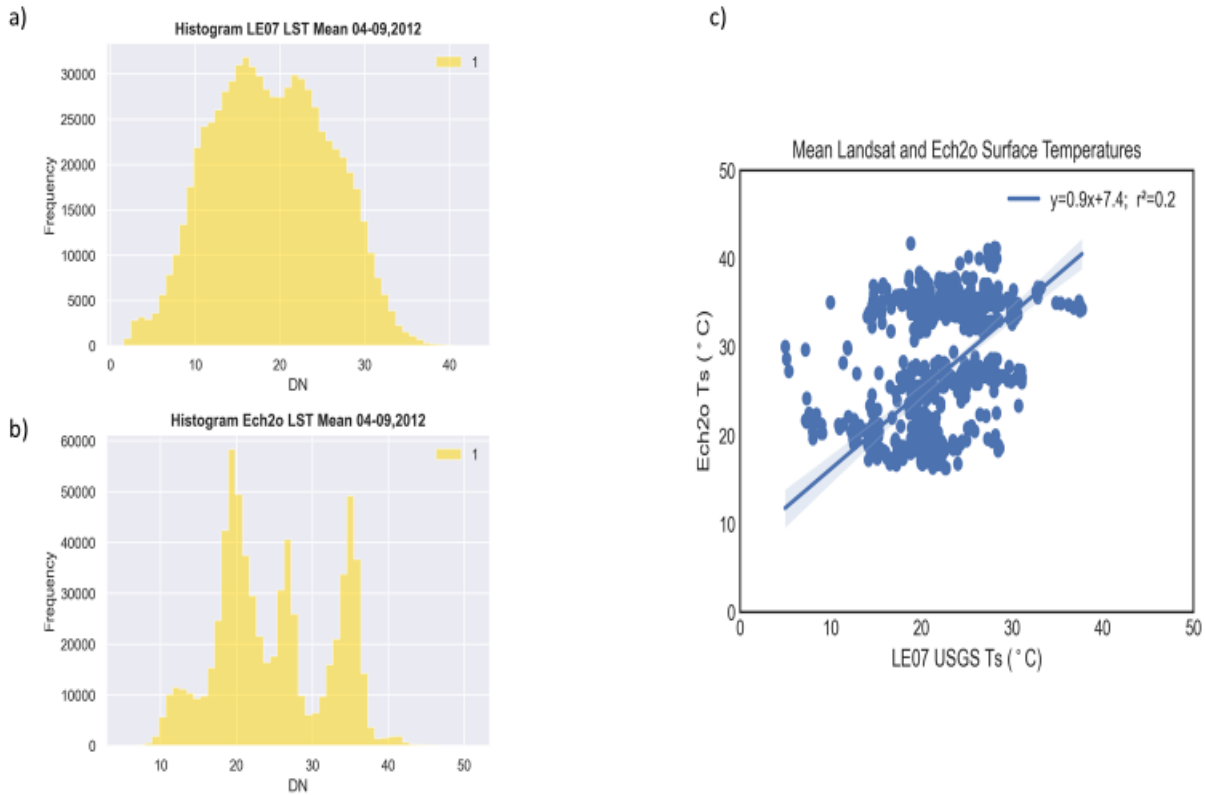
Figure 10. Comparison of pixel distribution within study area of a) Landsat 7 surface temperatures and b) simulated surface temperatures. DN numbers on x-axis represent surface temperature ranges of the histogram bins. A regression of randomly selected pixels between the two rasters (c) show a coefficient of determination of $r^2=0.2$.

2.3.2 Surface temperature dynamics for different landcovers

Time series of temperatures are presented here for a single year (2012) along with precipitation forcing for different selected landcovers as indicated in Figure 2. Overall seasonal trends are as expected, low surface temperatures that reach negative values during winter months from October up until March and then rising during summer months. In winter, there is not much difference in surface temperatures between different landcovers as they all overlap with most prominent landcover in light green representing developed, open spaces such as parks and golf courses (Figure 11). Differences between landcovers become more pronounced during summer months as soil moisture deficits accrue, exacerbated by differences in soil and surface properties. Highest temperatures in summer months appear to be in the interstate and other roads associated with the low albedo of asphalt, which allows it to absorb and retain heat during the day. Roads, therefore, tend to be hotter during the day relative to other surfaces.

The impacts of precipitation events in reducing surface temperatures are apparent in Figure 11. In addition to a reduction in radiation inputs associated with cloudiness during rainy periods, the

addition of water to the surface temporarily increases the soil thermal capacity, enhancing soil thermal inertia and facilitating latent heat energy expenditures through enhanced evapotranspiration. Surface temperatures tend to stay lower for longer periods of time in response to more frequent precipitation events, which is most noticeable in the precipitation events of the month of June. Single precipitation events with high magnitudes result in shorter periods of low surface temperatures, such as the large event that occurred in May, where surface temperatures quickly recovered after the event.
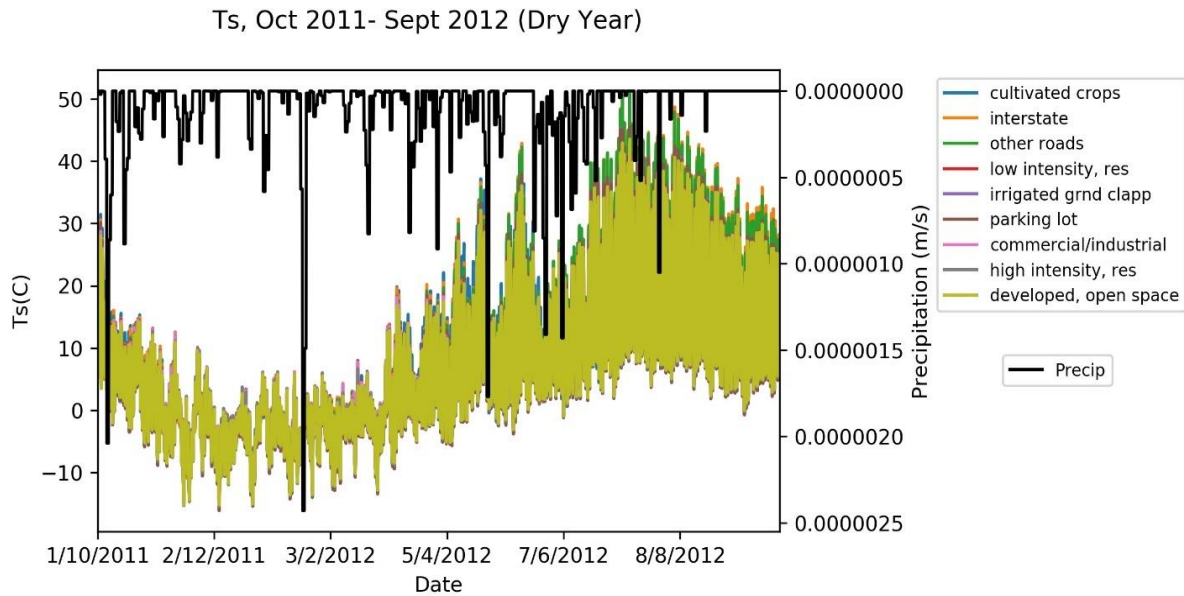
Figure 11. Diurnal and seasonal evolution of surface temperatures for different landcovers, presented in different colors, and precipitation (black) for 2012.

2.3.3 Energy balance components for different landcovers

Different landcovers partition the available energy in different ways, with the majority of the available energy (net radiation) being mostly dissipated as latent (*LE*) and sensible (*H*) heat. Net radiation has the expected seasonality of lower net radiation values during winter months due to reduced insolation, increased cloud cover and increased albedo because of snow on the ground (Figure 12a). Net radiation increases significantly during summer months starting April. Land covers with the highest positive and negative net radiation peaks during the summer are associated with roads and are due to low albedo and the higher absorptivity and emissivity of the asphalt surfaces. Diurnal negative net radiation values during summer occur at nighttime when outgoing longwave radiation is emitted from asphalt surfaces with high emissivity. Diurnal

38

values are highest between 4-6AM and lowest between 4-6PM coinciding with local sunrise and sunset times.

Peaks in latent heat flux are correlated with storm events with the exception of a large precipitation snow event in February (Figure 12b). The largest peak in latent heat flux occurs in June and July when the frequency of precipitation is also high and is associated with a combination high transpiration fluxes from fully developed crops (dark blue), lawns and other irrigated sites (light green).

Sensible heat fluxes are highly variable for the study period, with the largest fluxes occurring in May and July and low with summer values in June corresponding to a period with frequent precipitation events (Figure 12c). Variability in sensible heat fluxes between land covers was also more apparent during the summer, with highest positive sensible heat fluxes associated with roads (Figure 12c). Negative (outgoing) fluxes in the winter occur when cold air masses pass over a relatively warm urban surface, the sensible heat exchange between the surface and the overlying air is significantly enhanced. On the other hand, when warm air masses flow over the city, they usually significantly decrease the amount of heat lost from the surface. When advection of warm air occurs in winter, or after relatively cold periods, the surface gains heat from the overlying air and sensible heat fluxes become positive.

Ground heat fluxes exhibit a similar seasonal trend, with lower values in winter and higher in summer (Figure 12d). Unlike turbulent fluxes, positive and negative ground heat fluxes tend to balance over the daily cycle, resulting in relatively small net heat losses through conduction. Due to the high conductivity of wet soils, 'crops' category (dark blue) records the highest ground heat values.
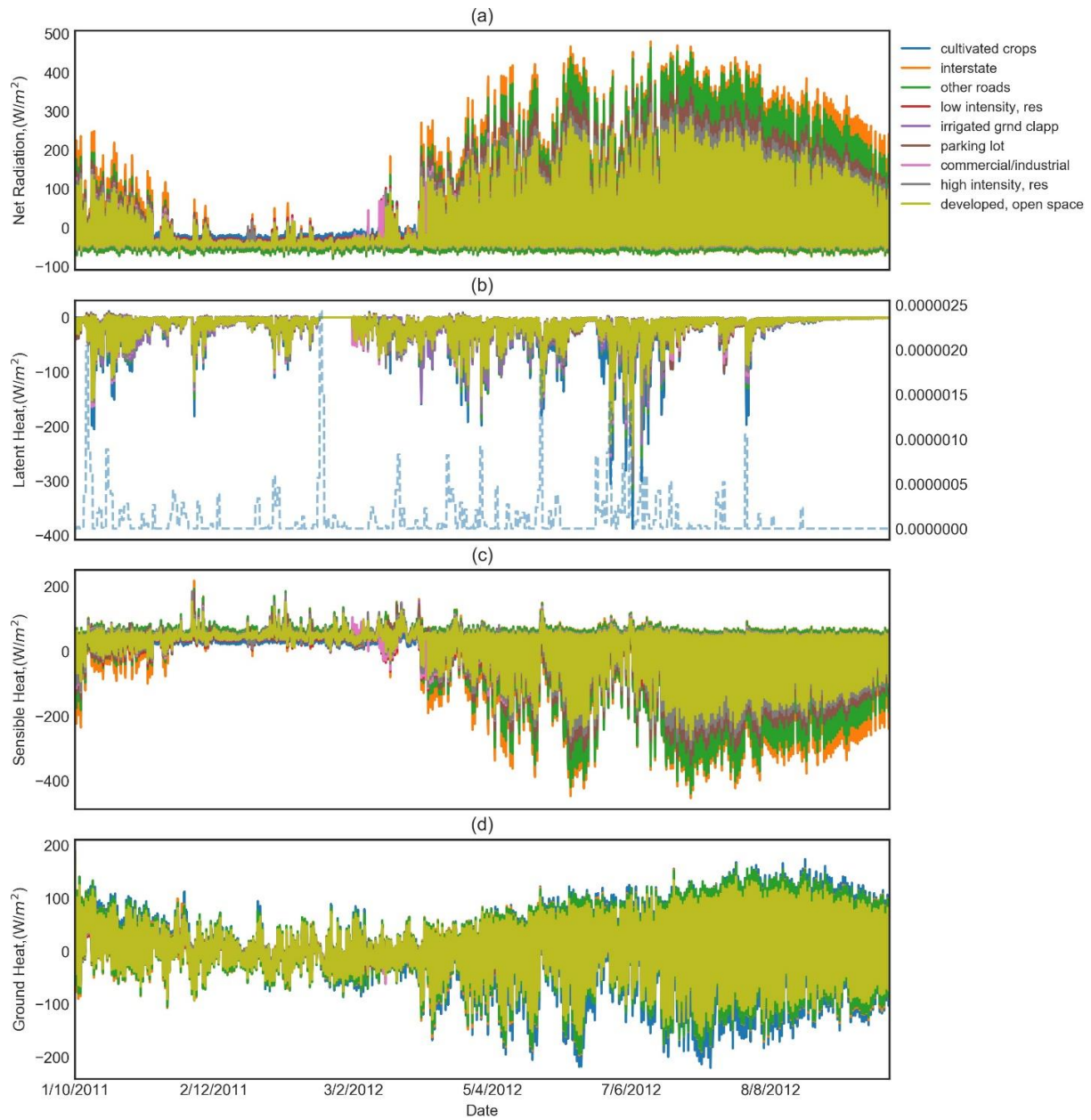
Figure 12. Surface energy balance components for 2012. A) Net radiation for different landcovers which is reapportioned between b) latent heat flux c) sensible heat flux and d) ground heat flux. The dotted blue graph in (b) is rate of precipitation (ms^{-1}).

2.3.4 Spatially distribution of surface temperatures for two contrasting years

The impact of variability in precipitation and its spatial distribution of summer mean (JJA) temperatures for different landcovers is presented in Figure 13. These differences in soil surface temperatures are evaluated for a wet year (1998) and a dry year (2012). There is a high degree of correlation between soil surface temperatures and aspect (e.g., northwest-facing versus southeast-facing slopes) because incoming shortwave radiation is a dominant factor determining surface temperature for the sparsely vegetated (grassy) hills surrounding Missoula.

The spatial patterns of surface temperature between the two years are very similar (Figure 13a-b), however, differences between the two simulations emerge when the net average surface temperatures are analyzed (Figure 13c). Some urban and natural surfaces show a temperature difference of 1.6^{o}C with higher differences for roads, 2.0^{o}C. The highest differences are in the northwest corner of the map, where a difference of up to 2.5^{o}C is apparent. These areas are mostly natural surfaces and croplands and therefore have higher soil moisture content than the built environment. Contrary to that, it is interesting that some natural surfaces such as those in the south east corner of the map have less difference in surface temperatures and this is most likely due to the fact that these surfaces are drier than the ones in the northwest.

Differences in spatially distributed surface temperatures with and without precipitation for a single year are presented in Figure 14. Magnitude of absolute differences under this extreme scenario is greater than Figure 13 as expected. When surfaces are dry and subject to similar meteorological conditions, temperatures variations between land covers become mostly determined by the thermal properties, because of this under the suppressed precipitation scenario variations in surface temperatures are less pronounced in dense urban areas (Figure 14a). On the other hand, under the reference 2012 precipitation scenario (Figure 14b) surface temperature variations become more pronounced between land covers that have larger variations in moisture content. Relative difference between the two maps (Figure 14c) shows us that in urban areas soil surface temperatures tend to be around 10°C whereas natural surfaces have higher differences of up to 17°C. This is because developed surfaces stay relatively dry and achieved temperatures that were close to their potential maximum temperatures even during the reference 2012 year. On the other hand, the impact of suppressed precipitation on surface temperatures was relatively larger on natural surfaces that experienced the largest difference in average water content between the wet and the dry year. Because of this, the largest soil surface temperature changes under extreme dry conditions was detected in natural surfaces, where the potential increase in temperature caused by drying the surface was larger than for developed land covers.
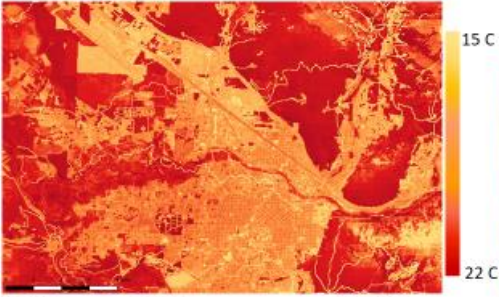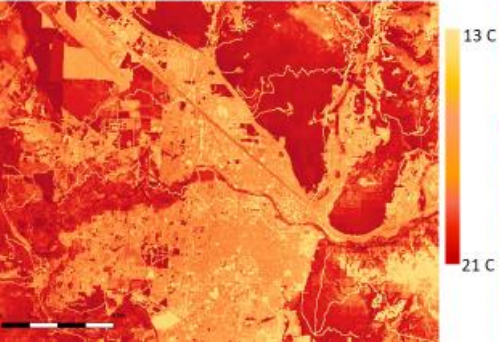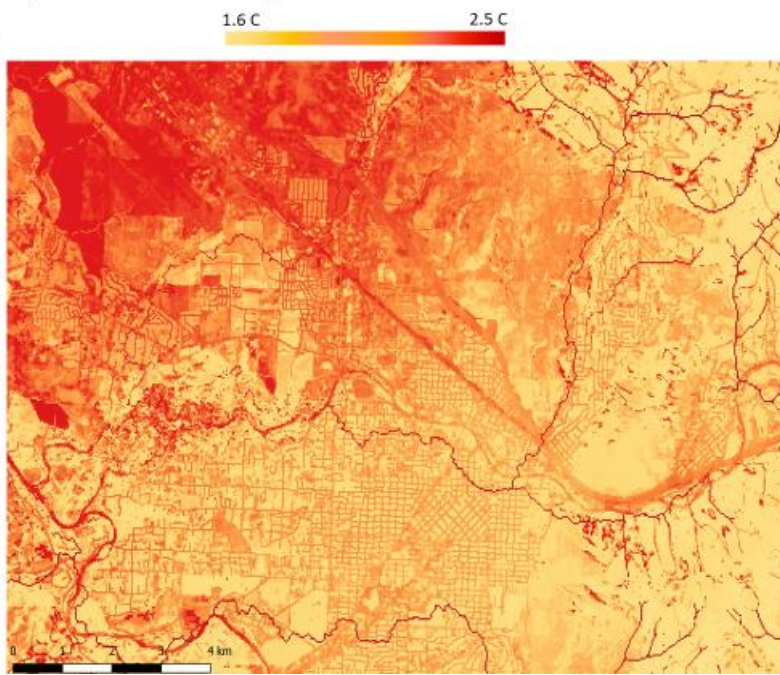
Figure 13. Differences in average summer surface temperatures over varying landcovers between 1998 (b) and 2012 (a). Highest difference in temperatures are natural areas or areas within urban landcovers that have moist soil conditions. Note the different temperature scales in (a) and (b).
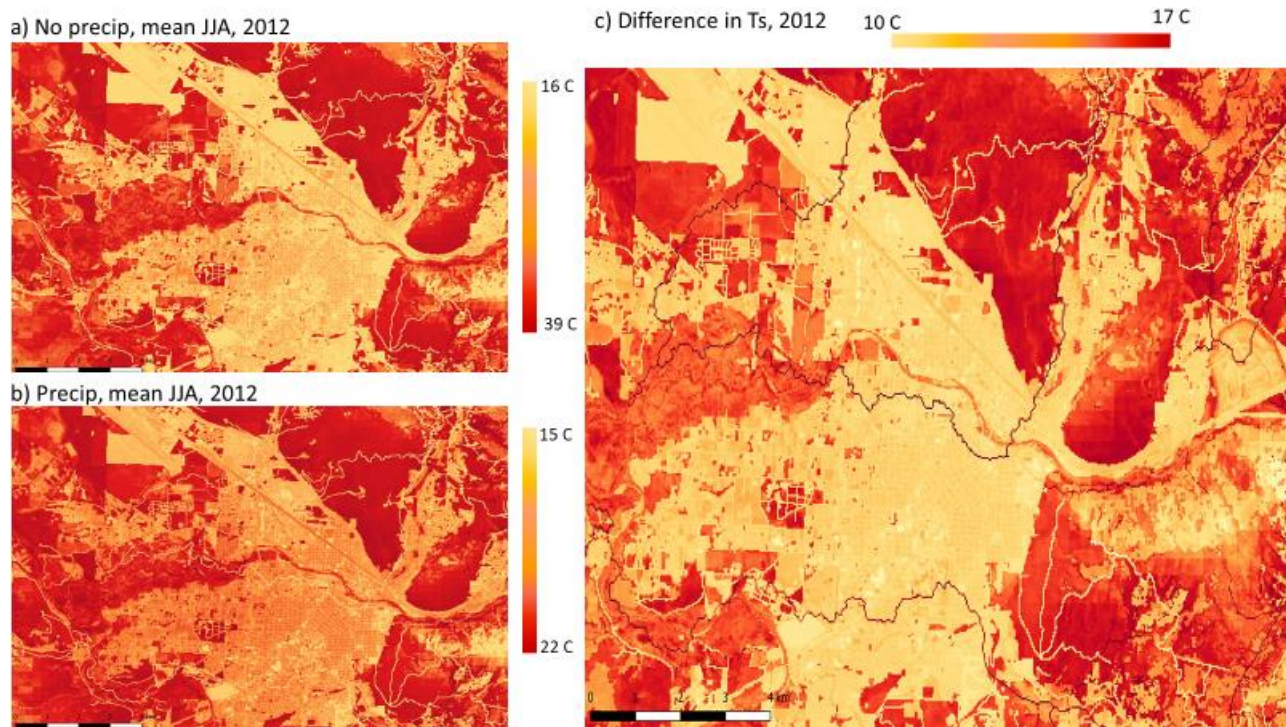
Figure 14. Differences in average surface temperatures over varying landcovers with 2012 precipitation conditions (a) and under the suppressed precipitation scenario (b). Temperatures can potentially increase 10°C-12°C in dense urban areas, however the largest relative surface temperature increase is in vegetated urban and suburban areas. Note the different temperature scales in (a) and (b).

2.4 Discussion

Despite the disagreements between Landsat LST and modeled surface temperatures, the range and main elements of the spatial temperature patterns are consistent across main urban and natural landcovers. The existing biases and differences in the statistical distribution of temperatures (Figure 9) is most likely the result from the fact that the model was not calibrated and the chosen parameterization may not be optimal. However, it is worth noting again that the modeled surface temperatures represent a 3-hourly average from 9AM to 12PM local time while the Landsat LST represents instantaneous radiative temperature at 11AM. Furthermore, Landsat retrieves land surface temperatures for a combination of emissivity temperatures from the canopies and the understory, whereas the model calculates integrated soil temperature over the first few inches of the soil.

Despite the lack of model calibration, the model simulates reasonably well the range of temperatures and explains 20% of the observed variance of the Landsat LST retrievals ($r^2= 0.2$, Figure 10c). Part of the bias is produced by an overestimation of high temperatures. Our simulations tend to overestimate the peak values of temperature ranges, most clearly around 20ºC, 25ºC and 35ºC, compared to the Landsat estimates. On the other hand, the spatial pattern of surface temperatures is reasonably well captured, providing some confidence that the spatial distribution of surface properties and their relative effect on the energy balance is generally correct.

The high surface heterogeneity of urban catchments and the associated complexity of hydrological and energy exchange processes require that environmental responses to varying precipitation inputs are analyzed at finer scales (Berne et al., 2004). Periodic precipitation events reduce soil surface temperature potentially maintaining it below hazardous levels and increasing urban thermal comfort during hot summer months (Mueller & Seneviratne, 2012; Ward et al., 2018). Surface temperatures variations due to changing precipitation regimes are more likely to increase due to a decrease in the frequency of summer precipitation events rather than a change in their magnitude, as illustrated in Figure 11.

LCLU impacts can significantly enhance or reduce the effects of hydroclimatic drivers on surface energy exchange processes (Rigden & Li, 2017; Zhao et al., 2014). Impervious surfaces reduce the amount of infiltration and water retention and therefore suppress latent heat fluxes, which leads to higher surface temperatures. Irrigated surfaces can enhance the dissipation of heat through latent heat losses (Figure 12b). Broadbent et al. (2018) show that the diurnal average air temperature was reduced by up to 2.3ºC at irrigated urban sites. The spatial distribution of available radiative energy is controlled by terrain aspect and by surface albedo and emissivity, which determine the fraction of incoming shortwave and longwave radiation that is absorbed. These properties provide the first order control on the accumulation of energy and hence on the enhancement of surface temperatures. Other properties, such as surface conductivity and heat

capacity or properties that enhance convective exchanges that determine the dissipation of available energy are secondary controls on the spatial distribution of surface temperatures.

Feedbacks between vegetation and the hydrologic cycle are well documented (e.g. Caylor et al., 2006; Florinsky & Kuryakova, 1996; Vivoni et al., 2010) and have been shown to modify water and energy balances and hence distribution of surface temperatures across varying spatial and temporal scales. Vegetation shades the ground, intercepts water and plays a key role in reapportioning between turbulent fluxes through latent heat losses associated with transpiration. Humes et al. (1994) showed that during the rainy season, the vegetation temperatures stayed within about 2°C of air temperature throughout the diurnal cycle, while the surface soil temperature warmed through the day in proportion to the surface soil moisture.

Within the study region, the percent canopy cover over developed areas is clearly lower than surrounding natural surfaces (Figure 4) reducing interception and transpiration water losses, but also reducing shading and aerodynamic resistance to turbulence and convection of latent and sensible heat. These factors partly determine the large difference in surface temperatures between urban and suburban or natural areas. The fractional vegetation cover over the densely populated urban area is on the order of 1%–20% (Figure 4), so the composite surface temperature is largely determined by the surface soil temperature, which is strongly influenced by the surface soil moisture status and hence precipitation.

2.5 Conclusions

In this study, we use an ecohydrological model to investigate the impact of two different precipitation scenarios on soil surface temperatures for different land covers in an urban setting. We show that the spatial variations in surface temperature differences between the two scenarios are determined by the heterogeneity of land surface properties and vegetation canopy cover. We also show that enhanced latent heat fluxes after precipitation events dissipate sufficient heat to reset the soil heat storage and significantly reduce soil temperatures. The cooling effect of precipitation is more efficient for relatively small but frequent precipitation events than for single large events.

In semiarid urban environments the combination of soil properties and the spatial heterogeneity of vegetation cover and evapotranspiration patterns interact to produce different partitions of the energy balance that determine the spatial and temporal dynamics of soil surface temperatures. Higher surface temperatures are expected in drier surfaces in which low latent heat exchanges are not sufficient to dissipate available energy, however these land uses are close to their maximum temperature and experienced relatively low increases in temperature under reduced precipitation scenarios. The largest relative increase in surface temperature occurred in vegetated regions with relatively high average soil moisture contents. It is in these land covers where the potential for temperature increases were the largest.

These findings have important practical implications for understanding land-atmosphere processes and can guide land planning to mitigate the impact of future drier conditions on surface temperatures.

References

Allen … Cobb. (2010). A global overview of drought and heat-induced tree mortality reveals emerging climate change risks for forests. *Forest Ecology and Management*, *259*(4), 660–684. https://doi.org/10.1016/j.foreco.2009.09.001

Anderegg, Berry, Smith, Sperry, Anderegg, & Field. (2012). The roles of hydraulic and carbon stress in a widespread climate-induced forest die-off. *Proceedings of the National Academy of Sciences of the United States of America*, *109*(1), 233–237. https://doi.org/10.1073/pnas.1107891109

Anderson, Hardy, Roach, & Witmer. (1976). *A Land Use And Land Cover Classification System For Use With Remote Sensor Data* (Vol. 964).

Anderson, Neale, Li, Norman, Kustas, Jayanthi, & Chavez. (2004). Upscaling ground observations of vegetation water content, canopy height, and leaf area index during SMEX02 using aircraft and Landsat imagery. *Remote Sensing of Environment*, *92*(4), 447–464. https://doi.org/10.1016/j.rse.2004.03.019

Barriopedro, Fischer, Luterbacher, Trigo, & García-Herrera. (2011). The hot summer of 2010: Redrawing the temperature record map of Europe. *Science*, *332*(6026), 220–224. https://doi.org/10.1126/science.1201224

Berg, Lintner, Findell, Malyshev, Loikith, & Gentine. (2014). Impact of soil moisture-atmosphere interactions on surface temperature distribution. *Journal of Climate*, *27*(21), 7976–7993. https://doi.org/10.1175/JCLI-D-13-00591.1

Berne, Delrieu, Creutin, & Obled. (2004). Temporal and spatial resolution of rainfall measurements required for urban hydrology. *Journal of Hydrology*, *299*(3–4), 166–179. https://doi.org/10.1016/S0022-1694(04)00363-4

Bertoldi, Albertson, Kustas, Li, & Anderson. (2007). On the opposing roles of air temperature and wind speed variability in flux estimation from remotely sensed land surface states. *Water Resources Research*, *43*(10), 1–13. https://doi.org/10.1029/2007WR005911

Boisier, De Noblet-Ducoudré, Pitman, Cruz, Delire, Van Den Hurk, Van Der Molen, Mller, & Voldoire. (2012). Attributing the impacts of land-cover changes in temperate regions on surface temperature and heat fluxes to specific causes: Results from the first LUCID set of simulations. *Journal of Geophysical Research Atmospheres*, *117*(12), 1–16. https://doi.org/10.1029/2011JD017106

Breshears … Meyer. (2005). Regional vegetation die-off in response to global-change-type drought. *Proceedings of the National Academy of Sciences of the United States of America*, *102*(42), 15144–15148. https://doi.org/10.1073/pnas.0505734102

Bright, Davin, O'Halloran, Pongratz, Zhao, & Cescatti. (2017). Local temperature response to land cover and management change driven by non-radiative processes. *Nature Climate Change*, *7*(4), 296–302. https://doi.org/10.1038/nclimate3250

Broadbent, Coutts, Tapper, & Demuzere. (2018). The cooling effect of irrigation on urban microclimate during heatwave conditions. *Urban Climate*, *23*(May), 309–329. https://doi.org/10.1016/j.uclim.2017.05.002

Budyko. (1969). The effect of solar radiation variations on the climate of the Earth. *Tellus*, *21*(5), 611–619. https://doi.org/10.3402/tellusa.v21i5.10109

Carlson, & Traci Arthur. (2000). The impact of land use - Land cover changes due to urbanization on surface microclimate and hydrology: A satellite perspective. *Global and Planetary Change*, *25*(1–2), 49–65. https://doi.org/10.1016/S0921-8181(00)00021-7

Caylor, D'Odorico, & Rodriguez-Iturbe. (2006). On the ecohydrology of structurally heterogeneous semiarid landscapes. *Water Resources Research*, *42*(7), 1–13. https://doi.org/10.1029/2005WR004683

Chen, & Dirmeyer. (2019). Global observed and modelled impacts of irrigation on surface temperature. *International Journal of Climatology*, *39*(5), 2587–2600. https://doi.org/10.1002/joc.5973

Cheruy, Dufresne, Aït Mesbah, Grandpeix, & Wang. (2017). Role of Soil Thermal Inertia in Surface Temperature and Soil Moisture-Temperature Feedback. *Journal of Advances in Modeling Earth Systems*, *9*(8), 2906–2919. https://doi.org/10.1002/2017MS001036

Comer … Teague. (2003). Ecological Systems of the United States: A Working Classification of U.S. Terrestrial Systems. *Nature Serve: Ecological Systems of the United States: A Working Classification of U.S. Terrestrial Systems*, *January*, 75. http://www.natureserve.org/publications/usEcologicalsystems.jsp

Cook, E. M., Hall, & Larson. (2012). Residential landscapes as social-ecological systems: A synthesis of multi-scalar interactions between people and their home environment. In *Urban Ecosystems* (Vol. 15, Issue 1). https://doi.org/10.1007/s11252-011-0197-0

Cook, M., Schott, Mandel, & Raqueno. (2014). Development of an operational calibration methodology for the Landsat thermal data archive and initial testing of the atmospheric compensation component of a land surface temperature (LST) product from the archive. *Remote Sensing*, *6*(11), 11244–11266. https://doi.org/10.3390/rs61111244

Coulston, Moisen, Wilson, Finco, Cohen, & Brewer. (2012). Modeling percent tree canopy cover: A pilot study. *Photogrammetric Engineering and Remote Sensing*, *78*(7), 715–727. https://doi.org/10.14358/PERS.78.7.715

D'Odorico, & Porporato. (2004). Preferential in soil moisture and climate dynamics. *Proceedings of the National Academy of Sciences of the United States of America*, *101*(24), 8848–8851. https://doi.org/10.1073/pnas.0401428101

Dai, Rasmussen, Liu, Ikeda, & Prein. (2020). A new mechanism for warm-season precipitation response to global warming based on convection-permitting simulations. *Climate Dynamics*, *55*(1–2), 343–368. https://doi.org/10.1007/s00382-017-3787-6

Daly, Taylor, & Gibson. (1997). The Prism approach to mapping precipitation and emperature. *10th AMS Conference on Applied Climatology*, *1*, 1–4.

Davenport, Grimmond, Oke, & Wieringa. (2000). Estimating the Roughness of Cities and Sheltered Country. *American Meterological Society*, *12*, 90–99.

Davis, Dobrowski, Higuera, Holden, Veblen, Rother, Parks, Sala, & Maneta. (2019). Wildfires and climate change push low-elevation forests across a critical climate threshold for tree regeneration. *Proceedings of the National Academy of Sciences of the United States of America*, *116*(13), 6193–6198. https://doi.org/10.1073/pnas.1815107116

Dentener … Morice. (2013). IPCC Climate Change 2013: The Physical Science Basis. Chapter 2:

Observations: Atmosphere and Surface. *Climate Change 2013 the Physical Science Basis: Working Group I Contribution to the Fifth Assessment Report of the Intergovernmental Panel on Climate Change*, *9781107057*, 159–254.

Devaraju, de Noblet-Ducoudré, Quesada, & Bala. (2018). Quantifying the relative importance of direct and indirect biophysical effects of deforestation on surface temperature and teleconnections. *Journal of Climate*, *31*(10), 3811–3829. https://doi.org/10.1175/JCLI-D-17-0563.1

Donohoe, Armour, Pendergrass, & Battisti. (2014). Shortwave and longwave radiative contributions to global warming under increasing CO2. *Proceedings of the National Academy of Sciences of the United States of America*, *111*(47), 16700–16705. https://doi.org/10.1073/pnas.1412190111

Duveiller, Hooker, & Cescatti. (2018). The mark of vegetation change on Earth's surface energy balance. *Nature Communications*, *9*(1). https://doi.org/10.1038/s41467-017-02810-8

Easterling, D.R., K.E. Knukel, J.R. Arnold, T. Knutson, A.N. LeGrande, L.R. Leung, R.S. Vose, D.E. Waliser. (2017). *Precipitation Change in the United States: Vol. I*. https://doi.org/10.7930/J0H993CC.U.S.

Fischer, & Knutti. (2015). Anthropogenic contribution to global occurrence of heavy-precipitation and high-temperature extremes. *Nature Climate Change*, *5*(6), 560–564. https://doi.org/10.1038/nclimate2617

Fischer, Rajczak, & Schär. (2012). Changes in European summer temperature variability revisited. *Geophysical Research Letters*, *39*(18), 1–8. https://doi.org/10.1029/2012GL052730

Fischer, Seneviratne, Vidale, Lüthi, & Schär. (2007). Soil moisture-atmosphere interactions during the 2003 European summer heat wave. *Journal of Climate*, *20*(20), 5081–5099. https://doi.org/10.1175/JCLI4288.1

Florinsky, & Kuryakova. (1996). Influence of topogrpahy on some vegetation cover properties. *Catena*, *27*, 123–141.

Francis, & Vavrus. (2012). Evidence linking Arctic amplification to extreme weather in mid-latitudes. *Geophysical Research Letters*, *39*(6), 1–6. https://doi.org/10.1029/2012GL051000

Garcia-Herrera, Díaz, Trigo, Luterbacher, & Fischer. (2010). A review of the european summer heat wave of 2003. *Critical Reviews in Environmental Science and Technology*, *40*(4), 267–306. https://doi.org/10.1080/10643380802238137

Gehne, Hamill, Kiladis, & Trenberth. (2016). Comparison of global precipitation estimates across a range of temporal and spatial scales. *Journal of Climate*, *29*(21), 7773–7795. https://doi.org/10.1175/JCLI-D-15-0618.1

Georgescu, Morefield, Bierwagen, & Weaver. (2014). Urban adaptation can roll back warming of emerging megapolitan regions. *Proceedings of the National Academy of Sciences of the United States of America*, *111*(8), 2909–2914. https://doi.org/10.1073/pnas.1322280111

Good, Ghent, Bulgin, & Remedios. (2017). A spatiotemporal analysis of the relationship between near-surface air temperature and satellite land surface temperatures using 17 years of data from the ATSR series. *Journal of Geophysical Research: Atmospheres*, *122*(17), 9185–9210. https://doi.org/10.1002/2017JD026880

Grimm, Faeth, Golubiewski, Redman, Wu, Bai, & Briggs. (2008). Global change and the ecology of cities.

Science, *319*(5864), 756–760. https://doi.org/10.1126/science.1150195

Gu … Wullschleger. (2006). Direct and indirect effects of atmospheric conditions and soil moisture on surface energy partitioning revealed by a prolonged drought at a temperate forest site. *Journal of Geophysical Research Atmospheres*, *111*(16), 1–13. https://doi.org/10.1029/2006JD007161

Haghighi;, & Kirchner. (2017). Near-surface turbulence as a missing link in modeling evapotranspiration-soil moisture relationships. *Water Resources Research*, *53*, 5320–5344. https://doi.org/10.1002/2016WR020111

Haghighi, E., & Or. (2013). Evaporation from porous surfaces into turbulent airflows: Coupling eddy characteristics with pore scale vapor diffusion. *Water Resources Research*, *49*(12), 8432–8442. https://doi.org/10.1002/2012WR013324

Haghighi, Erfan, Short Gianotti, Akbar, Salvucci, & Entekhabi. (2018). Soil and Atmospheric Controls on the Land Surface Energy Balance: A Generalized Framework for Distinguishing Moisture-Limited and Energy-Limited Evaporation Regimes. *Water Resources Research*, *54*(3), 1831–1851. https://doi.org/10.1002/2017WR021729

Hauser, Orth, & Seneviratne. (2017). Investigating soil moisture-climate interactions with prescribed soil moisture experiments: An assessment with the Community Earth System Model (version 1.2). *Geoscientific Model Development*, *10*(4), 1665–1677. https://doi.org/10.5194/gmd-10-1665-2017

Hegerl, F. W. Zwiers, Braconnot, Gillett, Luo, Orsini, Nicholls, Penner, & Stott. (2007). Understanding and Attributing Climate Change. In: Climate Change 2007: The Physical Science Basis. Contribution of Working Group I to the Fourth Assessment Report of the Intergovernmental Panel on Climate Change. *Cambridge University Press*, *80*(3–4), 213–238. https://www.ipcc.ch/pdf/assessment-report/ar4/wg1/ar4-wg1-chapter9.pdf

Holden … Landguth. (2019). A Topographically resolved wildfire danger and drought monitoring system for the conterminous United States. *Bulletin of the American Meteorological Society*, *100*(9), 1607–1613. https://doi.org/10.1175/BAMS-D-18-0178.1

Holden, Swanson, Luce, Jolly, Maneta, Oyler, Warren, Parsons, & Affleck. (2018). Decreasing fire season precipitation increased recent western US forest wildfire activity. *Proceedings of the National Academy of Sciences of the United States of America*, *115*(36), E8349–E8357. https://doi.org/10.1073/pnas.1802316115

Hsu, Lo, Guillod, Miralles, & Kumar. (2017). Relation between precipitation location and antecedent/subsequent soil moisture spatial patterns. *Journal of Geophysical Research*, *122*(12), 6319–6328. https://doi.org/10.1002/2016JD026042

Ingram. (2006). Detection and attribution of climate change, and understanding solar influence on climate. *Space Science Reviews*, *125*(1–4), 199–211. https://doi.org/10.1007/s11214-006-9057-2

Kitzberger, T.; Falk, D.A.; Westerling. (2017). Direct and indirect climate controls predict heterogeneous early-mid 21st century wildfire burned area across western and boreal North America. *PLOS One*, *12*(12), 429–438. https://doi.org/https://doi.org/10.1371/journal. pone.0188486

Kumar, Podzun, Hagemann, & Jacob. (2014). Impact of modified soil thermal characteristic on the simulated monsoon climate over south Asia. *Journal of Earth System Science*, *123*(1), 151–160. https://doi.org/10.1007/s12040-013-0381-0

Kuppel, Tetzlaff, Maneta, & Soulsby. (2018). What can we learn from multi-data calibration of a process-based ecohydrological model? *Environmental Modelling and Software*, *101*(January), 301–316. https://doi.org/10.1016/j.envsoft.2018.01.001

Lean. (1997). The sun's variable radiation and its relevance for earth. *Annual Review of Astronomy and Astrophysics*, *35*(1), 33–67. https://doi.org/10.1146/annurev.astro.35.1.33

Lean, & Rind. (1998). Climate forcing by changing solar radiation. *Journal of Climate*, *11*(12), 3069–3094. https://doi.org/10.1175/1520-0442(1998)011<3069:CFBCSR>2.0.CO;2

Liebethal, & Foken. (2007). Evaluation of six parameterization approaches for the ground heat flux. *Theoretical and Applied Climatology*, *88*(1–2), 43–56. https://doi.org/10.1007/s00704-005-0234-0

Luce,Abatzoglou. (2013). The Missing Mountain Water : Slower Westerlies Decrease Orographic Enhancement in the Pacific Northwest USA. *Science*, *342*(2013), 1360–1363.

Luyssaert … Dolman. (2014). Land management and land-cover change have impacts of similar magnitude on surface temperature. *Nature Climate Change*, *4*(5), 389–393. https://doi.org/10.1038/nclimate2196

Maneta, & Silverman. (2013). A spatially distributed model to simulate water, energy, and vegetation dynamics using information from regional climate models. *Earth Interactions*, *17*(11). https://doi.org/10.1175/2012EI000472.1

Meili … Fatichi. (2020). An urban ecohydrological model to quantify the effect of vegetation on urban climate and hydrology (UT&C v1.0). *Geoscientific Model Development*, *13*(1), 335–362. https://doi.org/10.5194/gmd-13-335-2020

Mesinger … Shi. (2006). North American regional reanalysis. *Bulletin of the American Meteorological Society*, *87*(3), 343–360. https://doi.org/10.1175/BAMS-87-3-343

Miralles, D. G., Van Den Berg, Teuling, & De Jeu. (2012). Soil moisture-temperature coupling: A multiscale observational analysis. *Geophysical Research Letters*, *39*(21), 2–7. https://doi.org/10.1029/2012GL053703

Miralles, Diego G., Teuling, Van Heerwaarden, & De Arellano. (2014). Mega-heatwave temperatures due to combined soil desiccation and atmospheric heat accumulation. *Nature Geoscience*, *7*(5), 345–349. https://doi.org/10.1038/ngeo2141

Missoula. (2019). *City of Missoula, Montana-City Limits Map*. City of Missoula, GIS Services. https://www.ci.missoula.mt.us/468/Available-Maps

Mueller, B., & Seneviratne. (2012). Hot days induced by precipitation deficits at the global scale. *Proceedings of the National Academy of Sciences of the United States of America*, *109*(31), 12398–12403. https://doi.org/10.1073/pnas.1204330109

Mueller, N. D., Butler, Mckinnon, Rhines, Tingley, Holbrook, & Huybers. (2016). Cooling of US Midwest summer temperature extremes from cropland intensification. *Nature Climate Change*, *6*(3), 317–322. https://doi.org/10.1038/nclimate2825

Neary, Daniel G.; Ryan, Kevin C.; DeBano. (2005). Wildland Fire in Ecosystems: Effect of Fire on Soil and Water. In *United States Department of Agriculture, USDA; Rocky Mountain Research Station* (Vol. 4).

Nemani, Pierce, & Running. (1993). Developing Satellite-derived Estimates of Surface Moisture Status. *J. Appl.Metero*, *32*, 548–557. https://doi.org/10.1175/1520-0450(1993)032<0548

Oke. (1982). The energetic basis of the urban heat island. *Quarterly Journal of the Royal Meteorological Society*, *108*(455), 1–24. https://doi.org/10.1002/qj.49710845502

Oleson, Bonan, Levis, & Vertenstein. (2004). Effects of land use change on North American climate: Impact of surface datasets and model biogeophysics. *Climate Dynamics*, *23*(2), 117–132. https://doi.org/10.1007/s00382-004-0426-9

Passerat De Silans, Bruckler, Thony, & Vauclin. (1989). Numerical modeling of coupled heat and water flows during drying in a stratified bare soil - Comparison with field observations. *Journal of Hydrology*, *105*(1–2), 109–138. https://doi.org/10.1016/0022-1694(89)90099-1

Perkins, Alexander, & Nairn. (2012). Increasing frequency, intensity and duration of observed global heatwaves and warm spells. *Geophysical Research Letters*, *39*(20), 1–5. https://doi.org/10.1029/2012GL053361

Puma, & Cook. (2010). Effects of irrigation on global climate during the 20th century. *Journal of Geophysical Research Atmospheres*, *115*(16), 1–15. https://doi.org/10.1029/2010JD014122

R, Marland, Betts, Chase, Eastman, Niles, & Running. (2002). The influence of land-use change and landscape dynamics on the climate system : relevance to climate-change policy beyond the radiative. *Environmental Sciences*, *360*(May), 1–15.

Rahmstorf, & Coumou. (2011). Increase of extreme events in a warming world. *Proceedings of the National Academy of Sciences of the United States of America*, *108*(44), 17905–17909. https://doi.org/10.1073/pnas.1101766108

Rigden, & Li. (2017). Attribution of surface temperature anomalies induced by land use and land cover changes. *Geophysical Research Letters*, *44*(13), 6814–6822. https://doi.org/10.1002/2017GL073811

Rother, & Veblen. (2016). Limited conifer regeneration following wildfires in dry ponderosa pine forests of the Colorado Front Range. *Ecosphere*, *7*(12). https://doi.org/10.1002/ecs2.1594

Samset, Stjern, Lund, Mohr, Sand, & Daloz. (2019). How Daily Temperature and Precipitation Distributions Evolve With Global Surface Temperature. *Earth's Future*, *7*(12), 1323–1336. https://doi.org/10.1029/2019EF001160

Schwingshackl, Hirschi, & Seneviratne. (2017). Quantifying spatiotemporal variations of soil moisture control on surface energy balance and near-surface air temperature. *Journal of Climate*, *30*(18), 7105–7124. https://doi.org/10.1175/JCLI-D-16-0727.1

Schwingshackl, Hirschi, & Seneviratne. (2018). Global Contributions of Incoming Radiation and Land Surface Conditions to Maximum Near-Surface Air Temperature Variability and Trend. *Geophysical Research Letters*, *45*(10), 5034–5044. https://doi.org/10.1029/2018GL077794

Shuai, Masek, Gao, & Schaaf. (2011). An algorithm for the retrieval of 30-m snow-free albedo from Landsat surface reflectance and MODIS BRDF. *Remote Sensing of Environment*, *115*(9), 2204–2216. https://doi.org/10.1016/j.rse.2011.04.019

Stone, & Allen. (2005). The end-to-end attribution problem: From emissions to impacts. *Climatic*

Change, *71*(3), 303–318. https://doi.org/10.1007/s10584-005-6778-2

Stroeve, Serreze, Holland, Kay, Malanik, & Barrett. (2012). The Arctic's rapidly shrinking sea ice cover: A research synthesis. *Climatic Change*, *110*(3–4), 1005–1027. https://doi.org/10.1007/s10584-011-0101-1

Templeton, Vivoni, Wang, & Schreiner-McGraw. (2018). Quantifying Water and Energy Fluxes Over Different Urban Land Covers in Phoenix, Arizona. *Journal of Geophysical Research: Atmospheres*, *123*(4), 2111–2128. https://doi.org/10.1002/2017JD027845

Thiery, Davin, Lawrence, Hirsch, Hauser, & Seneviratne. (2017). Present-day irrigation mitigates heat extremes. *Journal of Geophysical Research*, *122*(3), 1403–1422. https://doi.org/10.1002/2016JD025740

Thiery, Visser, Fischer, Hauser, Hirsch, Lawrence, Lejeune, Davin, & Seneviratne. (2020). Warming of hot extremes alleviated by expanding irrigation. *Nature Communications*, *11*(1), 1–7. https://doi.org/10.1038/s41467-019-14075-4

Trenberth, & Shea. (2005). Relationships between precipitation and surface temperature. *Geophysical Research Letters*, *32*(14), 1–4. https://doi.org/10.1029/2005GL022760

U.S. Census Bureau. (2018). *U.S. Census Bureau: Quick Facts*. U.S. Census Bureau. https://www.census.gov/quickfacts/fact/table/missoulacitymontana,US/RHI825218

United Nations. (2018). World Urbanization Prospects. In *Demographic Research* (Vol. 12).

USGCRP … Tavoni. (2018). Impacts, Risks, and Adaptation in the United States: Fourth National Climate Assessment. In *U.S. Global Change Research Program: Vol. II*. https://doi.org/10.7930/J0J964J6

USGS. (2018). *U . S . Landsat Analysis Ready Data* (Issue August).

Vivoni, Rodríguez, & Watts. (2010). On the spatiotemporal variability of soil moisture and evapotranspiration in a mountainous basin within the North American monsoon region. *Water Resources Research*, *46*(2), 1–18. https://doi.org/10.1029/2009WR008240

Ward, Tan, Gabey, Kotthaus, & Grimmond. (2018). Impact of temporal resolution of precipitation forcing data on modelled urban-atmosphere exchanges and surface conditions. *International Journal of Climatology*, *38*(2), 649–662. https://doi.org/10.1002/joc.5200

Westerling. (2016). Increasing western US forest wildfire activity: Sensitivity to changes in the timing of spring. *Philosophical Transactions of the Royal Society B: Biological Sciences*, *371*(1696). https://doi.org/10.1098/rstb.2015.0178

Whan, Zscheischler, Orth, Shongwe, Rahimi, Asare, & Seneviratne. (2015). Impact of soil moisture on extreme maximum temperatures in Europe. *Weather and Climate Extremes*, *9*, 57–67. https://doi.org/10.1016/j.wace.2015.05.001

Wild. (2016). Decadal changes in radiative fluxes at land and ocean surfaces and their relevance for global warming. *Wiley Interdisciplinary Reviews: Climate Change*, *7*(1), 91–107. https://doi.org/10.1002/wcc.372

Wu, Jenerette, Buyantuyev, & Redman. (2011). Quantifying spatiotemporal patterns of urbanization: The case of the two fastest growing metropolitan regions in the United States. *Ecological Complexity*. https://doi.org/10.1016/j.ecocom.2010.03.002

Zhao, Lee, Smith, & Oleson. (2014). Strong contributions of local background climate to urban heat islands. *Nature*, *511*(7508), 216–219. https://doi.org/10.1038/nature13462

Appendices

Appendix A: Surface energy balance components and parameter definitions
Description of symbols and units are presented in Table 1.

SEB component and parameter definitions:

$$a = \frac{0.2 * LAI * H_t}{l_m} \tag{A1}$$

$$\beta = \frac{1}{4}[1 - cos(\frac{\theta * \pi}{\theta_{fc}})]^2 \tag{A2}$$

$$\tag{A3}$$

$$C_s = (1 - n) * c_p + \theta * c_w * \rho_w + (n - \theta) * c_a * \rho_a$$

$$d_s = \sqrt{\frac{K_s}{2 * C_s * \omega}} \tag{A4}$$

$$e_a = e_s^* * R_H \tag{A5}$$

$$e_s^* = (611 * e^{\frac{17.3Ts}{Ts+237.3}}) \tag{A6}$$

$$G = (\frac{d_s * C_s}{dt} - \frac{G_d}{(\omega * dt)})T_s + (G_d - \frac{G_d * d_s * \omega * dt}{d_o}) T_d \tag{A7}$$

$$G_d = \sqrt{\frac{K_s * C_s * \omega}{2}} \tag{A8}$$

$$H = \frac{\rho_a * c_a}{r_a}(T_a + 273.2 - T_s + 273.2) \tag{A9}$$

$$H_r = \rho_w * c_w * P(T_a + 273.2 - T_m + 273.2) \tag{A10}$$

$$K_s = (1 - n) * K_p + \theta * K_w + (n - \theta) * K_a \tag{A11}$$

$$LE = \frac{\rho_a * c_a (e_a(T_a) - e_s^*(T_s) * R_H)}{\gamma(r_a + r_s)} \tag{A12}$$

$$l_m = \sqrt{\frac{4 * 0.05 * H_t}{\pi * LAI}} \tag{A13}$$

$$r_a = \frac{(\ln \frac{z_a - z_d}{z_o})^2}{\text{к} * u_a} \tag{A14}$$

$$r_s = 3.8113e4 * e^{-13.515 * S} \tag{A15}$$

$$r_{exp} = \frac{\ln(\frac{z_a - z_{do}}{z_{oo}})}{a * \text{к}^2 * u_a * (H_t - z_{do})} * H_t * \{ exp(a) * exp(\frac{-a * z_t}{H_t}) - exp(a) * exp(\frac{-a(z_{do} + z_{oo})}{H_t}) \} \tag{A16}$$

$$R_H = \beta * e_s^*(T_s) + (1 - \beta) * e_a(T_a) \tag{A17}$$

$$R_n = S_{down}(1 - \alpha_s)exp(-\chi * LAI) + \xi_s(1 - \xi_c)L_{down} + \xi_s\xi_c\sigma(T_c + 273.2)^4 - \xi_s\sigma(T_s + 273.2)^4 \tag{A18}$$

$$S = \frac{\theta - \theta_r}{\theta_{fc} - \theta_r} \tag{A19}$$

$$T_d = \frac{-d_s}{d_o} * (T_d^{t-1} - T_s^{t-1}) * \omega * dt + T_d^{t-1} \tag{A20}$$

$$\omega = \frac{2\pi}{Day} \tag{A21}$$

$$\theta_{fc} = (\frac{\psi_{ae}}{3.36})^{\frac{1}{\lambda}} * (\theta - \theta_r) + \theta_r \tag{A22}$$

$$\gamma = \frac{\rho_a * c_a}{0.611 * \lambda_v} \tag{A23}$$

$$* z_a = H_t + 2m \tag{A24}$$

$$z_d = 0.7 * r_r \tag{A25}$$

$$z_o = 0.1 * r_r \tag{A26}$$

$$z_{do} = H_t^{0.98} * 0.707946 \tag{A27}$$

$$z_{oo} = H_t^{1.19} * 0.057544 \tag{A28}$$

$$z_t = z_{do} + z_{oo} \tag{A29}$$

$* z_a$ for bare soil scenarios is elevation at which wind speed is measured at roughness of surface (r_r) +2m, for canopies it is height of vegetation (H_t)+ 2m.

Appendix B: Linearization of T_s

 All SEB components are non-linear functions of T_s. Latent heat flux, for example, is a function of saturated vapor pressure (e_s*). Since e_s* and outgoing radiation emitted by surface ($\xi_s \, \sigma \, (T_s + 273.2)^4$) are nonlinear, and we want to swap T_s with temperature of air (T_a), we linearize using a Taylor Series Expansion about a known value of T_a with $T_s = T_a + dT = T_a + (T_s-T_a)$:

$$f(T_a + dT) = f(T_a) + f'dT \tag{B1}$$

Linearizing outgoing radiation and e_s*:

$$\xi_s\sigma(T_s + 273.2)^4 \sim \xi_s\sigma(T_a + 273.2)^4 + 4\xi_s\sigma(T_a + 273.2)^3(T_s - T_a) \tag{B2}$$

Where ξ_s is emissivity of surface, σ is Stefan-Boltzman constant (W m^{-2} K^{-4}) and $\lambda_o = 4\xi_s\sigma(T_a + 273.2)^3$

$$e_s^* \sim e_a^* + \frac{de_s^*}{dT}|_{Ta} * (T_s - T_a) \sim e_a^* + \Delta_{Ta}(T_s - T_a) \tag{B3}$$

Where $\Delta_{Ta} = \frac{de_s^*}{dT}|_{Ta} = \frac{2508332.19 * e^{\frac{17.3Ta}{237.3+Ta}}}{(Ta+237.3)^2}$

Linearized versions of e_s^* in the latent heat term and net radiation terms in the energy balance equation:

$$LE^* = \frac{\rho_a \, c_a \, (e_a - (e_a^* + \Delta_{Ta}(T_s - T_a) * R_H))}{\gamma(r_a + r_s)} \tag{B4}$$

Where LE^* is linearized latent heat, ρ_a is air density (kg m^{-3}) , c_a is specific heat capacity of air (J Kg^{-1} ^{o}C^{-1}), e_a is vapor pressure of air (Pa), R$_H$ is relative humidity, γ is psychrometric constant (Pa ^{o}C^{-1}), r_a is aerodynamic resistance of surface (s m^{-1}) and r_s is soil resistance to evaporation(s m^{-1}) .

$$R_n^* = S_{down}(1 - \alpha_s)exp(-\chi * LAI) + \xi_s(1 - \xi_c)L_{down} + \xi_s\xi_c\sigma(T_c + 273.2)^4 - \xi_s\sigma(T_a + 273.2)^4 \\ - 4\xi_s\sigma(T_a + 273.2)^3(T_s - T_a) \tag{B5}$$

Where R$_n^*$ is linearized net radiation, S$_{down}$ is incoming shortwave radiation, L$_{down}$ is incoming longwave radiation, α_s is albedo, χ is exponential attenuation coefficient for vegetation following Beer's law, ξ_c is emissivity of canopy, LAI is leaf area index and T$_c$ is temperature of the canopy.

 Using the linearized surface energy balance equation:

$$R_n^* = -LE^* - H - G - H_r \tag{B6}$$

And then solving for T_s at time=t, the linearized T_s equation is:

$$T_s{}^t = \frac{\left(H_r + Rn^* + \left(\lambda_o + \Gamma_a * \Delta_{Ta} + \frac{r_o}{r_a + r_{exp}}\right) * T_a + \Gamma_a * e_a{}^* * (R_H - 1) + \left(\frac{d_s * C_s}{dt} - \frac{G_d}{(\omega * dt)}\right) * T_s{}^{t-1} + \left(G_d - \frac{G_d * d_s * \omega * dt}{d_o}\right) * T_d{}^{t-1}\right)}{\lambda_o + \Gamma_a * \Delta + \frac{r_o}{r_a + r_{exp}} + \frac{d_s * C_s}{dt} - \frac{G_d}{(\omega * dt)} + G_d - \frac{G_d * d_s * \omega * dt}{d_o}} \quad \text{(B7)}$$

Where $\lambda_o = 4\,\xi_s\,\sigma\,(T_a + 273.2)^3$, $\Gamma_a = \frac{r_o * \beta}{\gamma(r_a + r_s)}$, $r_o = \rho_a\,c_a$, $\Delta_{Ta} = \frac{de_s^*}{dT}\big|_{Ta}$

<u>Domain (Eq. B7):</u> domain of function: soil moisture 0<ℝ<1; temperature (-∞, ∞) radiation (0,∞)

<u>Initial conditions:</u>

Soil surface temperature (T_s)

Soil temperature at damping depth (T_d)

<u>Boundary conditions:</u>

1. Air temperature

2. Relative humidity

3. Incoming shortwave

4. Incoming longwave

5. Precipitation

6. Windspeed

<u>Soil, vegetation and surface parameters: Table 1</u>

Appendix C: In situ instrumentation
Site 1: Clapp Station, Irrigated surface
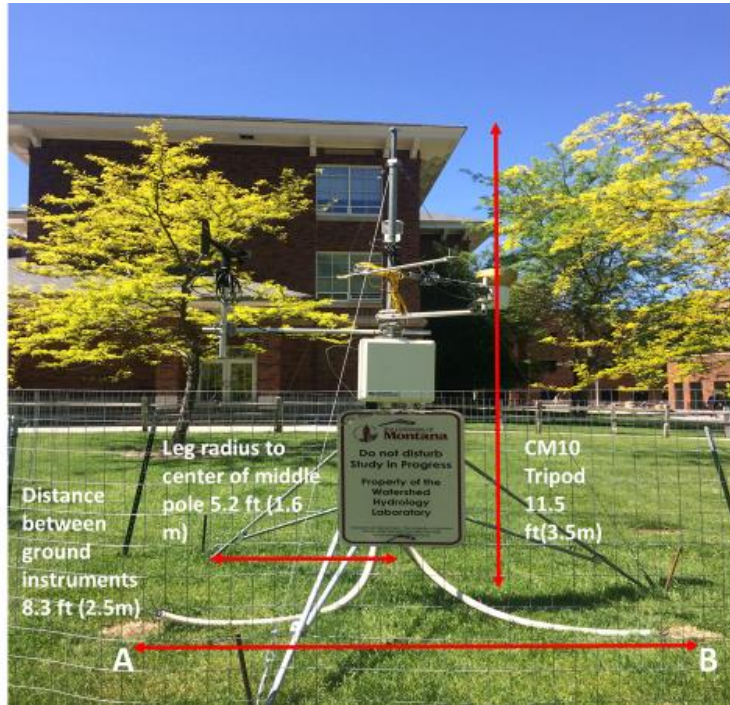
Figure C1. Site 1 instrumentation outside of CLAPP Building at University of Montana. A CM10 tripod with relative humidity and air temperature, net radiometer, pyranometer, wind speed, rain gauge and barometric pressure instruments and ground instrumentation with soil temperature, soil volumetric water content probes and ground heat flux plates.

Site 1 is located on the grounds outside of CLAPP Building at the University of Montana, Missoula campus. The total footprint of the CM10 tripod on which meteorology instruments are mounted is about 8.04 square meters with its height of 3.5 meters. Instruments mounted on the tripod and number of sensors (in brackets) are as follows:

Table C1. Instrumentation and number of sensors (in brackets) at Site1, Figure C1.

Instrument/model	Manufacturer	Variable measured
Net radiometer/NR-LITE 2 (1)	Kipp & Zonen	Spectral range for solar and far infrared from 0.2 to 100 micrometers
Pyranometer/CS300 (1)	Campbell Scientific	Spectral range 0.36 to 1.1 micrometers
Temperature and relative humidity sensor/ HMP50 (1)	Vaisala	Air temperature and relative humidity
Wind monitor/05103-45-L (1)	Young	Wind speed and direction

Rain gauge/ TE525MM (1)	Texas Electronics	Precipitation; metric tipping bucket with 0.1mm per tip resolution

Ground instruments were placed in two holes each about ~25 cm deep with top 10 cm of grass and grass roots, next 15 cm dark soil overlaying on a bed of gravel and cobbles. Total of 6 soil moisture and temperature probes and 2 ground heat flux plates were placed in the ground at two opposite sides of the tripod CM10 (positions A and B in Figure C1). The instruments and their quantities (in brackets) are as follows:

Table C2. Instrumentation and number of sensors (in brackets) at Site1 positions A and B under the ground, Figure C1.

Instrument/model	Manufacturer	Variable measured
Soil heat flux plate/ HFPSC-1 (2)	Hukseflux	Ground heat flux
Soil water content and temperature sensor/ECH2o 5TE (6)	Decagon Devices	Soil temperature and soil volumetric water content

Table C3. Depths of ground instruments installed at positions A and B (Figure C1), Site1.

Instrument	Depth (cm)
ECH2o 5TE probe (soil moisture probe 1) - position A	22.86
ECH2o 5TE probe (soil moisture probe 2) - position A	8.89
ECH2o 5TE probe (soil moisture probe 3) - position A	17.78
ECH2o 5TE probe (soil moisture probe 4) - position B	7.8
ECH2o 5TE probe (soil moisture probe 5) - position B	16.51
ECH2o 5TE probe (soil moisture probe 6) - position B	24.13
Hukseflux HFPSC-1 (ground heat flux plate 1) - position A	13.97
Hukseflux HFPSC-1 (ground heat flux plate 2) - position B	11.43

Figure C2. Site 2 instrumentation in the parking lot behind Skaggs Building at University of Montana. A trench was dug extending from the island with trees to under the asphalt and concrete lot. A soil moisture probe and one ground heat flux plate were installed at this location under the parking lot. The thickness of parking lot asphalt surface at this location is ~ 4.5 inches (11.43 cm).

Site 2 is located at the parking lot behind Skaggs Building at the University of Montana, Missoula campus. Ground instruments were placed at three different depths under the asphalt parking lot surface. The total thickness of asphalt was measured to be approximately 4.5 inches (11.43 cm) at this location. There is an insulating material layer below the asphalt surface followed by dry finely grained sand, silt with trace amounts of clay and big gravel and cobble aggregates that dominate the ground under the parking lot surface. Site 2 is characterized by a concrete curb about 11 inches (27.9 cm) deep and a concrete ledge next to it about 4.5 inches (11.43 cm) deep and about 15 inches (38.1 cm) long (Figure 11). Total of 3 soil moisture and temperature probes and 1 ground heat flux plate were placed in the ground at varying depths and

lengths (length measured from curb). The instruments and their quantities (in brackets) are as follows:

Table C4. Instrumentation and number of sensors (in brackets) at Site2 under the parking lot, Figure C2.

Instrument/model	Manufacturer	Variable measured
Net radiometer/NR-LITE 2 (1)	Kipp & Zonen	Spectral range for solar and far infrared from 0.2 to 100 micrometers
Soil heat flux plate/ HFPSC-1 (1)	Hukseflux	Ground heat flux
Soil water content and temperature sensor/ECH2o 5TE (1)	Decagon Devices	Soil temperature and soil volumetric water content

Table C5. Depths of ground instruments installed in the parking lot (Figure C2), Site2.

Instrument	Depth (cm)	Distance from curb (cm)
ECH2o 5TE probe	18.79	33.02 (positioned close to curb side on concrete surface)
Hukseflux HFPSC-1	18.79	33.02 (positioned next to soil moisture probe 3)

Appendix D: Verification of linearized T_s

Verification of the linear surface energy balance model:

We illustrate that in the case of both a non-vegetated and a vegetated surface the linear version of the model that is based on Monin-Obukhov similarity theory for turbulent exchanges, is a sufficiently good approximation of processes that determine surface temperatures (Fig E1). The linear model was verified against Ech2o, a fully distributed, physically based, ecohydrological model that has been previously calibrated and validated (Maneta & Silverman, 2013).

a) Bare soil **b) With vegetation**
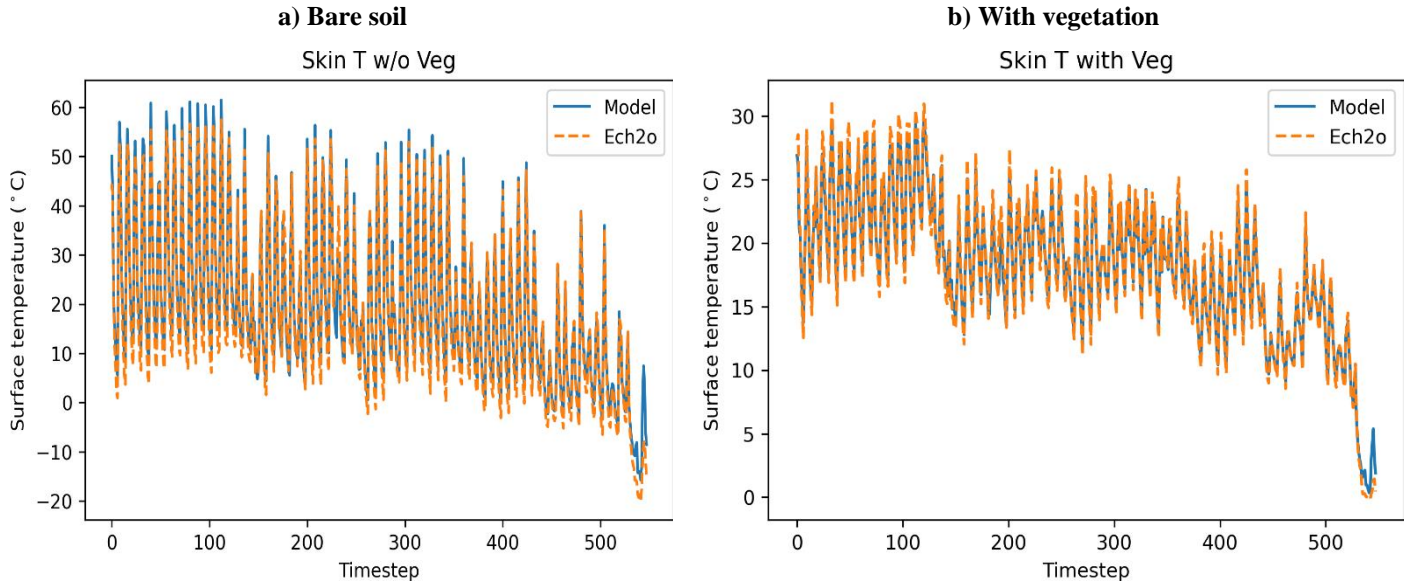
Figure D1. Linearized energy balance model (solid blue) for both bare soil (a) and with vegetation (b) shows close match with ecohydrological model, Ech2o (dashed orange).

Appendix E: Analytical solutions
Using analytical solutions to explain numerical elasticities: Attribution of differences in
elasticities to parameters of SEB components becomes apparent using analytical solutions to
partial derivatives of surface temperatures with respect to soil moisture, air temperatures and
radiative forcing.

$$\varepsilon_\theta$$

a) Bare soil

Soil moisture elasticity (Sensitivity of Ts to change in SM without Veg)

b) With vegetation
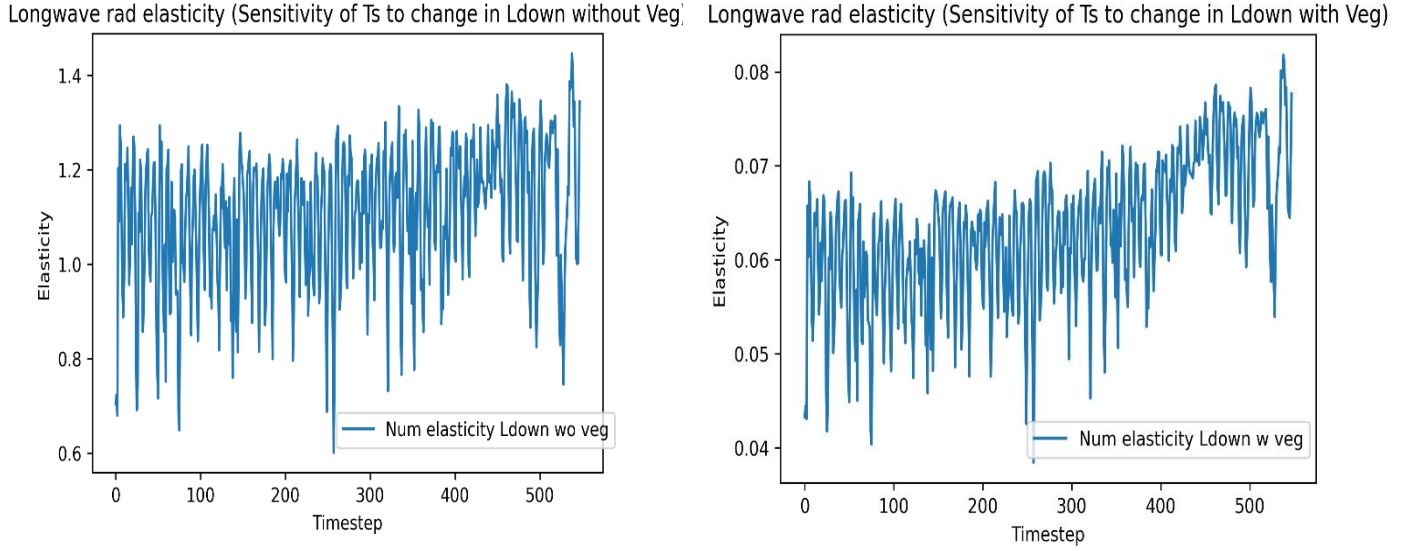
Soil moisture elasticity (Sensitivity of Ts to change in SM with Veg)
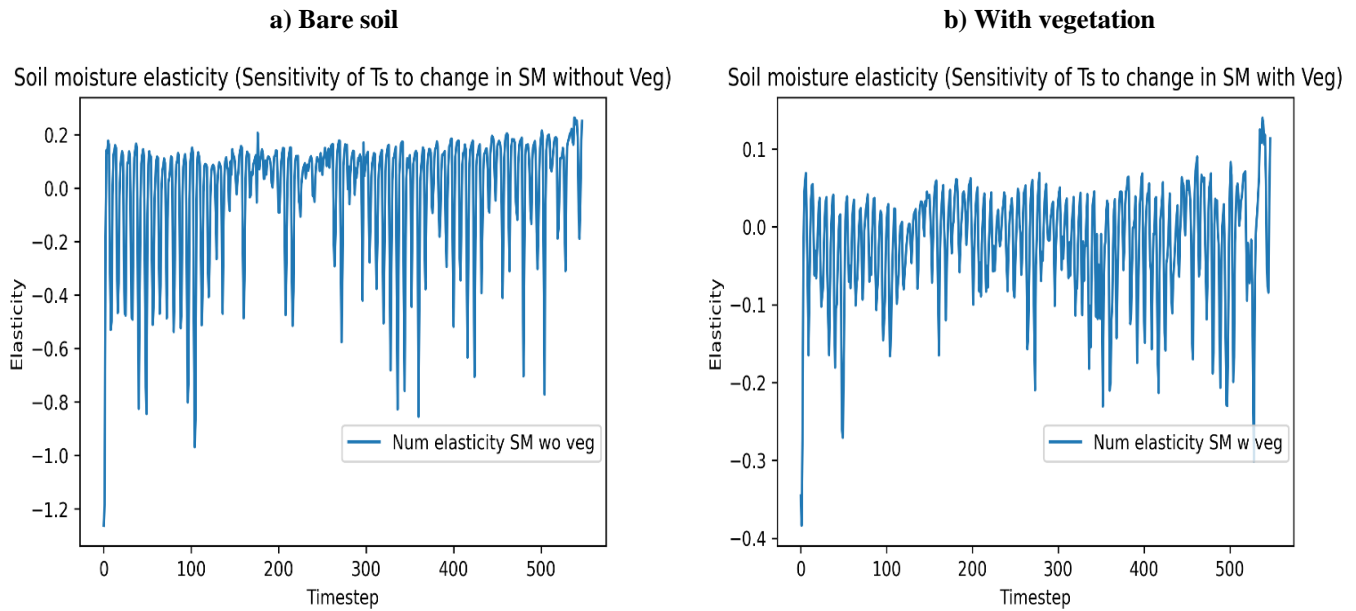
Figure E1. Numerical elasticities with respect to soil moisture for a bare soil (a) and a vegetated (b) landcover.

$$\frac{\partial T_s}{\partial \theta} = \frac{\Gamma_a{}'[\,(R_H-1)e_a{}^*\,\{\lambda_o +\frac{r_o}{r_a+r_{exp}}+Z\} + \Delta_{Ta}\{T_aZ-R_n{}^*-N\}\,]}{(\lambda_o+\Gamma_a\Delta_{Ta}+\frac{r_o}{r_a+r_{exp}}+Z)^2}\quad (f1)$$

$$+\frac{\Gamma_a\,[-(R_H-1)e_a{}^*Z' + \Delta_{Ta}\{-T_aZ'+N'\}]}{(\lambda_o + \Gamma_a\Delta_{Ta} + \frac{r_o}{r_a+r_{exp}} + Z)^2}\quad (f2)$$

$$+\frac{N'\,[\lambda_o + \frac{r_o}{r_a+r_{exp}} + Z]}{(\lambda_o + \Gamma_a\Delta_{Ta} + \frac{r_o}{r_a+r_{exp}} + Z)^2}\quad (f3)$$

$$-\frac{Z'\,[R_n{}^* + T_a\{\lambda_o + \frac{r_o}{r_a+r_{exp}}\} + N]}{(\lambda_o + \Gamma_a\Delta_{Ta} + \frac{r_o}{r_a+r_{exp}} + Z)^2}\quad (f4)$$

(E1)

Equation E1: analytical solution to numerical soil moisture elasticity. Where

$$Z = \frac{d_s*C_s}{dt} - \frac{G_d}{(\omega*dt)} + G_d - \frac{G_d*d_s*\omega*dt}{d_o}, N = \left(\frac{d_s*C_s}{dt} - \frac{G_d}{(\omega*dt)}\right)*T_s{}^{t-1} + \left(G_d - \frac{G_d*d_s*\omega*dt}{d_o}\right)*T_d{}^{t-1}$$

and Γ_a' Z' and N' are derivatives of those terms.
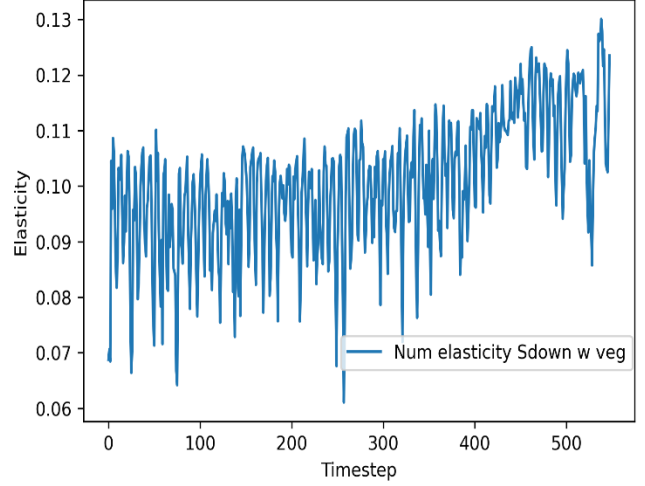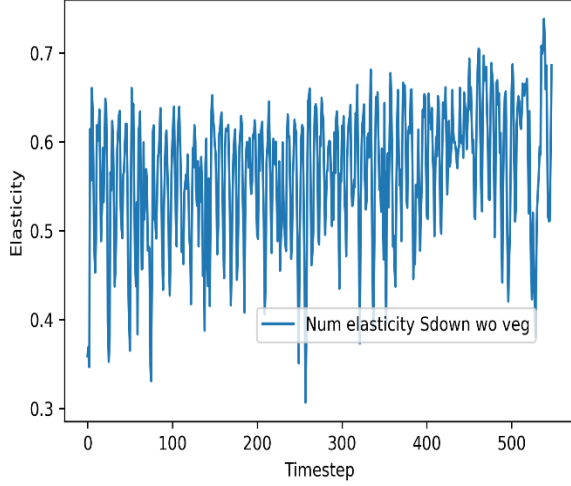
$$\mathcal{E}_{Ta}$$

a) Bare soil

b) With vegetation
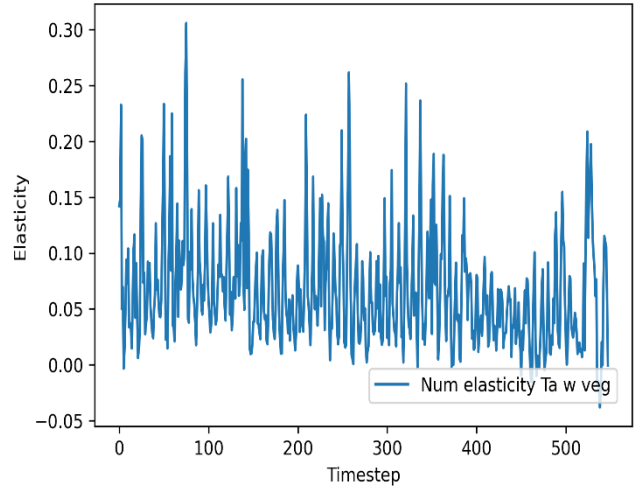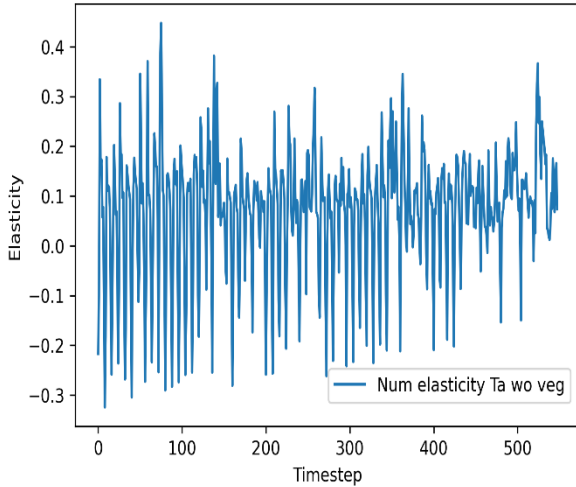
Figure E2. Numerical elasticities with respect to air temperature for a bare soil (a) and a vegetated (b) landcover.

$$\frac{\partial T_s}{\partial T_a} = \frac{\lambda_o[\lambda_o + R_n^{*\prime} + 2\Gamma_a\Delta_{Ta} + 2\frac{r_o}{r_a + r_{exp}} + (R_H - 1)\,(\Gamma_a{}^\prime e_a^{*} + \Gamma_a e_a^{*\prime}) + N^\prime + Z - Z^\prime T_a]}{(\lambda_o + \Gamma_a\Delta_{Ta} + \frac{r_o}{r_a + r_{exp}} + Z)^2} \quad (f1)$$

$$+ \frac{\Delta_{Ta}[\,\Gamma_a\,\{\,R_n^{*\prime} + \Gamma_a\Delta_{Ta} + 2\frac{r_o}{r_a + r_{exp}} + (R_H - 1)Xe_a^{*\prime} + N^\prime + Z - Z^\prime T_a\} + \Gamma_a{}^\prime\,\{-R_n^{*} - N + ZT_a\}]}{(\lambda_o + \Gamma_a\Delta_{Ta} + \frac{r_o}{r_a + r_{exp}} + Z)^2} \quad (f2)$$

$$+ \frac{\frac{r_o}{r_a + r_{exp}}\,[R_n^{*\prime} + \frac{r_o}{r_a + r_{exp}} + (R_H - 1)\,(\Gamma_a{}^\prime e_a^{*} + \Gamma_a e_a^{*\prime}) + N^\prime + Z - Z^\prime T_a\,]}{(\lambda_o + \Gamma_a\Delta_{Ta} + \frac{r_o}{r_a + r_{exp}} + Z)^2} \quad (f3)$$

$$+ \frac{Z\,[\,R_n^{*\prime} + (R_H - 1)\,(\Gamma_a{}^\prime e_a^{*} + \Gamma_a e_a^{*\prime}) + N^\prime\,]}{(\lambda_o + \Gamma_a\Delta_{Ta} + \frac{r_o}{r_a + r_{exp}} + Z)^2} \quad (f4)$$

$$+ \frac{Z^\prime[-(R_H - 1)\Gamma_a e_a^{*} - Rn^{*} - N]}{(\lambda_o + \Gamma_a\Delta_{Ta} + \frac{r_o}{r_a + r_{exp}} + Z)^2} \quad (f5)$$

$$+ \frac{\frac{r_o{}^\prime}{r_a + r_{exp}}\,[-(R_H - 1)\Gamma_a e_a^{*} - Rn^{*} - N]}{(\lambda_o + \Gamma_a\Delta_{Ta} + \frac{r_o}{r_a + r_{exp}} + Z)^2} \quad (f6)$$

$$+ \frac{\Delta_{Ta}{}^\prime\,[\,\Gamma_a\,\{-(R_H - 1)\Gamma_a e_a^{*} - R_n^{*} - N\}\,]}{(\lambda_o + \Gamma_a\Delta_{Ta} + \frac{r_o}{r_a + r_{exp}} + Z)^2} \quad (f7)$$

$$+ \frac{\lambda_o{}^\prime[-(R_H - 1)\Gamma_a e_a^{*} - R_n^{*} - N]}{(\lambda_o + \Gamma_a\Delta_{Ta} + \frac{r_o}{r_a + r_{exp}} + Z)^2} \quad (f8)$$

Equation E2: analytical solution to numerical air temperature elasticity where the apostrophes on top of variables represent derivatives of those terms.

$$\mathcal{E}_{Ldown}$$

a) Bare soil   **b) With vegetation**

Figure E3. Numerical elasticities with respect to downwelling longwave radiation for a bare soil (a) and a vegetated (b) landcover.

$$\frac{\partial T_s}{\partial L_{down}} = \frac{\xi_s(1 - \xi_c)}{\lambda_o + \Gamma_a \Delta_{Ta} + \dfrac{r_o}{r_a + r_{exp}} + Z} \tag{E3}$$
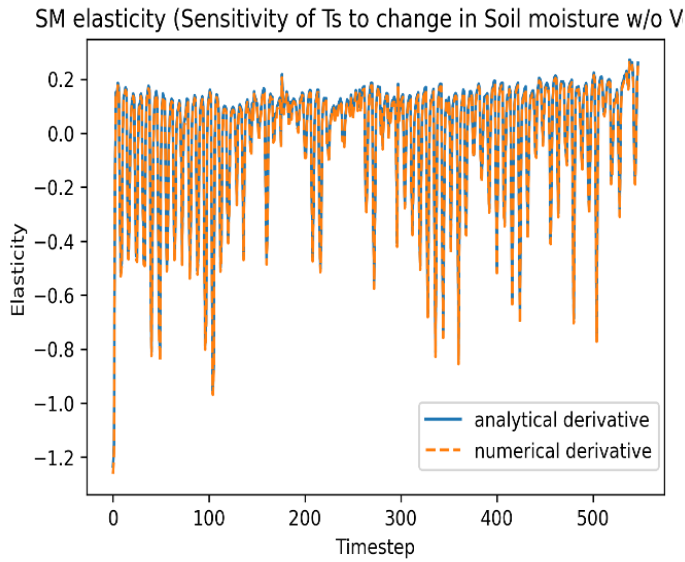
Equation E3: analytical solution to numerical downwelling longwave radiation elasticity.

$$\varepsilon_{Sdown}$$

a) Bare soil   **b) With vegetation**

Figure E4. Numerical elasticities with respect to incoming shortwave radiation for a bare soil (a) and a vegetated (b) landcover.

$$\frac{\partial T_s}{\partial S_{down}} = \frac{(1-\alpha_s)exp(-\chi * LAI)}{\lambda_o + \Gamma_a\Delta_{Ta} + \dfrac{r_o}{r_a + r_{exp}} + Z} \tag{E4}$$

Equation E4: analytical solution to numerical incoming shortwave radiation elasticity.

Appendix F: Verification of numerical and analytical derivatives

Verification of numerical and analytical derivatives of surface temperatures to soil moisture, air temperature and radiation for a bare soil and a vegetated surface.

a) Bare soil   **b) With vegetation**

SM elasticity (Sensitivity of Ts to change in Soil moisture w/o V)

SM elasticity (Sensitivity of Ts to change in Soil moist w Veg)

Ta elasticity (Sensitivity of Ts to change in Ta w/o Veg)

Ta elasticity (Sensitivity of Ts to change in Air Temp w Veg)
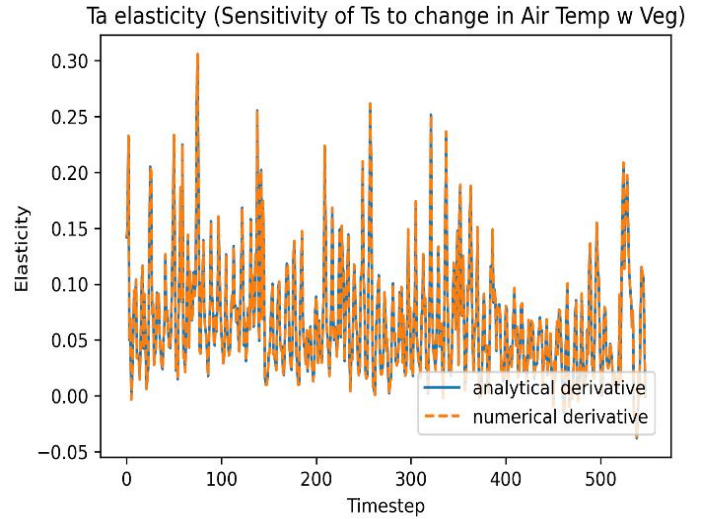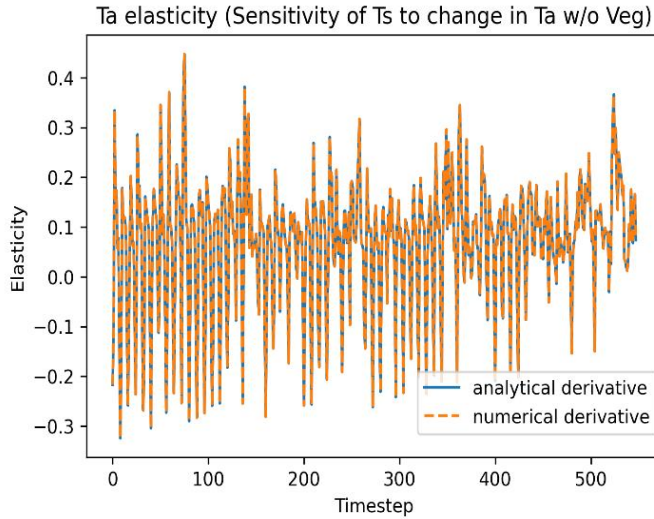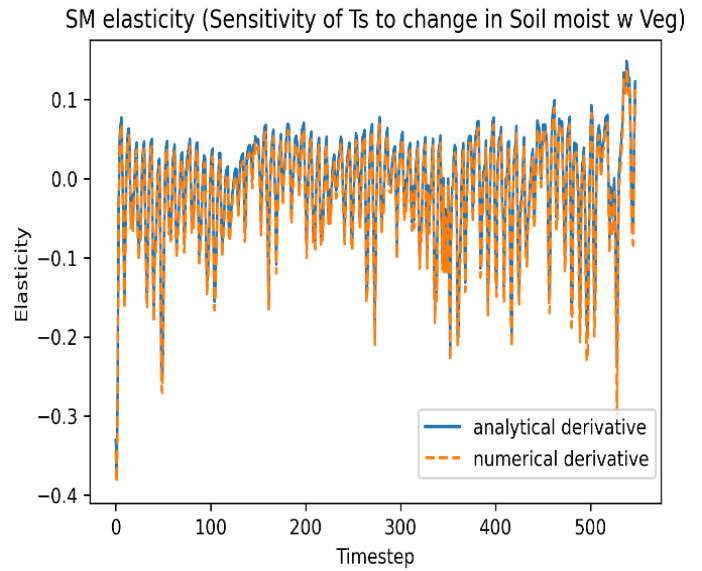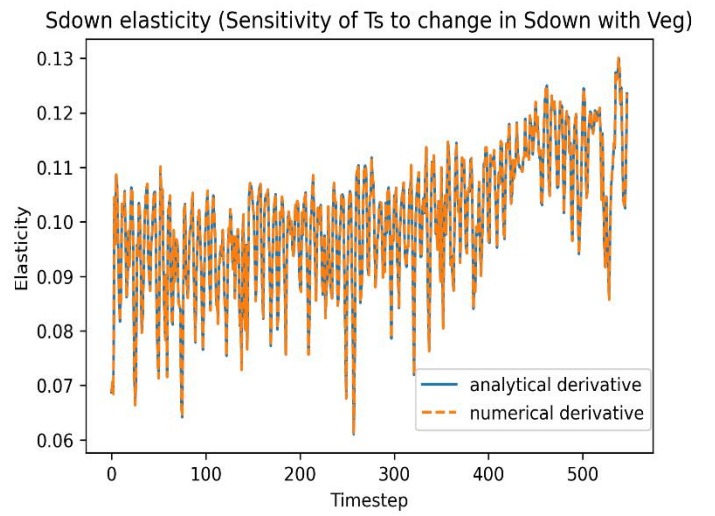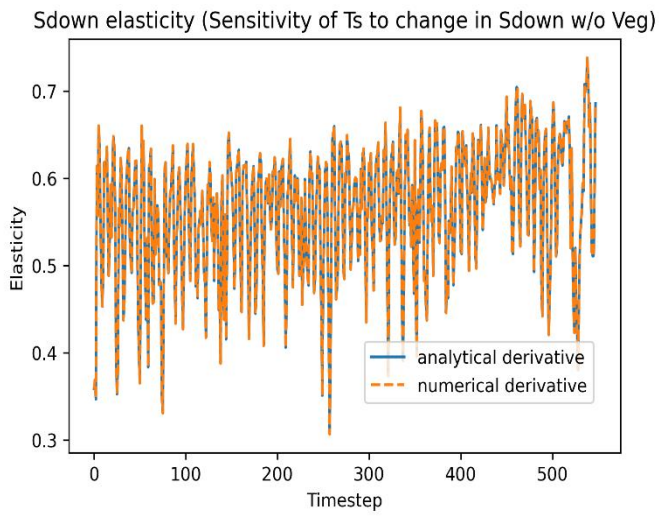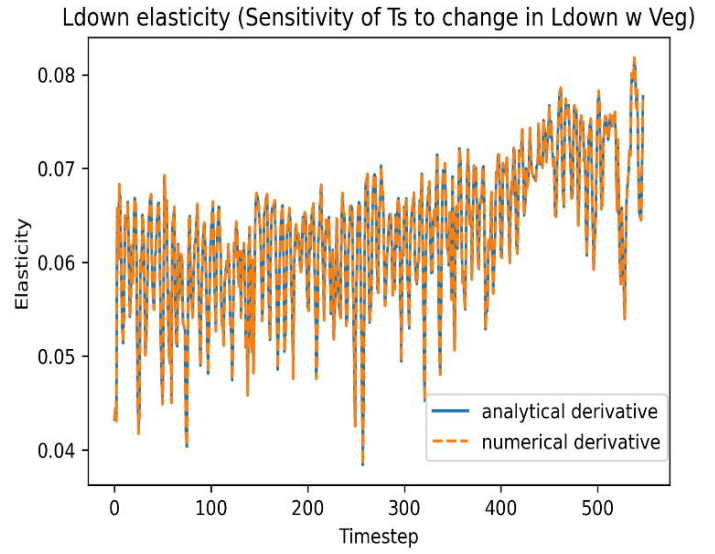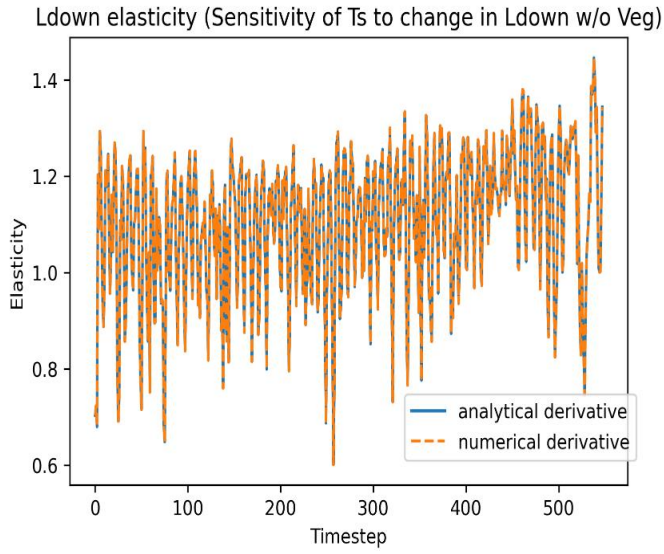
Fig F1. Comparison of analytical (solid blue) and numerical partial derivatives (dashed orange) showing exact match.

Appendix G: SSURGO soils data

Since SSURGO datasets on soils for Missoula over the urban areas is missing (Figure B1), land cover classification map was used to create spatially variable maps as input maps into Ech2o.
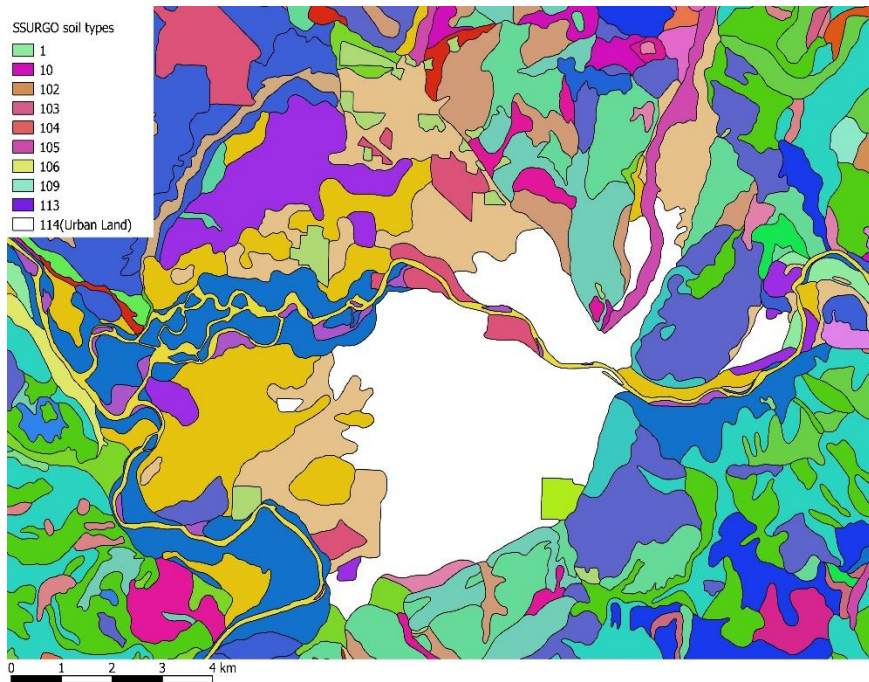
Figure G1. SSURGO missing soils data over Missoula (Web Soil Survey), classified simply as 'Urban land', soil map unit key 114. Missing soil data over urban areas occupy a total area of 6,315.3 acres and about 0.5% of Missoula county. SSURGO soils map overlain on land cover and land use classification map, processed in QGIS.

Appendix H: Anthropogenic heat

Anthropogenic heat profile for Missoula, MT calculations based on top-down methodology according to Sailor and Lu (2004) and Grossman-Clarke et al (2005). Data from University of Montana, Missoula campus and interpolated for select urban areas in study domain.

Anthropogenic heat (QAH) governing equation:

$$QAH = Q_b + Q_v + Q_m$$

Where QAH is total anthropogenic heat, Q_b is heat emissions from buildings, Q_v is heat emissions from vehicles and Q_m is metabolic heat of humans which for this study is considered negligible. All in units of W/m^2.
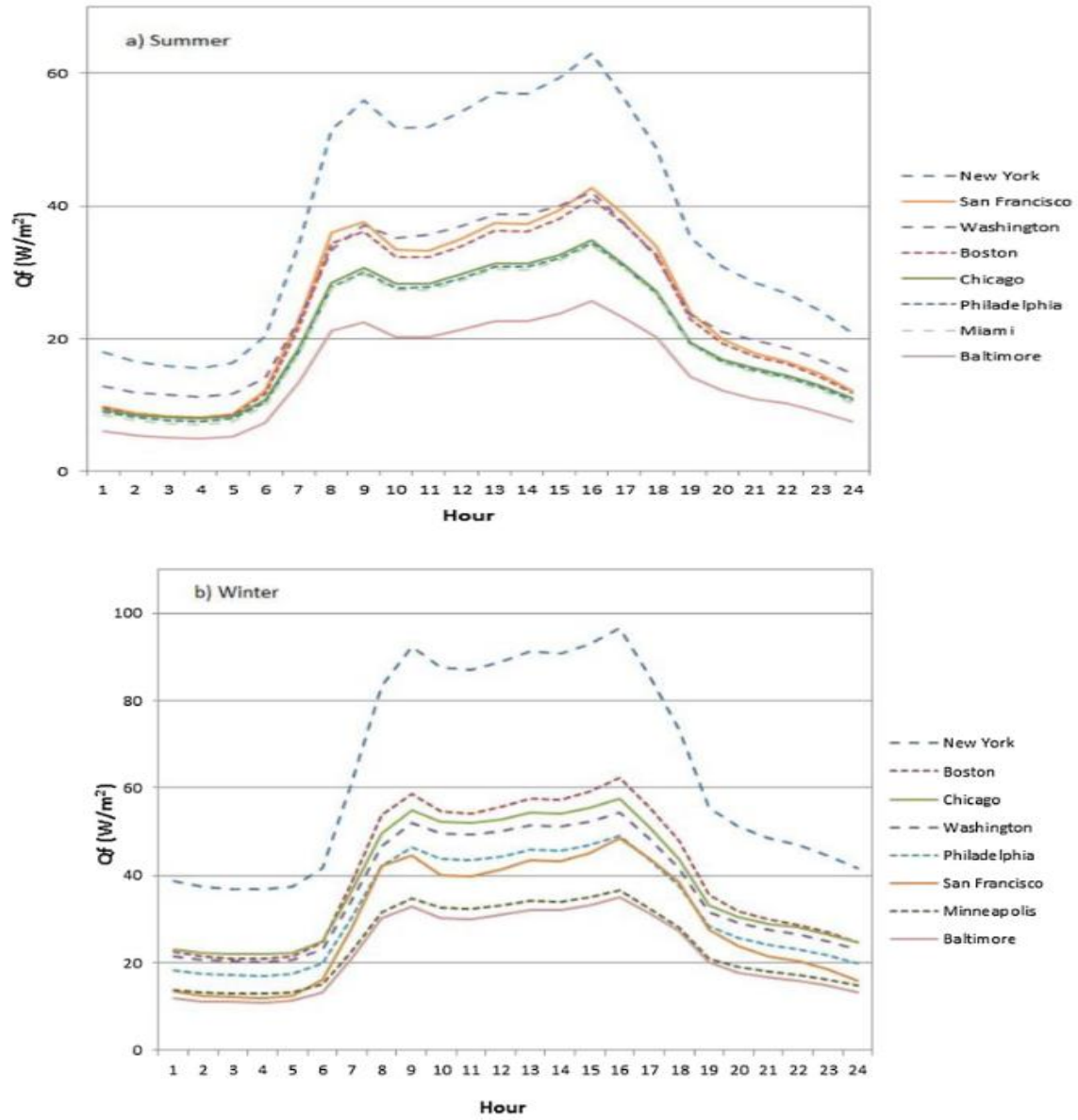
Fig. 3. January diurnal profiles for the 8 U.S. cities with the largest anthropogenic heating magnitude for (a) summer, and (b) winter.

73

QAH, 2012
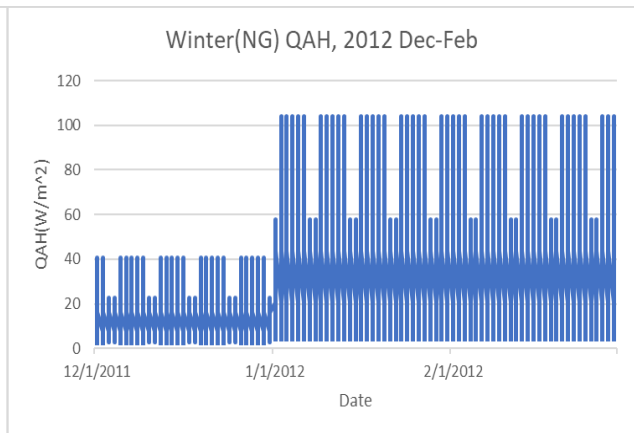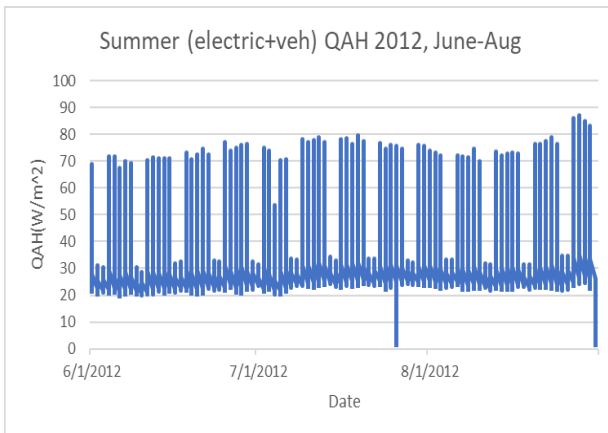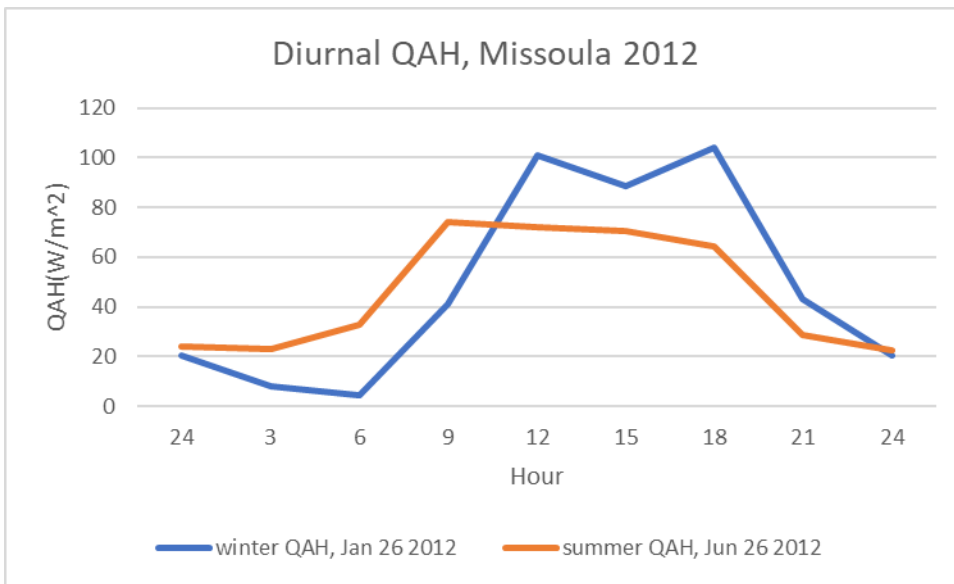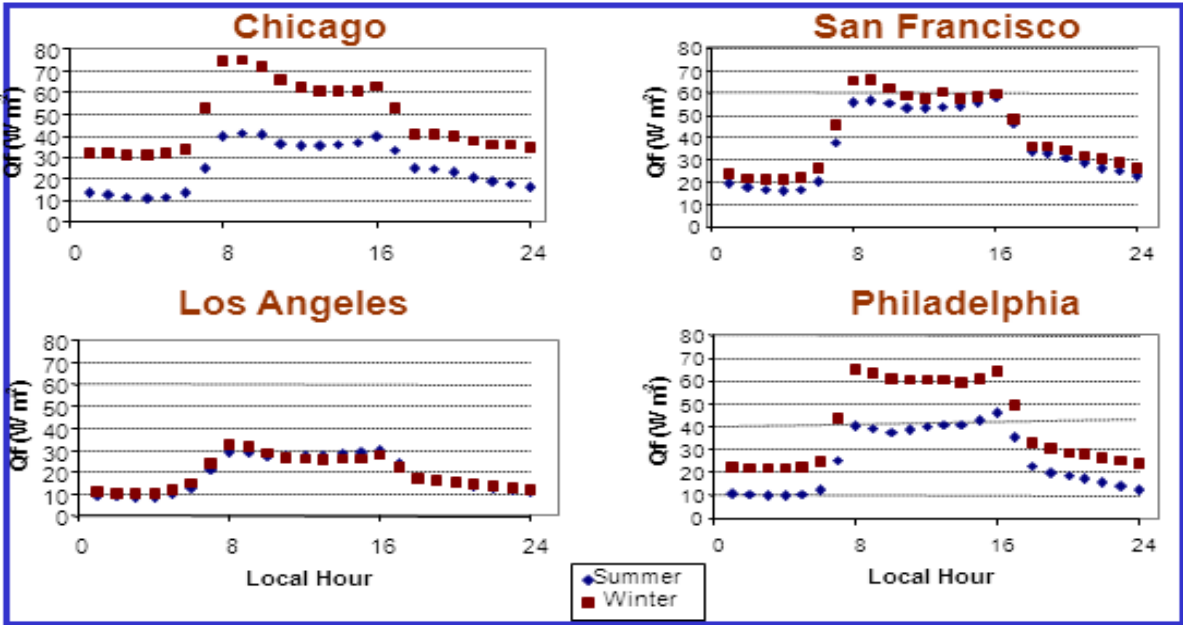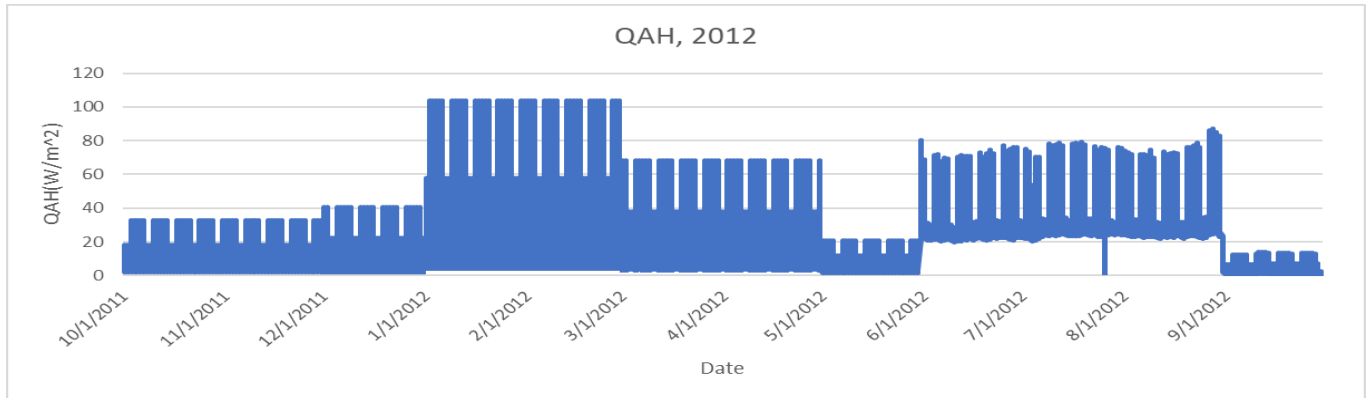
Building heat, Q_b $(\frac{W}{m^2})$:

$$Q_b = Q_e^* + Q_{ng}^\#$$

Q_e^*:

Where Q_e^* is total building heat from electricity usage where 80% is assumed to be AC use that contributes most to heat emissions during the summer (Jun-Aug). $Q_{ng}^\#$ is total building heat from natural gas and it is assumed that the typical thermal combustion efficiency is 80%.

$$Q_e^*(3hrly)(\frac{W}{m^2}) = \rho_{pop}(\frac{1}{m^2}) * E_c \,(3hrly)(W)/3600$$

Where ρ_{pop} is population density (m^-2):

$\rho_{pop}(\text{m}^\wedge - 2) = \text{population/area(m^2)}$

Population, Missoula MT = 57,887 in 1998 and 68,394 in 2012 (Montana Census and Economic Information Center and the American Community Survey (ACS), 2012).

Area, Missoula MT = 90,132,000 m^2 (City Limits Map as of July 5, 2019: https://www.ci.missoula.mt.us/468/Available-Maps)

ρ_{pop}(1998)= 6.4E-04 m^-2
ρ_{pop}(2012)= 7.5E-04 m^-2

Assuming 80% increase in population density during daytime working hours on weekdays in Missoula, MT, ρ_{pop}= 1.15E-03 m^-2, 1998 and 1.36E-03 m^-2, 2012.

E_c is per capita consumption of electricity (Watts): 15min data obtained from Brian Kerns, Engineer at University of Missoula. This data was summed to get 3-hourly time periods and extrapolated over entire City of Missoula, assuming similar consumption profiles.
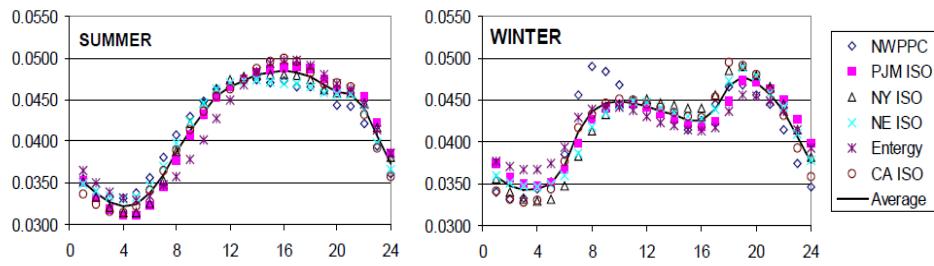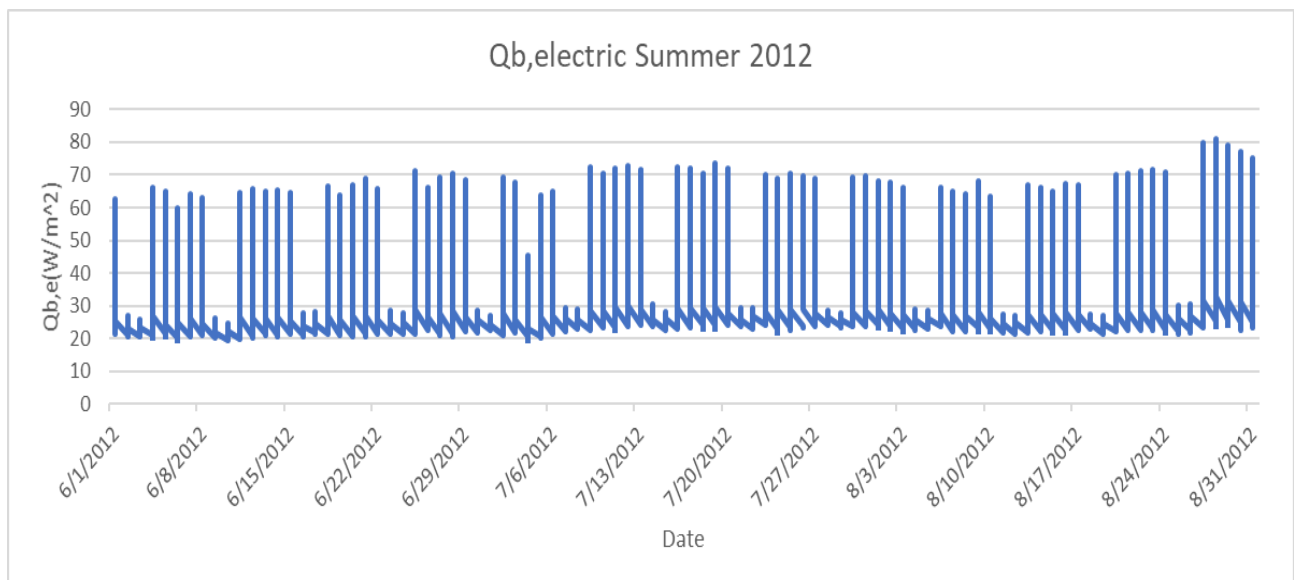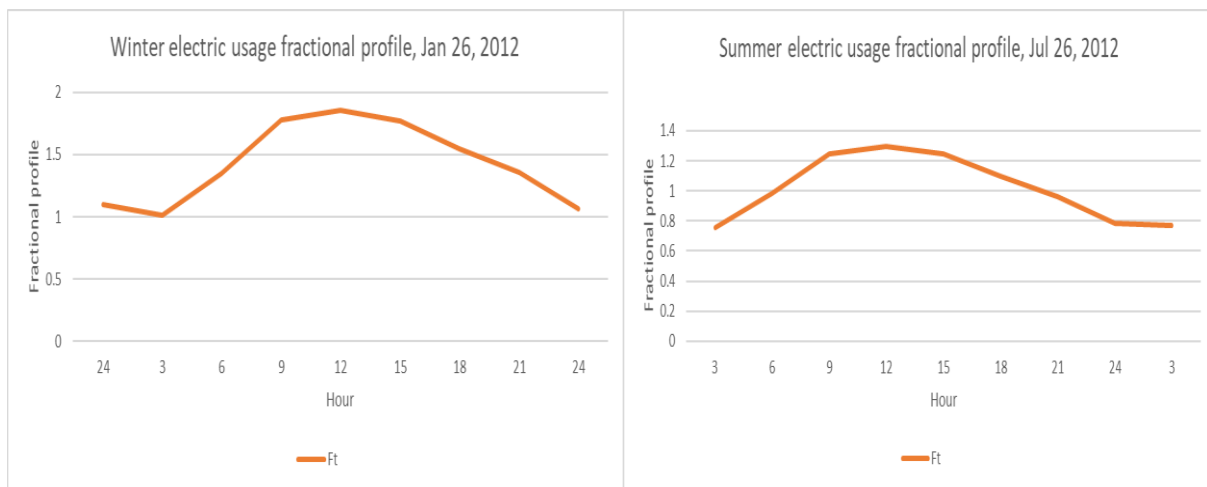
Fig. 3. Representative non-dimensional summer and winter electricity load profiles for various service areas across the US. The solid line represents the average of these profiles.

$$Q_{ng}^{\#}:$$

$$Q_{ng}^{\#}(3hrly)(\frac{W}{m^2}) = \rho_{pop}(\frac{1}{m^2}) * F(3hrly) * NG(W)$$

Where ρ_{pop} is population density in persons/m^2 and NG is natural gas in Watts.

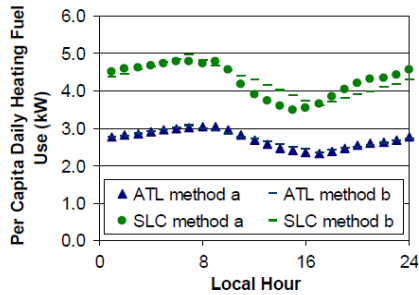F is 3-hourly fractional usage profile after Sailor & Lu, 2004 and is assumed same as vehicular fraction.
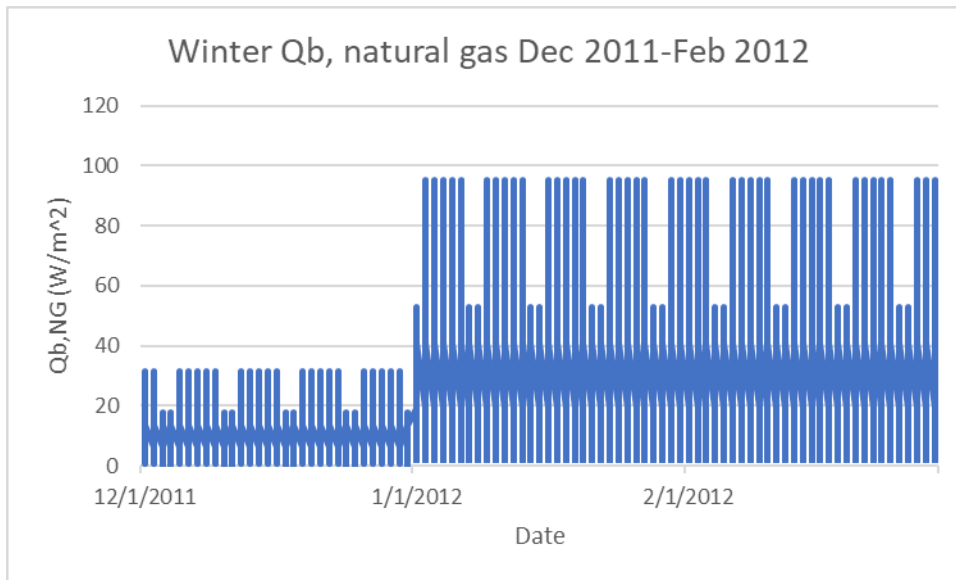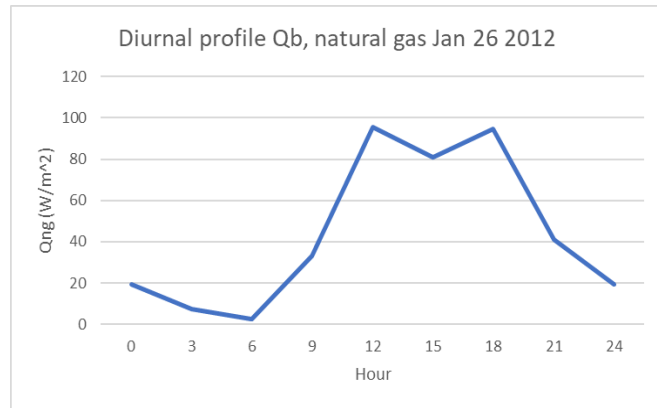
NG is 3-hrly natural gas usage in watts.

2745

Fig. 5. Comparison of winter HF profiles using two competing approaches for Atlanta (ATL) and Salt Lake City (SLC). Method a is the diurnal temperature formulation, and method b is the max-min temperature formulation.

Vehicle heat, $Q_v(\frac{W}{m^2})$:

$$Q_v(3hrly)(\frac{W}{m^2}) = \rho_{pop}(\frac{1}{m^2}) * F(3hrly) * E_v(\frac{J}{m}) * \frac{DVD_c(\frac{m}{day})}{3600 sec} * 3$$

Where E_v is energy release per vehicle per meter of travel (J/m):

$$E_v(\frac{J}{m}) = \frac{NHC(\frac{J}{kg}) * \rho_{fuel}(\frac{kg}{L})}{FE(\frac{m}{L})}$$

NHC is the net heat of combustion of gasoline (J/kg), ρ_{fuel} is the nominal fuel density (kg/L), and FE is the mean fuel economy (m/L). If one assumes a mean fuel economy of 8500 m/L (8.5 km/L), typical heat of combustion of 45x10^6 J/kg, and a nominal fuel density of 0.75 kg/L, E_v takes on a value of 3970 J/m of vehicle travel (Sailor & Lu, 2004).

DVDc is per capita daily vehicle distance travelled in Missoula (m/day/person):

$$DVD_c\left(\frac{meter/day}{person}\right) = \left(\frac{DVMT(mile/day)}{population}\right) * 1609.34$$

Where DVMT is daily vehicle miles driven in Missoula, obtained from Montana Department of Transportation, Cities Report, 2018. Total urban + rural daily distance driven is 1,078,989 miles for Missoula City. Given Missoula population of 57,887 for 1998 and 68,394 for 2012 (US Census Bureau, 2018), DVDc turns out to be 29997.4 m/day/person for 1998 and 25389.0 m/day/person for 2012.

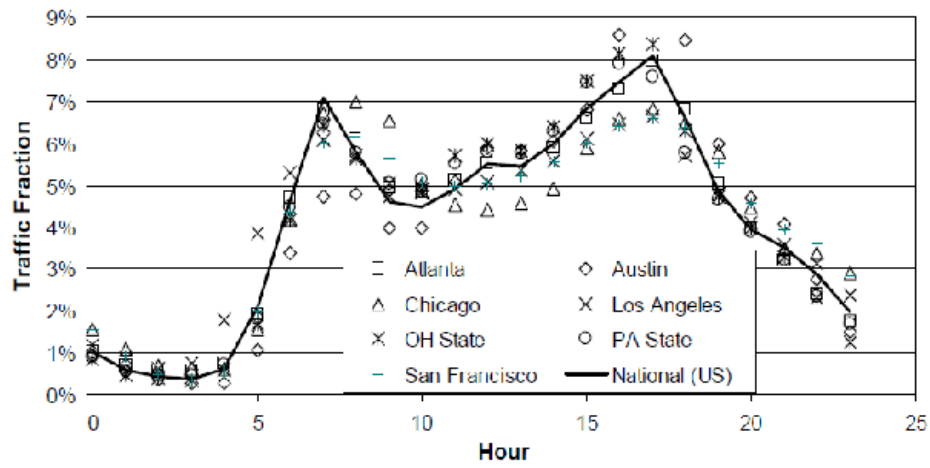F is 3-hourly fractional traffic profile after Sailor & Lu, 2004.

Fig. 2. Representative weekday hourly fractional traffic profiles (F_t) for various US cities and states. The bold line represents the national profile from (Hallenbeck et al., 1997).

Vehicle emissions Winter Dec 2011-Feb 2012

Vehicle emissions Summer Jun-Aug 2012